2024-05-01

Manipulation Of The Magnetic Properties Of Van Der Waals Materials Through External Stimuli

Luis Martinez
University of Texas at El Paso, lmmartinez12@miners.utep.edu

MANIPULATION OF THE MAGNETIC PROPERTIES OF VAN DER WAALS MATERIALS THROUGH EXTERNAL STIMULI

LUIS MIGUEL MARTINEZ MILIAN

Doctoral Program in Materials Science and Engineering

APPROVED:

Srinivasa R. Singamaneni, Ph.D., Chair

Prashant Padmanabhan, Ph.D.

Skye Fortier, Ph.D.

Davesh Mishra, Ph.D.

Hari Nair, Ph.D.

Stephen L. Crites, Jr., Ph.D.
Dean of the Graduate School

Per aspera ad astra

MANIPULATION OF THE MAGNETIC PROPERTIES OF VAN DER WAALS MATERIALS THROUGH IRRADIATION

by

LUIS MIGUEL MARTINEZ MILIAN, M.S.

DISSERTATION

Presented to the Faculty of the Graduate School of

The University of Texas at El Paso

in Partial Fulfillment

of the Requirements

for the Degree of

DOCTOR OF PHILOSOPHY

Department of Metallurgical, Materials, and Biomedical Engineering

THE UNIVERSITY OF TEXAS AT EL PASO

May 2024

Acknowledgements

To begin, I would like to thank all the collaborators that provided their help in one way or another throughout the various published works that make up this dissertation. First, I would like to thank the people who provided my group with the samples necessary before we even began the experiments laid out throughout this dissertation from Oak Ridge National Lab (Y. Liu and C. Petrovic) and Brookhaven National Lab (M. A. McGuire.) Second, I would like to thank the collaborators who performed complimentary characterization techniques from the National Institute of Standards (A. R. Hight-Walker and T. T. Mai) and Technology and Texas A&M University (L. Shao). Lastly, I would like to thank the collaborators who provided the theoretical backing to the experimental evidence from the Ecole Polytechnique Federale de Lausanne (J. Niklas, O. G. Poluektov, R. Yadav, M. Pizzochero, and O. V. Yazyv) and the University of Edinburgh (S. Haldar, T. Griepe, U. Atxitia, and E. J. G. Santos).

Next, I would like to thank my past lab mates who have now graduated and began their own Ph.D. journeys. Those are Hector Iturriaga (now at Stanford), Ruby Olmos (now at Rice), Chris Saiz (now at WhiteSands), Adrian Cosio (now at Sandia), and Jose Delgado (now at UC Boulder). Thank you for helping me with my experiments throughout your time here and allowing me to learn how to better guide students in their journey in conducting research.

I would also like to thank my committee members Hari Nair Ph.D., Skye Fortier Ph.D., and Davesh Misra Ph.D. for accepting to be a part of this huge effort, providing your feedback, and guidance when needed. Most importantly, I would like to thank my mentor Srinivasa Rao Singamaneni Ph.D. who has provided an enormous amount of guidance throughout my career from the moment we began building the lab back when I was a master's student in the Physics department and allowed me to grow as a scientist in more ways than one.

During my time as a young Ph.D. student, I was lucky enough to be selected into the Bridge to the Doctorate Louis Stokes Alliance for Minority Participation (BD-LSAMP). Thanks to this fellowship, I was able to commence my journey through my Ph.D. and received immense support from the people involved in that program. To add to that, I was also fortunate enough to receive the Science Graduate Student Research (SCGR) fellowship under the tutelage of Rohit Prasankumar Ph.D. allowing me to learn a completely new-to-me technique in the form of ultrafast optical spectroscopy. Most importantly, I would like to give an immense thank you to Prashant Padmanabhan Ph.D. who took the time to teach me how to swim in the metaphorical pool that is ultrafast optical spectroscopy and has provided guidance throughout my time as a graduate student intern in Los Alamos National Lab.

Finally, I would like to thank my parents, siblings, and friends who have provided love, guidance, moral support, and an understanding for my pursuit of knowledge outside of my home. Without the life lessons I have learned throughout my life through you, I would not be at the stage I am in my career. Gracias, padre, por siempre apoyar me y enseñar me que mis alas me pueden llevar a lo más alto que mis sueños quieran llegar.

Abstract

A new revolutionary application dependent on the electron spin to carry information with greater efficiency in data storage, transfer, and processing, will rely heavily on 2D magnets and the ability to effectively control their electron spins and engineer their properties. Previously, magnetic thin films were heavily studied to achieve this goal, however, these materials came with pitfalls and lacked naturally occurring 2D magnetism. The recent discovery of intrinsic magnetism in few-layered van der Waals (vdW) magnets has inspired researchers to extensively study them because of the feasibility to exfoliate them down to a monolayer. Due to this dimensionality factor, vdW magnets are susceptible to external stimuli opening a new avenue of exploration in the field of 2D magnets. However, the magnetic ordering temperature of these 2D vdW magnets remain quite low ($< 80\ K$) for real-world applications. Many research groups began engineering the magnetic properties of these 2D vdW magnets in their few-layered forms to enhance their ordering temperature without understanding how external stimuli affects a many-layered structure first. In this dissertation, two forms of external stimuli are implemented on various bulk vdW magnets. Optical excitation is shown to enhance the magnetization of a quasi-2D vdW magnet CrX_3 (X = Cl, I) by targeting its exchange interactions and is corroborated through Electron Spin Resonance spectroscopy. A sub-picosecond optical excitation of another quasi-2D vdW magnet $Mn_3Si_2Te_6$ (MST) reveals a coherent oscillatory mode that couples directly to the magnetic ordering. Lastly, proton irradiation takes advantage of the spin-lattice coupling in MST and reveals an enhancement in the magnetization at a particular proton fluence through the modification of the exchange interaction. The results presented in this dissertation demonstrate the feasibility to use external stimuli upon quasi-2D vdW magnets and use their exchange interactions as a tunable knob to control their magnetic properties.

Table of Contents

List of Tables

List of Figures

Chapter I – Introduction and Motivation

Today's technological progression has taken place due to a rigorous understanding of the fundamental properties of advanced materials and their development into a multitude of device applications pushing the boundaries of technology. This is a continuous cycle that requires researchers within the field of Material Science and Engineering to continue developing materials to improve their characteristics to match current societal needs such as renewable/sustainable energy, batteries with higher energy storage densities, and enhanced data storage density to name a few [1–3]. Currently, a strong push to develop materials for a new application in the form of spintronics is taking place, where the electron spin is the degree of freedom [4,5] that gives rise to macroscopic magnetism. This upcoming revolutionary application relies on the electron spin as the driver of information allowing greater efficiency in data storage, transfer, and processing [2,4–8] along with a reduced thermal load on devices [2]. However, to achieve effective control over the electron spin, the dimensionality of magnets must be reduced.

In this vein, researchers then began working on creating magnetic thin films through different synthesis techniques such as magnetic sputtering and pulse laser deposition [4,9]. The idea was to minimize three-dimensional (3D) magnetic material structures to the atomic scale. Unfortunately, these magnetic thin films lacked naturally occurring two-dimensional (2D) magnetism and suffered from dangling bonds, substrate effects, and lattice mismatching [4,10]. Luckily, the discovery of monolayer graphene catalyzed research into the van der Waals (vdW) material family, revealing interesting electrical and optical properties [11–13]. Some unique aspects of these vdW materials lie in their layered nature, with the vdW force holding the layers together, and a lack of dangling bonds along their interfaces preventing substrate effects [4]. Despite these important features, vdW materials lacked any sort of intrinsic magnetic ordering.

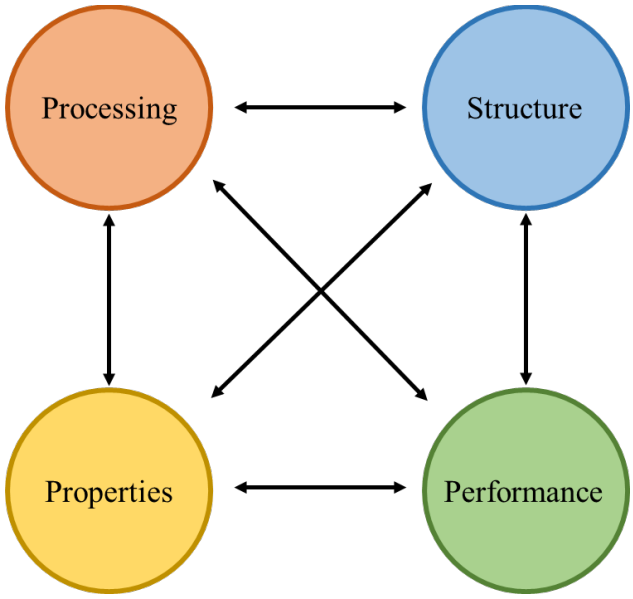

Figure 1: The materials paradigm demonstrating the interconnectedness between the preparation/synthesis (processing), structure, properties and performance of materials.

Auspiciously, material scientists and engineers followed the materials paradigm (see **Figure 1**) to induce magnetic ordering in these nonmagnetic vdW materials through various forms of external stimuli [14,15]. Nonetheless, intrinsic magnetism in these vdW materials was yet to be discovered.

During the conception of this dissertation, the field of vdW magnets made a grand entrance after the discovery of long-range magnetic ordering in monolayer [16] and bilayer [17] structures of CrI_3 and $Cr_2Ge_2Te_6$, respectively. This inspired other research groups to quickly begin extensive experimentation on these and other vdW magnets [18–22]. Due to their low cleavage energy [6], vdW magnets are easily exfoliable, allowing researchers to readily access 2D magnetic monolayers by simply using adhesive tape and depositing the exfoliated layers upon a substrate of choice. Furthermore, the low dimensionality of 2D vdW magnets makes their properties susceptible to external factors, opening a new avenue of exploration. The idea behind applying external stimuli to 2D vdW magnets was to enhance their low transition temperatures (typically below liquid nitrogen temperatures ~ 77 K) through the engineering of their exchange interactions and magnetic anisotropy [23].

This intense motivation led many research groups to study the effects of external stimuli on mono/few-layered vdW structures [24–28] without first addressing how introducing these external factors affects a many-layered crystal. Because of their intrinsic magnetic ordering, 2D vdW magnets retain many of their magnetic properties in their bulk form. Hence, it is incredibly useful to study the effects of external stimuli on bulk vdW magnets to gain a deeper understanding of the mechanisms behind the alteration of their magnetic properties in mono- and bilayer forms. Taking this approach, one can provide an empirical road map for the control of the magnetic properties in true 2D vdW magnets. This leads to the *principal goal* of this dissertation, which is to understand the intricate relationship between structure and magnetism in bulk vdW magnets through external stimuli.

Altering the magnetic properties of 2D vdW magnets through external stimuli has been highly successful [23], demonstrating the enhancement of the magnetic properties on multiple materials by various methods including; electrostatic gating, isostatic pressure, ion intercalation, and chemical doping [8,26,29,30]. However, other forms of stimuli can be applied to bulk vdW magnets to explore the perturbation-induced changes on the magnetic properties of these material systems. Within this dissertation, we will explore two types of external stimuli in the form of optical excitation and proton irradiation, demonstrating how these methods successfully control the magnetic properties of bulk vdW magnets through the modification of their exchange interactions.

To investigate the magnetic properties of 2D vdW magnets, optical spectroscopy becomes an important characterization tool using experimental techniques such as the magneto-optical Kerr effect (MOKE) [16,17], magneto-circular dichroism (MCD) [22], and magneto-photoluminescence [31]. These techniques can directly characterize the magnetic properties of

nanoscale magnetic systems, revealing the strong light-matter interactions that exist within the bulk vdW magnets. While most prior reports employed optical tools to probe the magnetic properties of 2D magnets, photoexcitation is also an ideal control knob, enabling remote and rapid control of the magnetic properties of layered vdW magnets. To advance the knowledge of light as a method of control, photoexcitation studies are required on well-known bulk vdW magnets with strong magneto-optical effects such as the CrX_3 (X = Cl, I) [31–33]. Of particular interest is applying optical excitation at various time scales from static (no temporal component) down to ultrafast excitations (femtoseconds (fs)). Static optical excitations can reveal time independent macroscopic changes to the magnetic properties while ultrafast excitations (< 100 fs) can reveal photo-induced changes upon the exchange interactions in magnetic systems [3].

On the other hand, the irradiation with high-energy, charged particles is another form of perturbation, enabling the alteration of the physical properties of materials. Specifically, proton irradiation is known to negatively impact the electrical properties of devices in spacecraft undergoing tasks near Earth's orbit [34–36]. Surprisingly, it can also have a positive impact on materials. Some reports have shown that this method is an effective tool to induce ferromagnetic ordering in some materials that are normally nonmagnetic [37–39]. For example, Mathew et al irradiated MoS_2 with protons introducing diamagnetic to ferrimagnetic order attributed to vacancies and edges states [39]. While another research group used proton irradiation to induce ferromagnetic ordering in pyrolytic graphite through the implantation of hydrogen [37]. However, proton irradiation has remained largely unexplored in intrinsically magnetic vdW materials. This opens the possibility to use this as another tool to modify the magnetic properties of bulk vdW magnets and provide evidence of the general behavior of magnetic vdW materials after irradiation.

Section 1.1 - Dissertation Overview

The rest of this dissertation is organized as follows: Chapter II provides an in-depth explanation of the experimental tools used to accomplish the established goals within this dissertation such as magnetometry, electron paramagnetic resonance (EPR) spectroscopy, and ultrafast pump probe spectroscopy. Chapter III explores the static photo-induced magnetic changes driven by targeting specific optical transitions within bulk CrI_3. Chapter IV takes a deeper look into the photo-induced magnetic changes in bulk CrX_3 (X = Cl, I) vdW magnets through EPR spectroscopy. Chapter V explores $Mn_3Si_2Te_6$ by characterizing its optical, vibrational, and spin dynamics through ultrafast optical excitation. In Chapter VI, the alterations in the magnetic properties of $Mn_3Si_2Te_6$ are thoroughly explored following exposure to proton irradiation with varying fluence. Lastly, Chapter VII summarizes the work presented in this dissertation and provides potential paths for further exploration.

Chapter II - Experimental Methods

Section 2.1 - Magnetometry

One of the most vital tools used to characterize bulk magnetic materials is static magnetometry. This technique provides a plethora of information regarding the materials' magnetic nature including its transition temperature (Curie temperature (T_C) for ferromagnets and Néel temperature (T_N) for antiferromagnetic systems), coercive field, magnetic field-dependent magnetization, magnetization saturation, remnant magnetization, and their magnetic susceptibility [40]. Further characterization of a material's magnetic properties can be extracted from this information, such as its Curie-Weiss behavior, the presence of long-range correlations, the effective magnetic moment, the critical behavior of a magnetic system, and even an estimate of its nearest-neighbor exchange interactions [41]. Typically, these parameters are obtained by examining the magnetic susceptibility (χ) of a material which is defined as:

$$M = \chi H \qquad 2.1.1$$

relating a material's magnetization (M) with an applied field (H). A temperature-dependent χ [$\chi(T)$] measurement is usually measured with either a zero-field-cooled (ZFC) or field-cooled (FC) protocol. A ZFC $\chi(T)$ measurement involves first cooling the in the absence of a magnetic field, followed by a measurement under an applied field. In contrast, a FC $\chi(T)$ requires the application of a magnetic field during the cool down process through the transition temperature and during the measurement. These two protocols are used to define the initial magnetic state of a material, providing information on the magnetic ordering of the system. Generally, magnetic systems possess an ordering temperature where they exhibit ferromagnetic (FM) or antiferromagnetic (AFM) ordering below this temperature and paramagnetic (PM) behavior above

this temperature. Within the PM phase, as stated previously, further information on the magnetic material can be extracted by fitting this temperature region with the Curie-Weiss law,

$$\chi(T) = \frac{C}{T-\Theta_{CW}}, \quad 2.1.2$$

where C (emu K mol^{-1}) is the Curie constant and Θ_{CW} (K) is the Curie-Weiss temperature [41], providing information on how the magnetic moments align under an applied magnetic field.

Most of this characteristic information can be extracted using a physical properties measurement system (PPMS). For this work, we make use of the VersaLab (VL) from Quantum Design. This system has a magnetic field range of $\pm$ 3 T and a temperature range of $50 - 400$ K. Other measurement options (e.g., heat capacity, AC susceptibility, and resistivity) can be used to further characterize the magnetic, electronic, and thermal properties of materials, however, the main measurement option used in this dissertation focuses on the vibrating sample magnetometer (VSM). As shown in **Fig. 2.1**, the VSM is comprised of four parts; (1) the electromagnet, (2) the linear transport motor, (3) pickup coils, and (4) the electronics to pick up the voltage induced by the sample on the pickup coils (V_{coil}). In this configuration, the pickup coils are a 1st order gradiometer which picks up the changes induced by the sample onto the coils that then produces the V_{coil}. This V_{coil} is determined by Faraday's Law of Induction,

$$V_{coil} = -\frac{d\Phi}{dt} = -\left(\frac{\partial\Phi}{\partial z}\right)\left(\frac{\partial z}{\partial t}\right) = CmA\omega\sin(\omega t), \quad 2.1.3$$

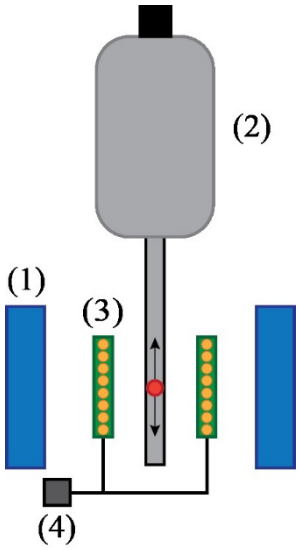

Figure 2.1: The schematic diagram of Quantum Design Versalab VSM magnetometer located in our laboratory. The schematic depicts the main components of the VSM system including (1) the electromagnet, (2) the linear transport motor, (3) the pickup coils, and (4) the electronics used to pick up the signal from the sample.

where C is the coupling constant, m is the sample moment (emu), A is the amplitude of vibration, and ω is the frequency of vibration. The linear transport motor provides the amplitude and frequency of vibration (which are optimal at $A = 2$ mm and $\omega = 40$ Hz). The generated signal is then sent to a pre-amplifier to amplify the signal. The amplified signal is then sent into a lock-in amplifier that uses phase sensitive detection (PSD) to measure the signal at the operating frequency. With these parameters and by using the 6 mm bore diameter pickup coils, the sensitivity of the instrument is about 6×10^{-7} emu.

In Chapter III, static magnetic measurements were conducted with an added option which includes coupling an external light source to the VSM to measure the photo-induced magnetic

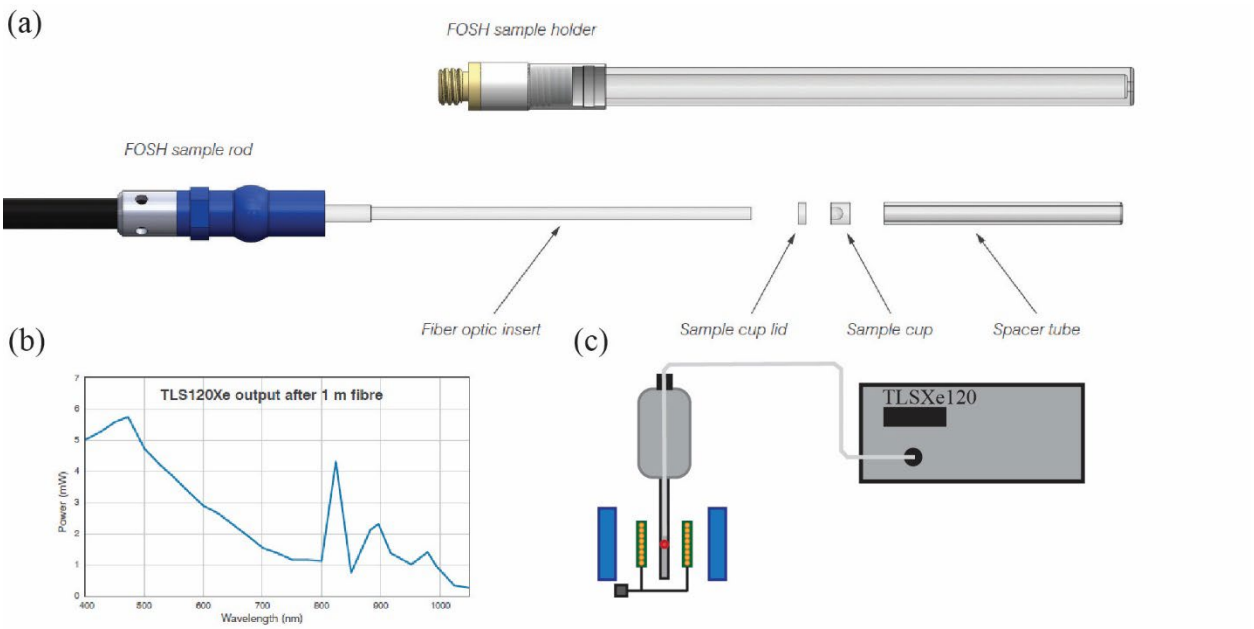

Figure 2.2: (a) Schematic of the fiber optic sample holder (FOSH)adapted from Ref [42] showing each component used to assemble the FOSH. (b) The optical spectra of the TLS120Xe adapted from Ref. [43]. (c) An example of how the TLS120Xe is connected to the FOSH and the VSM.

response of a magnetic material. This is done by using a different sample mount, sample rod, and a fiber optical cable that connects to the sample rod and the light source (shown in **Fig. 2.2**). All of these components come as a separate measurement option provided by Quantum Design. The sample mount in this new configuration is referred as the fiber optic sample holder (FOSH) [42]. It is comprised of quartz parts and has a sample cup inside to hold the sample in the center of the FOSH. This part then couples to the sample rod which contains a fiber optic cable that goes inside the FOSH so that the light impinges on the sample directly. These two components then go inside the VSM, and the fiber optical cable is then connected to the top of the sample rod (see **Fig. 2.2 (c)** for example). The FOSH reduces the moment sensitivity to $< 10^{-4}$ emu. Lastly, the fiber optic cable connects directly to a computer-controlled light source (Bentham TLS120Xe). The light source has a xenon bulb that is able to generate a broadband spectrum from $280 - 1100$ nm (see spectrum in **Fig. 2.2 (b)**) which can be filtered to a desired wavelength (with 40 nm FWHM) using an integrated filter wheel [43].

Section 2.2 - Electron Paramagnetic Resonance spectroscopy

While static magnetometry allows the macroscopic magnetic characterization of materials, it is not sensitive enough to detect minute changes surrounding the magnetic spin system. One of the most sensitive tools to detect local magnetic moments is electron paramagnetic resonance (EPR) spectroscopy [44,45]. EPR is a technique used to detect the splitting of electronic energy states through the application of electromagnetic radiation at a resonant magnetic field, also known as the Zeeman splitting. Additionally, this technique has the capability to become sensitive enough to detect down to 10^{13} spins, depending on the experimental parameters [44]. EPR can only detect centers with unpaired electron spins leaving this technique blind to systems with many paired spins. The materials of interest in this dissertation have transition metal magnetic centers containing unpaired electron spins within their $3d$ orbitals, making EPR a useful technique in our investigations.

The electromagnetic radiation in this technique comes from microwave radiation that is taken through a waveguide towards the cavity, where the frequency of operation can vary between $1 - 100$ GHz, however, the most common operational frequency of an EPR spectrometer is $\sim$9.5 GHz (X-Band frequency) which is the operational frequency used throughout this dissertation. This microwave radiation is steered through the waveguide towards the cavity. At the

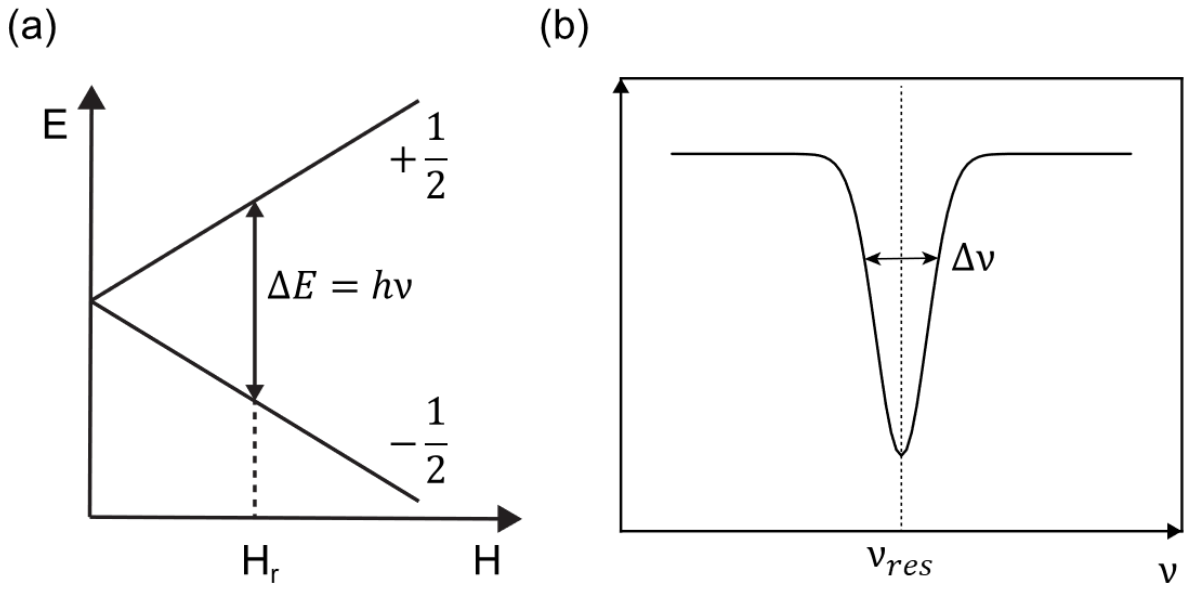

Figure 2.3: (a) shows Zeeman splitting occurring in an example system at a resonant field (H_r). Within an EPR cavity, a resonant frequency (υ_{res}) must be reached to maximize the sensitivity to enhance the resonant absorption of a paramagnetic material (b).

resonant frequency of the cavity, the energy density inside the resonator becomes large enough to allow greater sensitivity, enhancing the resonant absorption from a material. This sensitivity is determined by,

$$Q = \frac{\upsilon}{\Delta \upsilon}, \qquad 2.2.1$$

where Q is the quality factor, υ is the energy stored, and $\Delta\upsilon$ is the energy dissipated per cycle (shown graphically in **Fig. 2.3 (b)**). The resultant EPR signal from the material is then rectified and shown as the first derivative of the absorption. Lastly, two conditions have to be met for the resonance to take place: (i) the energy ($h\upsilon$) of the radiation must match the energy separation between particular electronic energy levels in the material, and (ii) the oscillating magnetic field component must be able to interact with an oscillating magnetic dipole moment (see **Fig. 2.3 (a)**) [45] in the material.

In solid state systems, EPR spectroscopy is also used as a tool to identify defects, paramagnetic species, and/or conduction electrons in semiconducting materials. One of the most

important parameters that can be extracted from EPR spectroscopy is the Zeeman splitting factor, also known as the g-value described as,

$$g = \frac{hv}{\beta_e H_o}, \qquad 2.2.2$$

where h is Planck's constant, v is the operating frequency, β_e is the Bohr magneton constant, and H_o is the signal's center field. The g-value in this spectroscopic technique is known to provide an almost fingerprint-like identification of a paramagnetic species. For a free electron, this value is $g_e = 2.00231$ and is one of the most accurately known physical constants. This g-value can vary between different paramagnetic species due to the surrounding atoms, spin-orbit coupling, and the local magnetic field [44,45] . Additional information can be extracted by simulating the line shape of the EPR signal. Different line shapes can be used to determine homogeneous and inhomogeneous broadening (Lorentzian and Gaussian line-shapes, respectively), and if asymmetry exists within the EPR line-shape (Dysonian line-shape). Throughout this dissertation, the EPR signals were found to be best simulated with a Dysonian line shape of the form,

$$P = \left(\frac{16I}{\pi}\right)\left[\frac{\alpha\left(\sqrt{2}H_{pp}\right)^2 - 4\alpha(H-H_o)^2 - 8\left(\sqrt{2}\,H_{pp}\right)(H-H_o)}{\left(4(H-H_o)^2 + \left(\sqrt{2}\,H_{pp}\right)^2\right)} + \frac{\alpha\left(\sqrt{2}H_{pp}\right)^2 + 4\alpha(H+H_o)^2 - 8\left(\sqrt{2}\,H_{pp}\right)(H+H_o)}{\left(4(H+H_o)^2 + \left(\sqrt{2}\,H_{pp}\right)^2\right)}\right], \qquad 2.2.3$$

where P is the absorbed power, I is the dimensionless intensity factor, α is the asymmetry parameter, H_o is the center field, and H_{pp} is the peak-to-peak linewidth of the EPR signal.

The EPR experiments performed in Chapter IV were measured through a collaboration with Argonne National Lab. For those experiments, a continuous-wave (CW) X-band (9.45 GHz) Bruker ELEXSYS II E500 EPR spectrometer was employed, equipped with a TE102 rectangular EPR resonator (Bruker ER 4102ST). For cryogenic temperatures, a helium gas-flow cryostat and

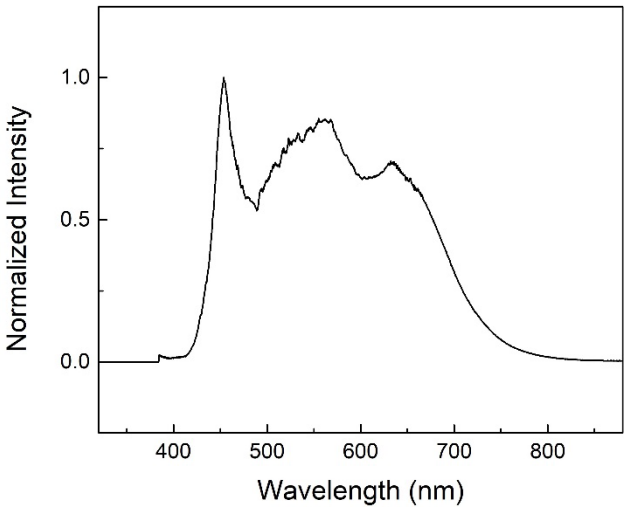

Figure 2.4: Optical spectrum of the Solis 3c white LED source used for the light-induced EPR experiments in Chapter IV. The data for this spectrum was taken from Thorlabs Inc.

a PID temperature controller (Oxford Instruments ITC503) were utilized. All the EPR experimental settings were kept constant throughout the experiments to ensure reproducibility. For the EPR measurements, the samples were inserted into a quartz tube under a nitrogen atmosphere. The sample platelets were mounted such that the magnetic field was applied perpendicular to the plane of the sample. The light source implemented in Chapter IV was a Solis-3c white (daylight) LED from Thorlabs and the optical spectrum for this light source is shown in **Figure 2.4**. The maximum power output from this light source is ~1 W. The time traces collected for the EPR spectra in Chap. IV had a 40 ms resolution time. The EPR measurements shown in Chapter VI were measured with a similar EPR spectrometer at the University of Texas at El Paso.

Section 2.3 - Ultrafast Pump-Probe Spectroscopy

The capability to drive materials out of equilibrium allows us to study transient properties on femtosecond timescales, and track dynamic phenomena, such as time-resolved photoinduced phase transitions [46,47], ultrafast de/remagnetization [48–51], and the interplay between the electronic, lattice, and spin subsystems [48,52]. This is achieved by driving a material with a high-

intensity optical pump pulse which perturbs the system out of equilibrium, using a weaker time-delayed probe pulse to measure the dynamic changes. This method of detection, also known as ultrafast pump-probe spectroscopy, can temporally resolve the electronic, magnetic, and optical properties of materials. In this section, I will briefly explain the details of a pump-probe experiment, how a laser system operates, and the type of laser implemented in Chapter V.

Pump-probe spectroscopic experiments can have a temporal resolution that far exceeds that of the electrical bandwidth limits of an electronic measurement system. It is possible to avoid the limits imposed by the electronics by implementing a stroboscopic sampling technique that reconstructs the signal by probing the induced changes upon the material system. To accomplish this, every datapoint is taken as an average of the pump-induced signal over many pulses at a given time delay. The temporal resolution is set by the pulse duration of the pump and probe, and the step size between the measured time delay points.

The laser system is essentially an optical oscillator consisting of an amplifying medium inside a suitable optical cavity. Currently, most commercially available and experimentally viable lasers are those with a titanium (Ti^{3+}) doped sapphire ($Ti:Al_2O_3$ also known as Ti:Sapph) crystal as the amplifying medium. This amplifying medium can generate optical pulses with < 50 fs temporal width and relatively large wavelength tunability ($740 - 1050$ nm). Ti:Sapph based lasers operate best at approximately 1.55 eV (800 nm) due to the maximum gain and high laser efficiency attained at that photon energy [52].

For the experiments performed in Chapter V, the laser of choice was a Ti:Sapph regenerative amplifier that is seeded by a Ti:Sapph oscillator. The oscillator (Coherent Mantis) generates an ~ 800 nm optical pulse train at ~ 80 MHz with a bandwidth of ~ 70 nm, allowing the pulses to have transform-limited temporal width of 20 fs. The resulting optical pulse gets sent into

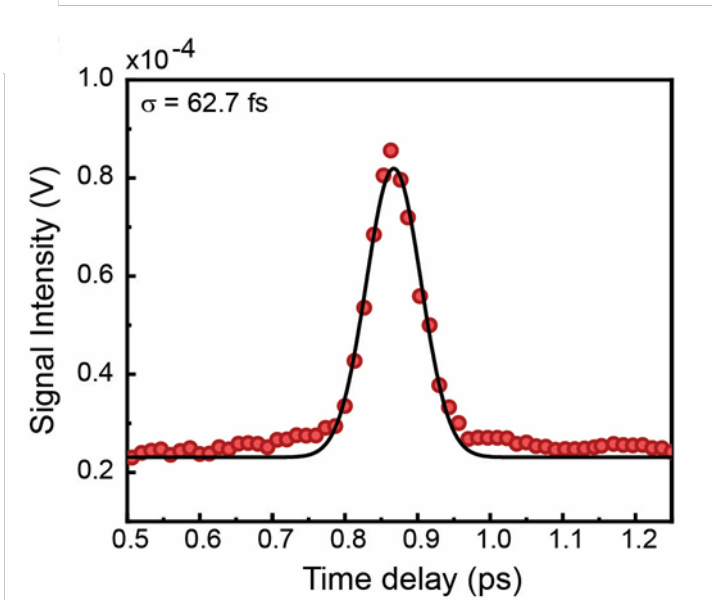

Figure 2.5: Pulse width characterization of the laser system used for the pump probe experiment in Chapter V, where the red circles represent experimental data, and the black line is a fit to the data using a Gaussian function to extract the pulse width (σ).

an optical stretcher system to reduce the laser intensity to avoid damaging the optical components within the next stage. This stretched pulse train then gets seeded into a regenerative amplifier system (Coherent RegA 9000) increasing the pulse energy to ~ 5 μJ when operated at a 100 kHz repetition rate. The amplified pulse then gets sent into an optical compressor that allows the user to compensate for group delay dispersion (GDD) to achieve the shortest pulse possible at the sample position. GDD is chromatic dispersion caused by the laser beam passing through dispersive components. This chromatic dispersion causes the different frequency components within the pulse to experience a different relative delay in their propagation, inherently stretching the pulse width of the laser beam. To compensate for this issue, a second harmonic generation (SHG) cross-correlation experiment can be performed, allowing for the quantification of the pulse width through the relative temporal displacement between the two pulses that are identically split from a source beam [53]. Each pulse can generate an SHG signal when focused onto a nonlinear optical crystal (e.g., β-barium borate, BBO). However, when the two pulses are focused onto the same

spot at a small crossing angle and overlapped in time, they generate an SHG signal together, with a vanishing in-plane wavevector component (i.e., the SHG pulse propagates normal to the crystal surface). By measuring the temporal width of this SHG signal (by stepping the delay of one input pulses relative to the other) and properly normalizing based on the expected pulse shape [53], one can obtain the pulse width of the input pulses. By adjusting the compression of the input beam while simultaneously measuring this pulse width, we can then compensate the GDD at the sample position, ensuring the shortest possible on-sample pulse. **Figure 2.5** shows the cross-correlation trace taken for the experiment in Chapter V with an adjusted pulse width of 62 fs.

The RegA outputs ~900 mW (average power) of temporally compressed 800 nm pulses at a 100 kHz repetition rate. This beam gets sent into the experimental setup shown in **Fig. 2.6**. The main beam is split into degenerate pump and probe arms using a 50/50 beam splitter. The double-bladed optical chopper allows for the separate modulation of the pump and probe arms. We typically used a pump chopper frequency was $f_{pump} = 700$ Hz and a probe chopper frequency was $f_{probe} = 500$ Hz. Subsequently, the pump beam passes through a computer-controlled

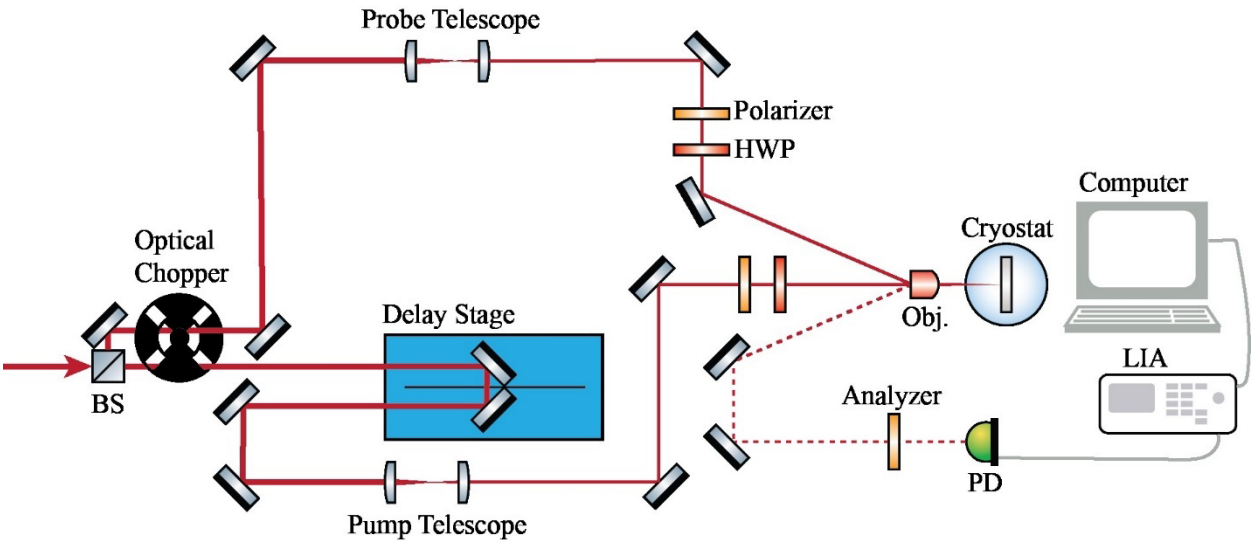

Figure 2.6: Experimental setup implemented for the experiments in Chapter V. BS is a beam splitter, HWP is a half-waveplate, Obj is an objective, PD is a photodiode, and LIA is a lock-in amplifier.

mechanical delay line (Newport ILS250PP) with a minimum repeatable step size of 1 μm and a backlash of ± 1 μm. Both beams then pass through separate telescopes to reduce the spot sizes. A combination of a polarizer and a half-waveplate (HWP) are used to control the polarization state and power of each beam separately. For further context, a polarizer is an optical component that only allows light of a particular polarization to transmit set by the direction of its transmission axis. A HWP can linearly change the polarization state of light (e.g., if the incoming beam is vertically polarized and the fast axis of the HWP is at 45^o, then the transmitted light through the HWP will be horizontally polarized). In the experiments performed in Chap. V, the pump and probe were cross-polarized to reduce noise (due to scattered light from the pump entering the detector). Before the sample, the pump beam was set to come in at normal incidence, with respect to the sample surface, while the probe beam was set to be slightly off normal incidence to collect the reflected probe beam with a pick-off mirror that sends the beam onto a photodiode. The photodiode is connected to a lock-in amplifier (LIA) that is referenced to the sum frequency ($f_{sum} = f_{pump} + f_{probe}$) of the pump and probe chopping frequency to phase-sensitively isolate the pump-induced changes in the reflected probe intensity. The LIA signal is connected to a computer through a GPIB connection which is controlled through a LabView program that allows the read-out of the LIA signal while also moving the delay stage to measure the pump-induced changes as a function of pump-probe delay. We typically used a time delay interval of 33 fs (9.9 μm).

In the pump-probe experiment utilized in Chapter V, the change in the sample reflectivity (ΔR) induced by the pump is determined by the reflection coefficient. Let us look at **Figure 2.7** which shows an incident electromagnetic wave with electric field (magnetic field) $\vec{E}^{(i)}$ ($\vec{B}^{(i)}$) that is

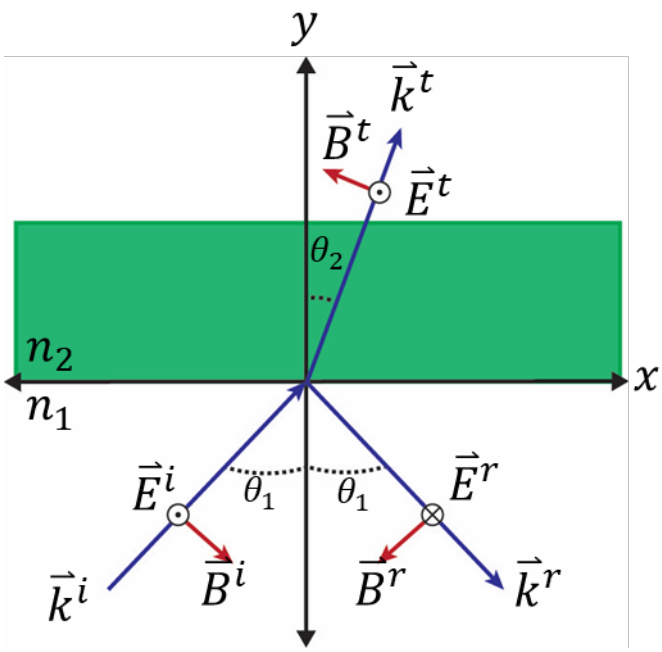

Figure 2.7: Schematic representation of an incident electromagnetic wave upon an isotropic system with the reflected (transmitted) electromagnetic wave. The green square represents a sample medium that reflects (transmits) the incident wave with an index of refraction n_2 and n_1 is the index of refraction in a vacuum.

polarized parallel to plane of incidence. This is referred as *p*-polarization and if the wave was polarized perpendicular to the plane of incidence that is referred to as *s*-polarization. The incident wave can be written as,

$$\vec{E}^{(i)}(\vec{r},t) = E_o^{(i)} e^{i(\vec{k}\cdot\vec{r}-\omega t)} \qquad 2.3.1$$

where $E_o^{(i)}$ is the electric field amplitude, $\vec{k}$ is the wavevector, $\vec{r}$ is the position vector, ω is the angular frequency, and t is the time [54] with similar expressions for the reflected and transmitted wave. At the boundary, we find that,

$$E_o^{(i)} + E_o^{(r)} = E_o^{(t)} \qquad 2.3.2$$

particularly for the *s*-polarization state. A similar expression can be gleaned from the tangential component of B as,

$$B_o^{(i)} cos\theta_{(1)} - B_o^{(r)} cos\theta_{(1)} = B_o^{(t)} cos\theta_{(2)} \qquad 2.3.3$$

and by implementing $E_o = \left(\frac{c}{u}\right) B_o$ (where c is the speed of light in vacuum, u is the speed of light in the medium, and the ratio between them is n the index of refraction [55]) we can reduce the above equation to

$$\frac{E_o^{(i)}}{n_1} cos\theta_{(1)} - \frac{E_o^{(r)}}{n_1} cos\theta_{(1)} = \frac{E_o^{(t)}}{n_2} cos\theta_{(2)} \quad 2.3.4$$

Furthermore, the *field* reflection coefficient is defined as $r = \frac{E_o^{(r)}}{E_o^{(i)}}$ and can be expanded by solving for $E_o^{(r)}$ in terms of $E_o^{(i)}$ [54] resulting in the following expression (for *s*-polarization),

$$r_s = \frac{n_1 cos\theta_1 - n_2 cos\theta_2}{n_1 cos\theta_1 + n_2 cos\theta_2} \quad 2.3.5$$

While for *p*-polarization,

$$r_p = \frac{n_1 cos\theta_2 - n_2 cos\theta_1}{n_1 cos\theta_2 + n_2 cos\theta_1} \quad 2.3.6$$

These two equations are known as the Fresnel equations, and if an incident wave comes in normally incident upon the sample surface ($\theta_1 \approx 0$) then

$$r_s = r_p = \frac{n_1 - n_2}{n_1 + n_2} \quad 2.3.7$$

Which relates the index of refraction of material system with the *field* reflection coefficient [52,54]. Now, what is measured during a pump-probe experiment is the *intensity* reflection coefficient which is $R = |r|^2$ [52]. So, when an optical pulse perturbs the system, it induces a change in the refractive index of the material ($n \rightarrow n + \Delta n$) which changes the material's reflectivity ($R \rightarrow R + \Delta R$). Finally, the optically induced changes upon the refractive index are proportional to the differential reflectivity by [52],

$$\frac{\Delta R}{R}(\hbar\omega_{probe}, t) = \frac{4\Delta n(\hbar\omega_{probe}, t)}{n^2(\hbar\omega_{probe}) - 1}, \quad 2.3.8$$

which is the information collected within Chapter V.

Chapter III - Magnetic properties of bulk vdW ferromagnet CrI_3 upon photoexcitation

As illustrated in the introductory Chapter, multiple routes have been explored demonstrating control over the magnetic properties of vdW magnets using external stimuli such as electric fields [24,56], electrostatic doping [57], and mixed halide chemistry [58,59]. Because of their layered nature, the ground state of these vdW magnets may display greater sensitivity to external stimuli such as photoexcitation. Thus, light excitation can become a unique route to modify these properties without creating contacts and damaging the sample. This, in turn, provides a versatile, contactless method for manipulating their properties. This method of control has been employed as early as the late 1960's, when researchers looked at the permeability of a chalcogenide spinel after illuminating the sample with a white-light source [60]. Other riveting experiments have been conducted by using intense pulses of light to study the femtosecond magnetization dynamics of various magnetic systems, such as the ultrafast demagnetization in Nickel [61], tuning the exchange parameters in $FeBO_3$ [62], and all-optical thermal switching in the ferrimagnetic Mn_2Ru_xGa [63].

Recently, greater emphasis has been placed on studying the effects on the magneto-optical properties of vdW magnets [64–69] due their strong light-matter interactions. In particular, the CrX_3 vdW magnets are a unique set of materials possessing various optically accessible electronic transitions [70,71] that can be excited to alter their magnetic properties. Interestingly, multiple theoretical studies have predicted a strong coupling between light and magnetism in these semiconducting vdW magnets stemming from a complete spin polarization between the conduction and valence bands [72–74]. Evidence of this has been shown by Zhang et al who targeted some of these optical transitions (1.96 [633 nm] and 2.33 eV [532 nm]) in tri-layer CrI_3

by applying circularly polarized photons to excite electron-hole pairs [75] inducing a spin-flip transition. However, how these optical transitions affect the magnetic nature of bulk CrI_3 still remains an open question. In this chapter, we seek to answer this question by employing static magnetometry along with an unpolarized continuous wave (CW) light source to target specific optical transitions in polycrystalline bulk CrI_3 to characterize light-driven changes in its ordering temperature, magnetization, and exchange interactions.

The optical properties of the CrI_3 vdW magnets have been investigated in the past [70,76–78]. The most prominent optical absorption peaks in CrI_3 are correlated to two ligand-to-metal charge transfer (LMCT 1 (1.93 eV) [642 nm] and LMCT 2 (2.7 eV) [459 nm]) and two *d-d* (*d-d* 1 (1.79 eV) [689 nm] and *d-d* 2 (1.5 eV) [827 nm]) transitions located above its bandgap. LMCTs are a type of electronic transition that occur after the absorption of light at specific wavelength promotes an electron from a ligand *p*-orbital to a higher-energy metal *d*-orbital (see **Figure 3.1 (a)**), reducing the metal ion [79]. The absorbed energy relates to the energy difference between the initial and

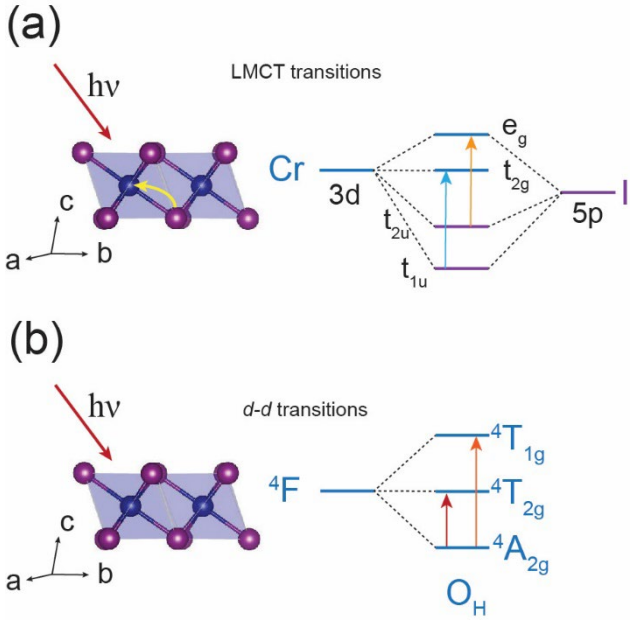

Figure 3.1: Partial crystal structure of CrI_3 showing the electronic transition between the ligand *5p* orbital (t_{2u} or t_{1u}) to either the t_{2g} or e_g orbitals after optical excitation of the LMCT transitions (a). Similarly, after optical excitation of the *d-d* transitions in CrI_3, an electronic transition occurs within the *3d* orbitals from the octahedrally split ground state ($^4A_2$) to the $^4T_2$ or $^4T_1$ states.

final electronic states involved in the LMCT transition. In the case of *d-d* transitions, an electronic transition occurs between the *d* orbitals of the transition metal centers. Specifically, an electron spin can be excited from the $^4A_2$ orbital ground state to an excited state ($^4T_2$ or $^4T_1$) (see **Fig. 3.1 (b)**). It is important to note that some *d-d* transitions can be forbidden due to the Laporte Selection rule which says that transitions between electronic states with the same parity are forbidden in complexes with inversion symmetry [80,81]. However, these transitions can become enabled if odd parity mixing states exist as in the case in CrI_3. Additionally, a trigonal field from the nearest-neighbor Cr atoms distort the octahedral field breaking the local inversion symmetry within each Cr site permitting these *d-d* transitions to become weakly allowed [71,82]. An example of this was demonstrated by Padmanabhan et al [82] who identified the spin-lattice coupling in CrI_3 by pumping with one of these *d-d* transitions (1.55 eV) demonstrating the helical sensitivity of this optical transition. In the following sections, we reveal the effects on the magnetic properties of CrI_3 after photo excitation of the LMCT and *d-d* transitions.

Section 3.1 – Photoexcitation with LMCT transitions

We begin by targeting the LMCT transitions on bulk polycrystalline CrI_3 and measuring the $M(H)$ curves above and below T_C as shown in **Figure 3.2 (a, b)**. From the $M(H)$ measured at 100 K (**Fig. 3.2 (a)**), exciting either at the LMCT transitions results in an enhancement in the magnetization while still demonstrating PM behavior. **Figure 3.2 (b)** shows the isothermal $M(H)$ curve measured within the FM phase (50 K) for pristine and the two LMCT optical excitations. For pristine CrI_3, the magnetization measured at 30 kOe is 1.70 μ_B/Cr, which is quite close to that of Ref. [83]. In the report by McGuire et al, the magnetization of CrI_3 single crystals is measured along its magnetic easy axis at 2 K and the authors characterized the saturation

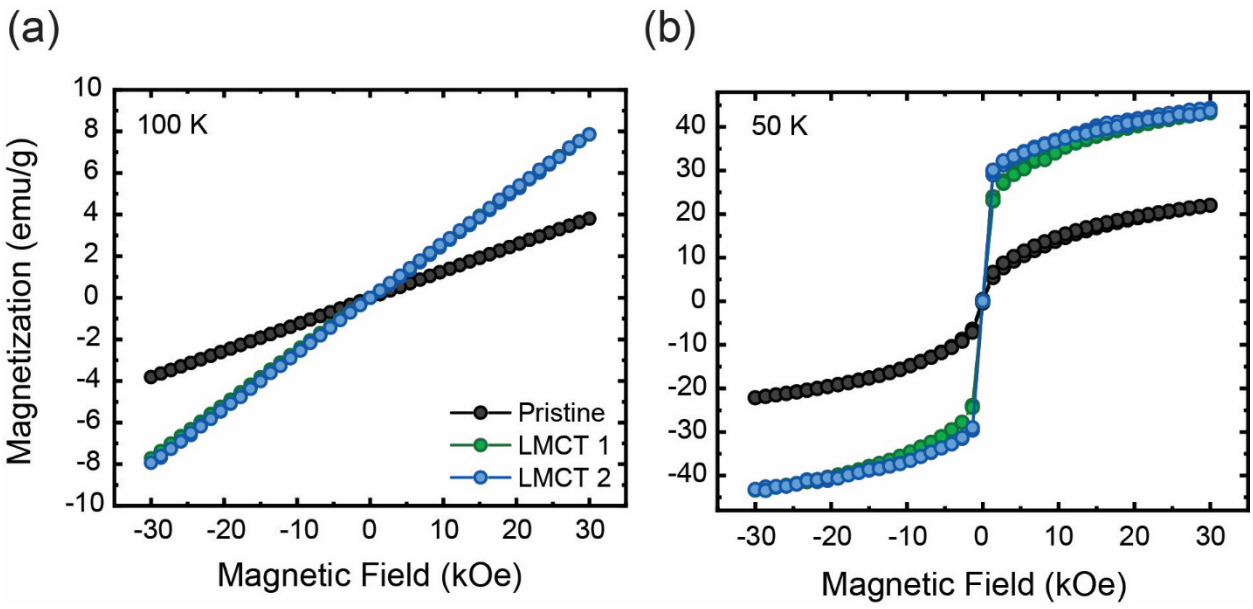

Figure 3.2: M(H) curves measured above (a) and below (b) the $T_C = 60\ K$ for pristine CrI_3 (black circles) and after optical excitation of the LMCT 1 (green circles) and LMCT 2 (blue circles) transitions.

magnetization to be 3 μ_B/Cr corresponding to trivalent Cr in an octahedral environment with $S = 3/2$ [83]. Remarkably, after optically exciting with both LMCT transitions in the experiments presented here, the magnetization reaches a value of 3.38 μ_B/Cr in CrI_3 at 50 K which is greater than the previously reported saturation magnetization at 2 K [83].

Next, we study the temperature dependence of the magnetic susceptibility ($\chi(T)$) in CrI_3 before and after photoexcitation of the LMCT transitions. **Figure 3.3 (a)** shows $\chi(T)$ taken through a ZFC protocol and measured with an applied magnetic field of $H_a = 1$ kOe, where pristine CrI_3 demonstrates its FM behavior below 60 K, as expected. Through this measurement, we noticed that after exciting at each of the LMCT transitions, a stronger effect was observed at the LMCT 2 transition, relative to LMCT 1. However, optical excitation at the resonances still enhanced the $\chi(T)$ of CrI_3 by a factor of 4.4 (LMCT 1) and 5.4 (LMCT 2) over that of the pristine case. The $\frac{d\chi}{dT}$ is also derived to estimate any changes in the T_C after photoexcitation at these transitions. From

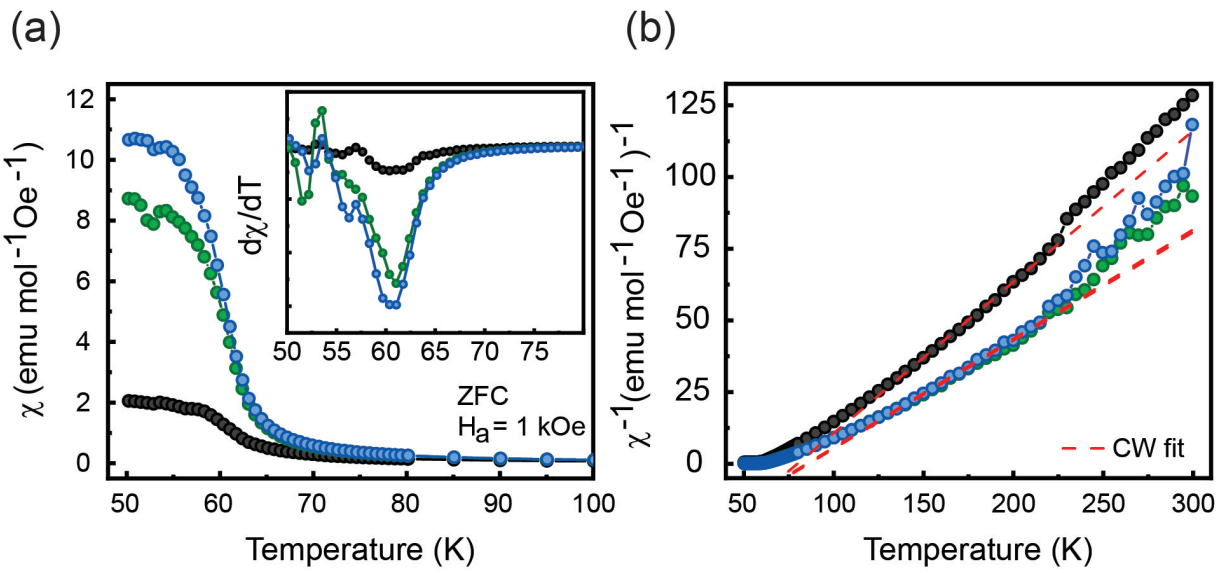

Figure 3.3: (a) $\chi(T)$ measured with a zero-field-cooled (ZFC) protocol and an $Ha = 1\ kOe$ for pristine CrI_3 and both optical excitations of the LMCT 1 (green circles) and LMCT 2 (blue circles) transitions. The inset is the derivative of the $\chi(T)$ $\left(\frac{d\chi}{dT}\right)$ to correctly estimate changes in the T_C. The inverse magnetic susceptibility ($\chi^{-1}(T)$) for pristine, LMCT 1, and LMCT 2 excitations with the Curie-Weiss (CW) law (dotted red line) fitted in the PM phase ($130 - 220\ K$).

the inset of **Figure 3.3 (a)**, no notable change in the T_C was observed with the magnetic phase transition remaining at ~ 61 K after photoexcitation.

Additional information on the magnetic characteristics of photoexcited CrI_3 can be extracted by fitting $\chi^{-1}(T)$ to the CW law as shown in **Fig. 3.3 (b)**. At first glance, a decrease in the $\chi^{-1}(T)$ is observed after photoexcitation at both LMCT transitions. Notably, the pristine $\chi^{-1}(T)$ for CrI_3 shows a kink at around 220 K indicating the presence of the structural transition temperature (T_S)

Table 3.1: Magnetic parameters extracted from the CW fit of pristine CrI_3, and after photoexciting the LMCT, and the *d-d* transitions. C is the Curie constant, Θ_{CW} is the Curie-Weiss temperature, μ_{eff} is the effective moment, and J is the nearest-neighbor exchange interaction.

Parameters	C (emu K mol^{-1})	Θ_{CW} (K)	μ_{eff} (μ_B)	J (meV)
Pristine	1.8965	79.8	3.895	0.917
LMCT 1	2.6504	86.1	4.604	0.989
LMCT 2	2.6337	85	4.59	0.977
d-d 1	4.9319	68.5	6.281	0.787
d-d 2	4.0951	70.7	5.723	0.812

as is expected for this material [83]. By fitting the CW law to the $\chi^{-1}(T)$, the effective moment ($\mu_{eff} = \sqrt{8C}\ \mu_B$) and nearest-neighbor exchange interaction ($J = \frac{k_B \Theta_{CW}}{2S(S+1)}$) were estimated [30]. The parameters extracted from the CW fits are shown in **Table 3.1** for all the optical excitations we employed. For the pristine case, we find that the μ_{eff} = 3.895 μ_B is quite close to the calculated moment for Cr^{3+} of 3.87 μ_B/Cr. After photoexcitation at both LMCT 1 and LMCT 2, an enhancement in the μ_{eff} is found with values of 4.60 and 4.59 μ_B, respectively. Such an enhancement points towards the creation of the high spin-state Cr^{2+} ($S = 2$) due to the similarities in the effective magnetic moment of divalent Cr in an octahedral environment (4.8 μ_B) [41]. As for the estimated exchange interaction extracted from C for pristine CrI_3, it is found to have a value of 0.917 meV which is quite close to the previously reported nearest-neighbor exchange interaction of 0.9 meV [82,84]. After optically exciting the sample at both LMCT 1 and LMCT 2, J increases to 0.989 meV and 0.977 meV, respectively.

Section 3.2 - Photoexcitation with *d-d* transitions

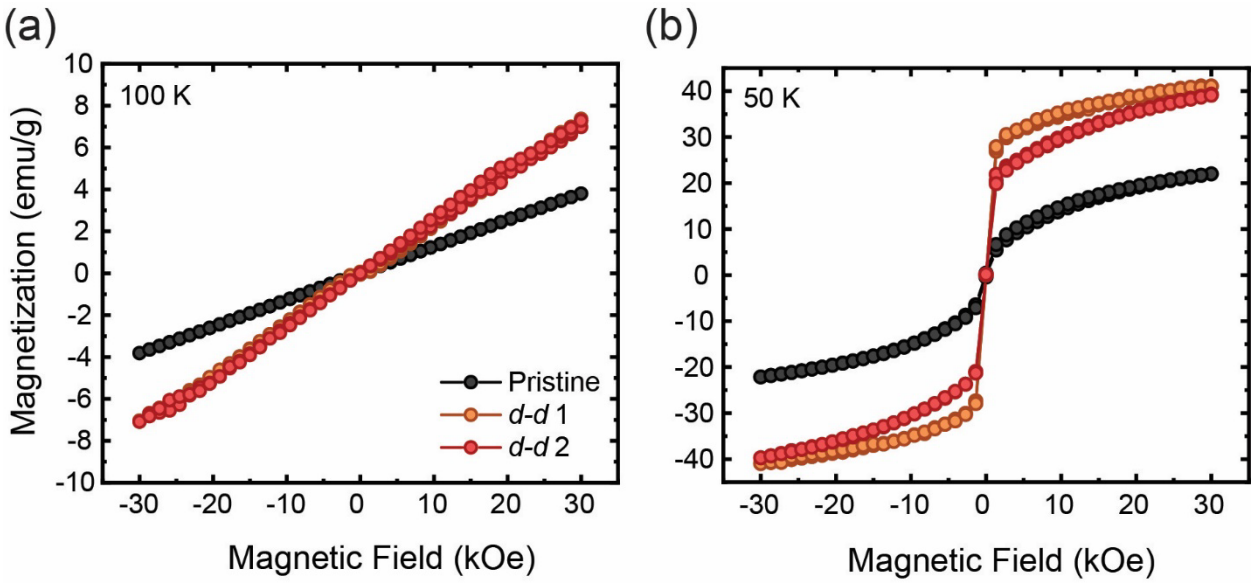

Figure 3.4: M(H) curves measured above (a) and below (b) the $T_C = 60\ K$ for pristine CrI_3 (black circles) and after optical excitation of the *d-d* 1 (orange circles) and *d-d* 2 (red circles) transitions.

This section focuses on optically exciting the *d-d* transitions to modify the magnetic properties of bulk polycrystalline CrI_3. **Figure 3.4 (a, b)** shows the $M(H)$ measurements for pristine and with *d-d* transition excitations collected above (100 K) and below (50 K) the T_C. Within the PM phase (100 K), the magnetization of CrI_3 increases by a factor of 1.75 over the original magnetization after optically exciting the sample at each *d-d* transition, similar to the effect observed for LMCT optical excitations. In this case, the increase in magnetization is slightly lower than that of the LMCT cases. Below the T_C (50 K), optical excitation at the *d-d* transitions also enhance the magnetization to a value of 40 emu/g (~3 μ_B/Cr) at 30 kOe which is a factor of 1.8 greater than the pristine magnetization.

Figure 3.5 (a, b) displays the temperature dependent magnetic susceptibility behavior for CrI_3 before and after optical excitation at the *d-d* transitions. In this case, each optical transition enhances the $\chi(T)$ of CrI_3. However, **Figure 3.5 (a)** demonstrates that optically exciting the *d-d* 1 transition has a stronger effect on the magnetization of CrI_3 than the *d-d* 2 transition. This

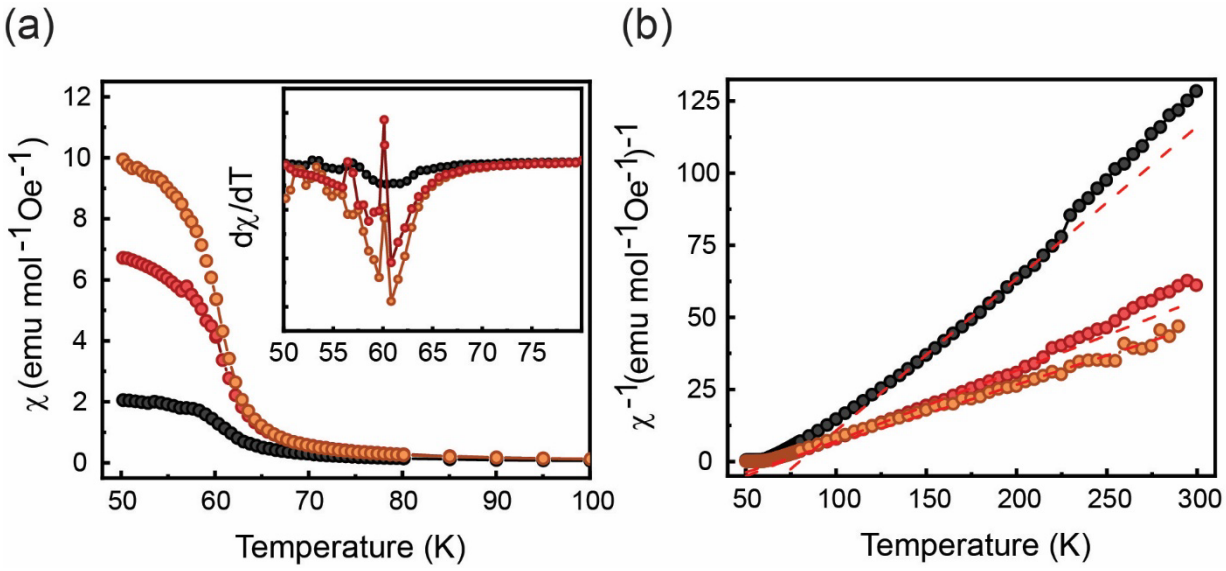

Figure 3.5: (a) $\chi(T)$ measured with a ZFC protocol and an H_a = 1 kOe for pristine CrI_3 and both optical excitations of the *d-d* 1 (orange circles) and *d-d* 2 (red circles) transitions. The inset is $\frac{d\chi}{dT}$ to correctly estimate changes in the T_C. The $\chi^{-1}(T)$ for pristine, *d-d* 1, and *d-d* 2 excitations with the CW law (dotted red line) fitted in the PM phase (130 – 220 K).

enhancement in the magnetization may arise from the fact that the *d-d* 1 transition (1.79 eV) is near the LMCT 1 transition (1.93 eV), possibly enhancing the optical excitation effects coming from the *d-d* 1 transition due to the intermixing of both excitation mechanisms. As for the *d-d* 2 transition, from the introductory part of this section, it is understood that this lowest lying optical transition is weakly allowed within CrI_3, which could explain why the enhancement in $\chi(T)$ is the lowest among all the optical transitions. The $\frac{d\chi}{dT}$ taken after the photoexcitation at the *d-d* transitions (inset of **Fig. 3.5 (a)**) reveals no change in the T_C of this material.

We continue exploring the effects of photoexcitation at the *d-d* transitions by extracting the additional magnetic parameters upon fitting the $\chi^{-1}(T)$ to the CW law (**Figure 3.5 (b)**). The μ_{eff} extracted after optical excitation at both *d-d* transitions reveals an enhancement in μ_{eff} with values of 6.281 μ_B and 5.723 μ_B, for the *d-d* 1 and *d-d* 2 transitions, respectively. The extracted μ_{eff} values for these optical excitations exceed that of the values expected for a photoinduced Cr^{2+} high spin state (4.8 μ_B). Despite this significant enhancement in the μ_{eff}, the estimated *J* decreases for both *d-d* optical excitations to 0.787 meV and 0.812 meV for *d-d* 1 and *d-d* 2, respectively. The changes observed in the magnetic parameters of CrI_3 after optically exciting the *d-d* transitions differ from the LMCT transitions, pointing towards a different mechanism behind the enhancement.

To verify if the light-induced magnetization enhancement is related to these specific optical transitions, we further explored other photoexcitation energies. **Figure 3.6** shows the magnetization of CrI_3 taken at 30 kOe at various optical excitation energies. It becomes clear from this plot that only the *d-d* and LMCT optical excitations induce an enhancement in the magnetization. While optically exciting CrI_3 with energies farther away from the *d-d* and LMCT

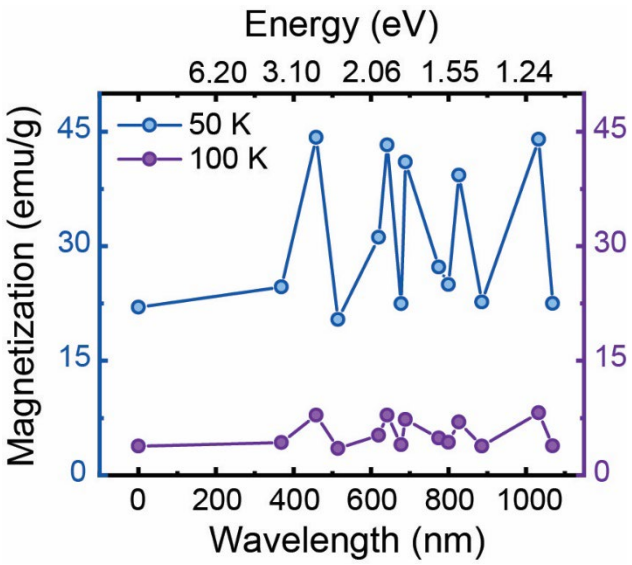

Figure 3.6: The magnetization taken from the M(H) curves at a max field of 30 kOe measured above (light blue circles) and below (purple circles) the T_C for CrI_3 at all the applied photo-excitations.

transitions either have no effect or slightly decrease the magnetization. Additionally, exciting CrI_3 with an energy close to its bandgap (1.2 eV) also shows an enhancement compared to that of the LMCT 2 transition. It is quite likely that optically exciting CrI_3 near its bandgap may still excite carriers in the system inducing changes in its magnetic properties.

Section 3.3 - Discussion

When looking at the changes in magnetization produced by the photoexcitation of each of these optical transitions, a significant modification in the magnetic properties of CrI_3 is clearly visible for each individual case. The enhancement in the μ_{eff} changes upon the application of each optical excitation leading to the assumption of two possible scenarios, specifically for the LMCT transitions. The first scenario paints a picture of the optical excitations leading to a photo-induced transition from the trivalent Cr state to a photoexcited Cr^{2+} state as evidenced by the increase in the μ_{eff}. An example of this can be taken from a light-induced ferromagnetic resonance (FMR)

study of $CdCr_2Se_4$ revealing a modification of the FMR properties attributed to a photoinduced Cr^{2+} excited state of the Cr^{3+} in this material [85].

The second scenario comes in the form of the modification of the FM phase through the enhancement of the orbital interactions [86–88]. In particular, recent first-principle calculations studied the effects of photoexcitation on monolayer CrI_3 using the LMCT 2 transition (~ 2.7 eV) [88]. The authors traced the charge transfer between the ligand and metal sites establishing that the carrier excitation takes place between the *p-d* transitions. Moreover, another theoretical group [89] established a different perspective to the magnetism in monolayer CrI_3 by taking into account the orbital magnetism. The authors note that there is a competition between the conventional super-exchange interaction between the occupied $t_{2g} - t_{2g}$ orbitals (AFM) and the virtual transitions between the occupied and unoccupied $t_{2g} - e_g$ orbitals (FM) on two different atoms [89]. However, it is the virtual transitions that dominate the magnetic order in CrI_3 as has been shown in another theoretical study [78]. As demonstrated earlier, photoexciting at the LMCT transitions causes an increase in the exchange interaction resulting in a significant enhancement in the magnetization. A similar observation was reported on the light-induced effects on (Co, Fe) Prussian blue compounds, attributed to electron transfer between the orbitals of the magnetic ions [86]. Another similar type of enhancement in the magnetization of GaMnAs [87] through optical excitation was assigned to an alteration to the exchange interactions. Both studies support our observation of the LMCT transitions causing an enhancement in the exchange interaction in CrI_3. It is quite possible that both scenarios occur together. Hypothetically, the photoexcitation of CrI_3 at these LMCT transitions drives the creation of photoexcited Cr^{2+} centers, thus resulting in an enhancement in the exchange interaction strength.

To gain better understanding of underlying mechanism behind the effect caused by the *d-d* optical excitations, we turn to an ultrafast photoexcitation study performed by Mikhaylovskiy et al [90]. The authors targeted *d-d* transitions on iron oxides using ultrafast pulses of light to optically control the exchange interactions in these magnetic systems by modulating the ratio $\frac{J}{D}$ where J is the exchange interaction and D is the Dzyaloshinkii-Moriya interaction [90]. Both of these interactions coexist within CrI_3, particularly, the D interaction, which was corroborated through an inelastic neutron scattering study, evidenced by the separation between the acoustic and optical spin-wave branches [91]. The study performed by Mikhaylovskiy et al argued that the perturbation of the exchange ratio triggers an antiferromagnetic resonance [90,92] which is seen as an Impulsively Stimulated Raman Scattering (ISRS) process. In fact, by optically exciting CrI_3 with the *d-d* 2 transition (~ 1.55 eV), Padmanabhan et al were able to coherently drive phonon oscillations through the ISRS process. More importantly, not only did they observe a phonon oscillation linked to the ferromagnetic ordering in CrI_3 (at 3.87 THz), the authors also observed an additional phonon mode (at 3.73 THz) that arises from the known antiferromagnetic ordering in CrI_3 [82]. The fact that they were able to observe this AFM mode provides some support for the enhancement in the magnetization in the experiments presented here through the optical excitation of the *d-d* transitions. Even though the optical excitation comes from a noncoherent and unpolarized light source, one can infer that optical excitation of CrI_3 with these *d-d* transitions can cause an excitation between *3d* metal centers, hence modify J/D.

Section 3.4 - Summary

In this chapter, the magnetic properties of bulk polycrystalline CrI_3 are studied upon photoexcitation with the specific optical transitions. Optical excitation of CrI_3 at the LMCT

transitions revealed the presence of photoexcited high-spin Cr^{2+} state, accompanied by an enhancement in the intralayer exchange interaction, resulting in an enhanced magnetization of CrI_3. Additionally, targeting the two *d-d* transitions shows a significant enhancement in the effective moment of Cr that exceeds the value of high-spin Cr^{2+} with a reduction in the estimated exchange interaction. Upon comparison with other works that optically excite magnetic systems with *d-d* transitions, it is hypothesized that a modification of the exchange ratio can occur when exciting an electron spin between the metal *3d* orbital centers within CrI_3. Additionally, optically exciting CrI_3 with photon energies away from these electronic transitions does not result in an enhancement in the magnetization. These experiments provide initial evidence of the ability to modify the magnetic properties of van der Waals magnets through noncoherent light sources. To better understand the photo-induced magnetic properties of the materials studied in this Chapter, we employed electron paramagnetic resonance (EPR) spectroscopy, as discussed in the following Chapter.

Chapter IV - Photo-induced EPR properties of van der Waals CrX_3 magnets

In this chapter, we discuss out efforts to capture the light-induced changes on the magnetic properties of CrX_3 vdW magnets through EPR spectroscopy [93]. As stated in section 2.2, EPR spectroscopy has the potential to provide a better understanding on the local magnetic interactions upon photoexcitation.

The CrX_3 family of vdW magnets were the first to raise considerable interest within the condensed matter community. Specifically, CrI_3 was one of the first vdW magnets revealed to possess long range magnetic ordering in its monolayer form, leading to a large number of investigations [16,75,94–96]. This family of materials consist of a naturally layered honeycomb structure with the majority of them possessing a structural stacking transition from monoclinic to rhombohedral at 220 K and 256 K for CrI_3 and $CrCl_3$, respectively [83,97]. Additionally, they are known to have ferromagnetically aligned spins within each layer while the interlayer exchange interactions can be antiferromagnetic [98–103]. CrI_3 displays an overall FM phase with a T_C of ~ 60 K [83] in its bulk form and when reduced to tens of layers its magnetic ordering becomes AFM with a lower ordering temperature of 45 K [100]. In its bulk form, CrI_3 possess a bandgap of 1.2 eV and higher energy optical transitions such as LMCT and *d-d* transitions [71]. Similarly, $CrCl_3$ is also a ferromagnet with its spins pointing within the plane with an ordering temperature of 17 K, while also possessing antiferromagnetic behavior in the out-of-plane direction. This magnet is unique in that it's out-of-plane magnetic ordering can be tuned from AFM to FM by applying a small magnetic field ($H_a \geq 6$ kOe) [97]. Additionally, $CrCl_3$ possesses a large bandgap (3.1 eV) that is also optically active, containing two electronic transitions within its band gap [97]. While most of the prior works employed optical probes to study the magnetic properties of these materials, no prior research has been conducted on the light-induced EPR spectral properties of

CrX_3. This chapter showcases the light-induced effects on the local magnetic interactions within the CrX_3 bulk compounds through the lens of EPR spectroscopy. The data presented in this chapter will serve as a basis for understanding the magneto-optical phenomena in their few-layered structures.

Section 4.1 - Magnetic characterization and light-induced EPR of $CrCl_3$

Before starting the light-induced EPR spectroscopic measurements, the magnetic properties for $CrCl_3$ were verified through magnetometry. **Figure 4.1 (a)** shows the $\chi(T)$ behavior of $CrCl_3$ down to 2 K. From the inset in **Fig. 4.1 (a),** the T_C can more accurately be estimated and is found to be $\sim$17 K, matching that of previous reports [97,104]. The isothermal $M(H)$ behavior of $CrCl_3$ is also shown in **Fig. 4.1 (b)** demonstrating FM behavior in the $H//c$ as is expected of this material.

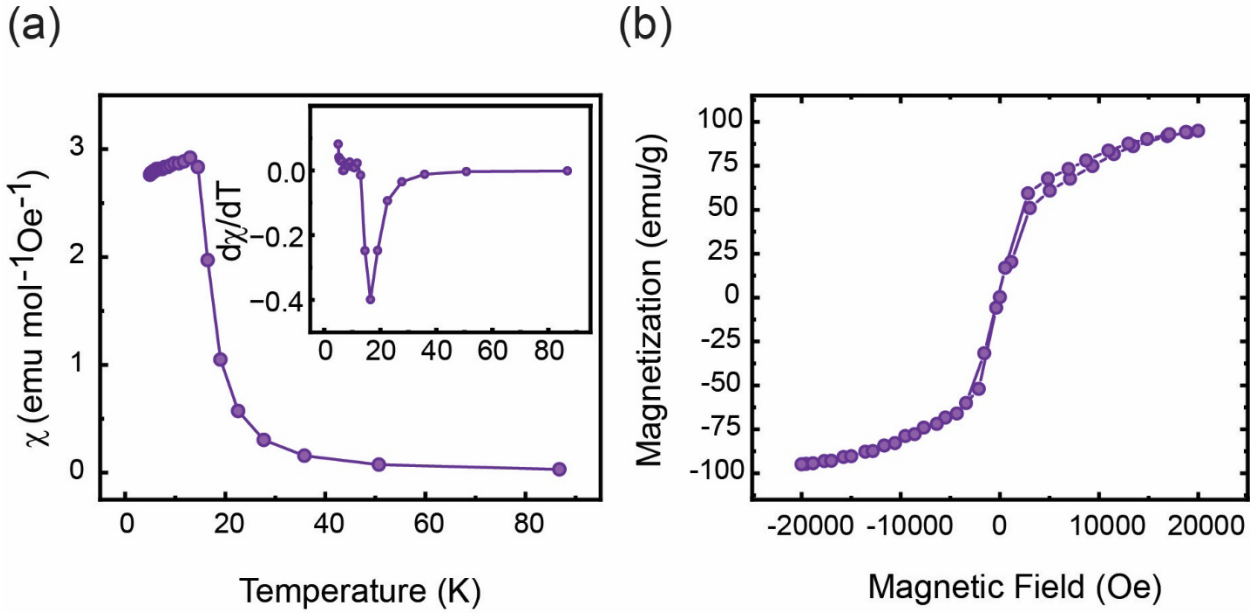

Figure 4.1: (a) $\chi(T)$ measured with a ZFC protocol with an applied field (H_a) of 0.5 kOe in the out-of-plane (H//c) direction. The inset shows the derivative of the $\chi(T)$ $\left(\frac{d\chi}{dT}\right)$ curve to correctly estimate the T_C. (b) The M(H) curve measured at 2 K was also taken along H//c.

For the light induced EPR measurements on the CrX_3 vdW magnets, we utilize a broadband white light source for photoexcitation. **Figure 4.2 (a – d)** presents the EPR signals of $CrCl_3$ at 10 K, 20 K, 50 K, and 100 K when the white light source is off (I_{off}) and then turned on (I_{on}). Additionally, the difference between the signals ($\Delta I = I_{on} - I_{off}$) is calculated and clearly shows the intensity difference between the two states. At 10 K, the weak signals noted at slightly lower fields than the main signal are thought to come from small FM inhomogeneity or isolated Cr^{3+} ions

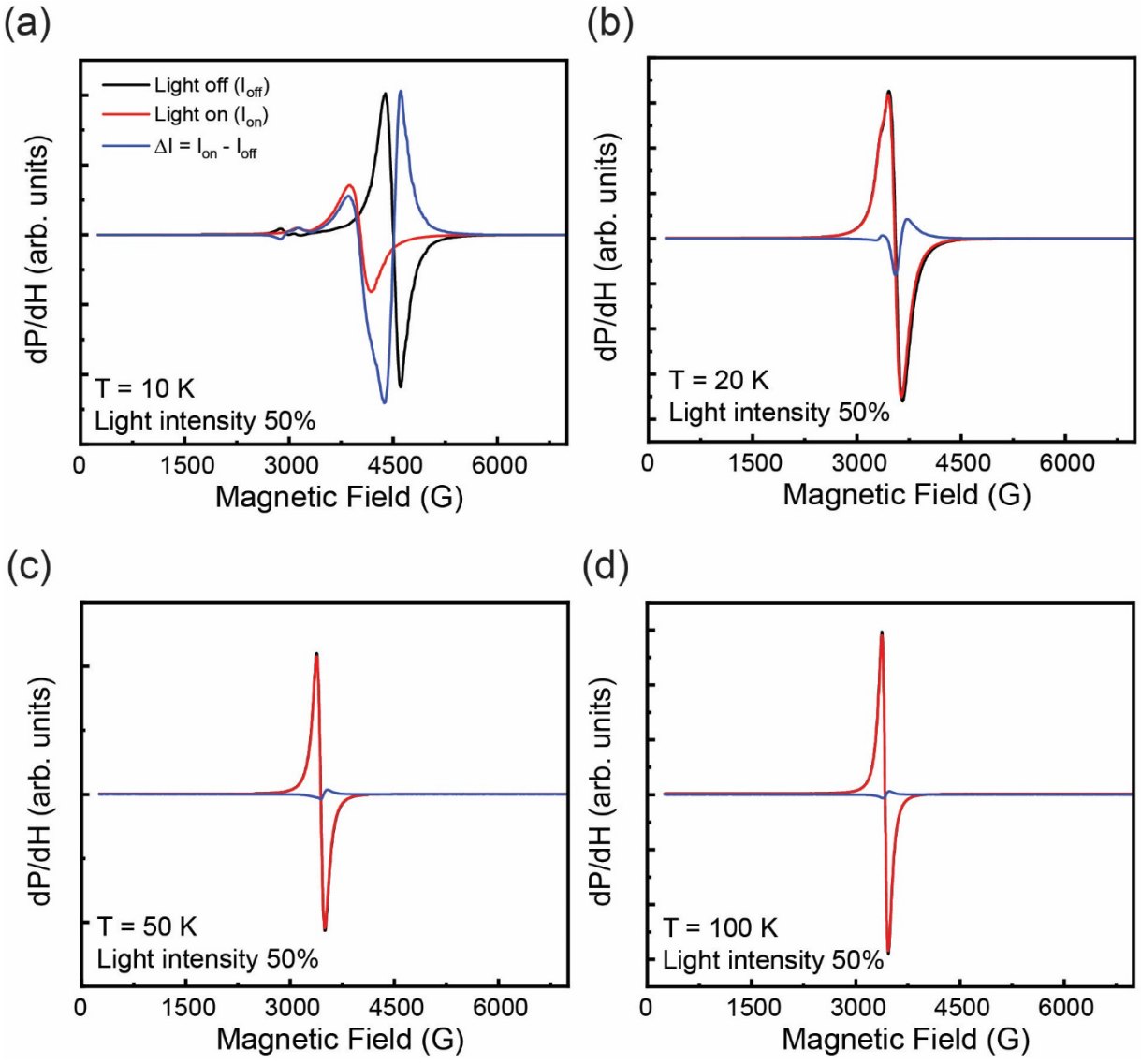

Figure 4.2: The EPR spectra obtained for $CrCl_3$ at (a) 10, (b) 20, (c) 50, and (d) 100 K. Each plot provides the spectra with the light off (I_{off}), the light on (I_{on}), and the difference between the two states (ΔI). The light intensity for all temperature points were kept at 50% intensity.

within the material that disappear as temperature increases [105]. Within the FM phase of $CrCl_3$ (**Fig. 4.2 (a)**), a clear change in the EPR signal centered at ~ 4500 G is observed in the I_{on} state to a center field of ~ 3870 G with a significant change in the signal intensity. The biggest change is observed within the FM phase and as temperature increases, the changes become less apparent, as shown in the ΔI signals. To further elucidate the EPR parameter space of the signals observed

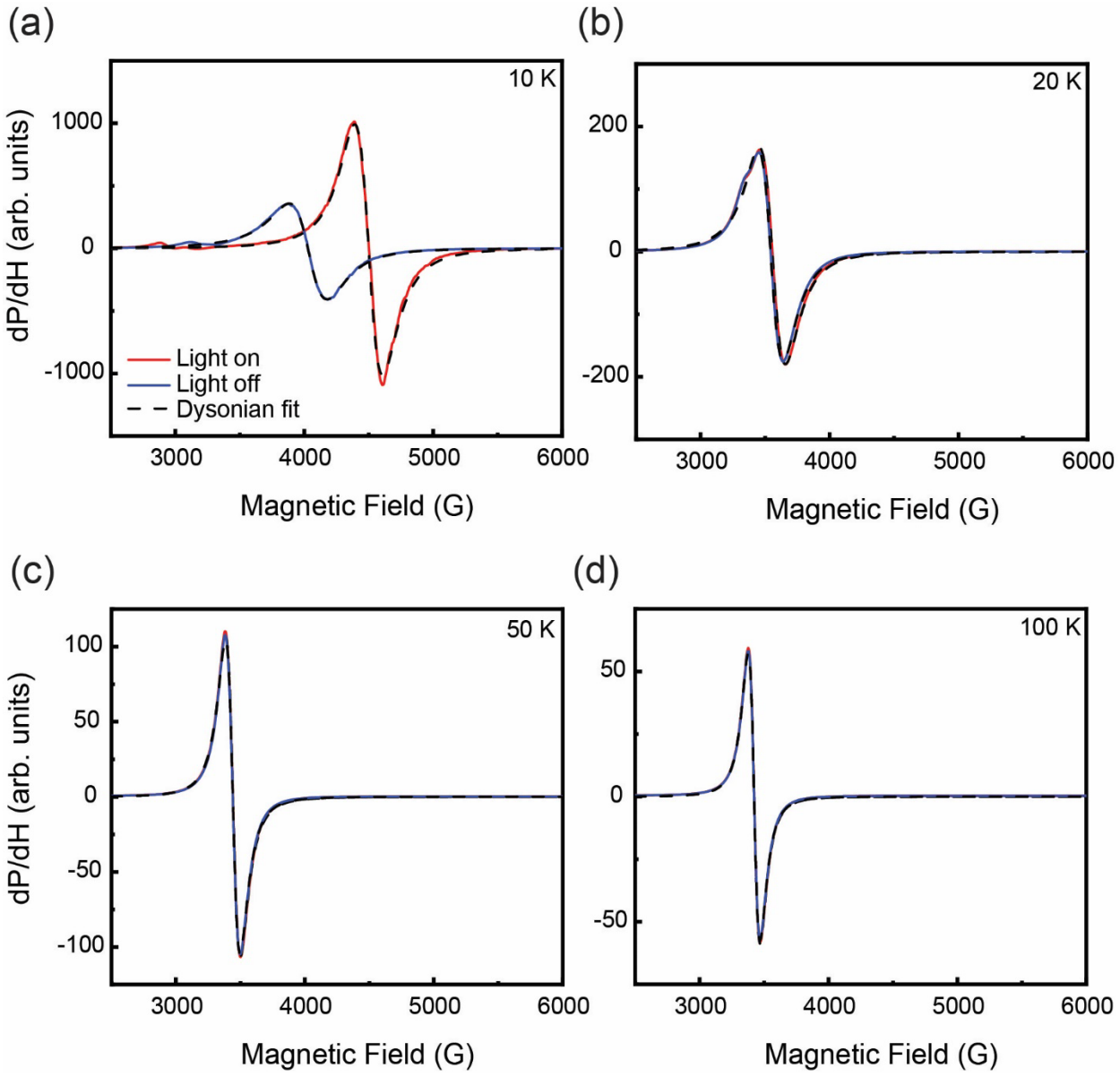

Figure 4.3: The I_{on} (red line) and I_{off} (blue line) states are shown for (a) 10, (b) 20, (c) 50, and (d) 100 K with the computer-generated fits (dotted lines) using the Dysonian line-shape from Eq. 2.3.

in $CrCl_3$, a Dysonian line shape (Eq. 2.3) is used to fit the data. This line shape is applied here due to the signal's slight asymmetry [45,106,107], particularly within the FM phase. The signals fitted with Eq. 2.3 are shown in **Fig. 4.3 (a – d)** demonstrating excellent reproduction of the experimental data for the I_{off} and I_{on} states.

The EPR spectral parameters extracted from Eq. 2.2 and Eq. 2.3, including the g-value, I, and H_{pp}, plotted in **Fig. 4.4 (a – c)** as a function of temperature. The strongest change in $CrCl_3$'s EPR properties can be observed within the FM phase, similarly observed from the ΔI plots in **Figure 4.2.** It's g-value shifts from 1.5 in the I_{off} state to 1.67044 in the I_{on} state, followed by a broadening of its H_{pp} from $265.9\,\mathrm{G}$ to $357.5\,\mathrm{G}$, and a reduction in the signal intensity. Additionally, at 10 K, the asymmetry parameter (α) increases from -0.037 ± 0.006 to -0.221 ± 0.004 when going from the I_{off} to the I_{on} state. The EPR signal parameters in the I_{off} state match that of previously reported g-value, H_{pp}, and H_o for Cr^{3+} ions ($S = 3/2$) in the octahedral environment of $CrCl_3$ [108]. The observed change in the signal intensity and asymmetry is attributed to a change in the penetration depth of the radiation provided by the light source [109] similarly observed in another Cr^{3+} hosting compound $CdCr_2Se_4$.

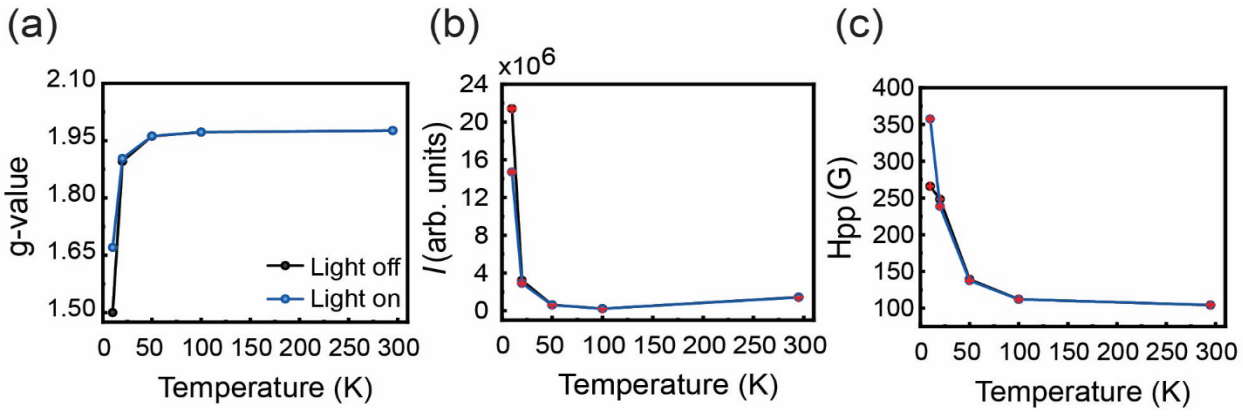

Figure 4.4: $CrCl_3$ temperature dependent EPR spectral parameters such as its (a) g-value, linewidth (H_{pp}), and (c) the signal intensity (I) are shown in the light OFF (black) and ON (blue) states with error bars for I and H_{pp} (in red).

We now look at the EPR signal intensity as a function of time, as shown in **Fig. 4.5 (a - d)**, measured at 10 K and 20 K. In **Figure 4.5 (a)**, the EPR intensity is measured at a fixed field of 3870 G, which is the maximum peak field of the I_{off} state in the EPR signal for $CrCl_3$. Applying 50% of the light source's intensity induces a drop in the EPR signal intensity with a decay time

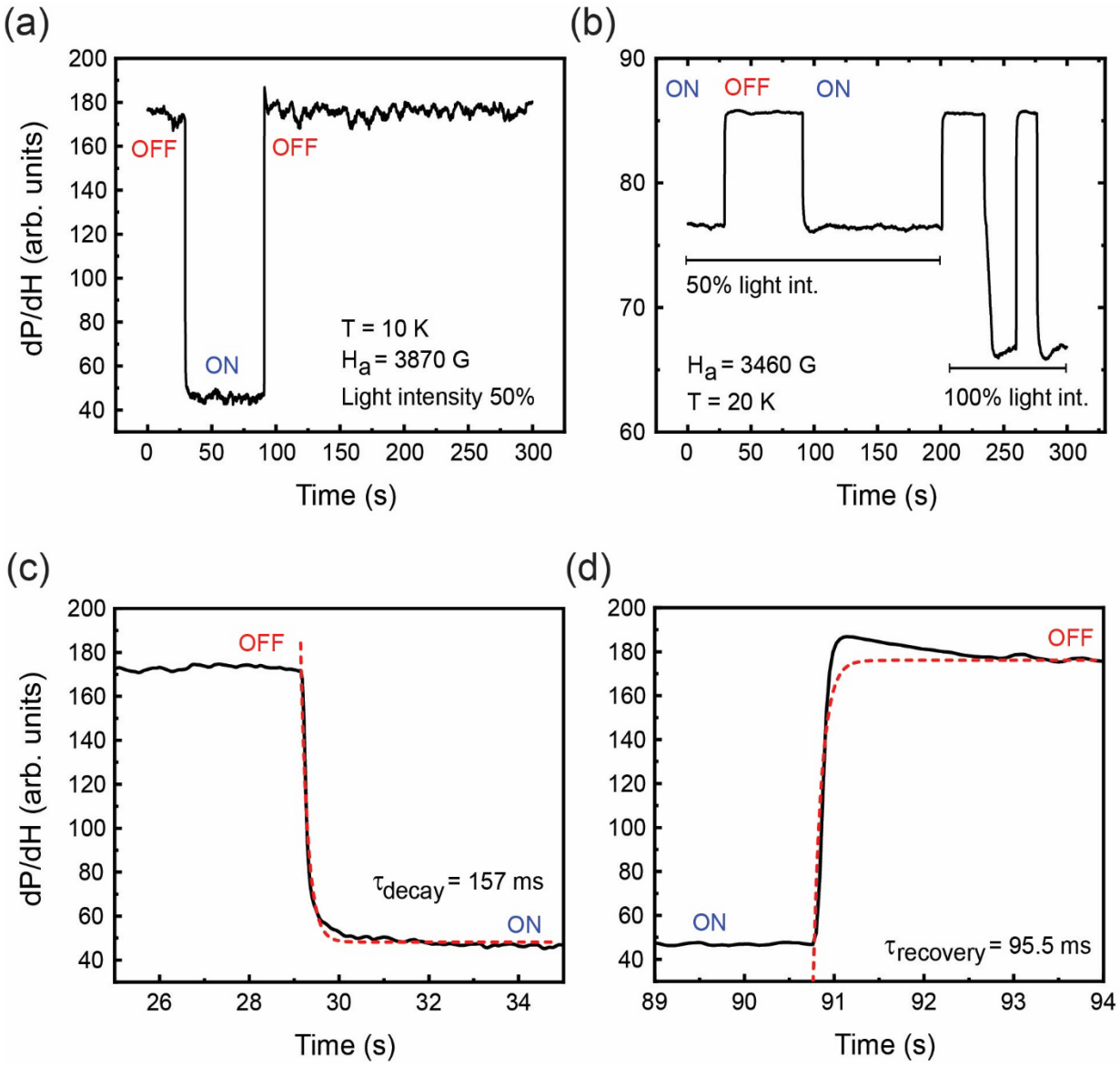

Figure 4.5: The time traces of the EPR signal measured at (a) 10 K at a fixed field of 3870 G which is the H_o of the main signal. with OFF and ON state at a 50% light intensity demonstrating a decrease in the signal intensity. While (b) shows the time trace taken at 20 K, at a fixed field of 3460 G, with ON and OFF states at 50% and 100% light intensity. (c) and (d) are a closer look to the decay and recovery of the EPR signal intensity for (a). Both are fitted with a single exponential to extract τ_{decay} and $\tau_{recovery}$.

(τ_{decay}) of 157 ms. The τ_{decay} was obtained by fitting the time-dependent EPR signal intensity with a single exponential $I = Ae^{-\frac{\tau}{t}}$, where A is the decay amplitude and τ is the decay time. Once the light is turned off, $CrCl_3$ experiences a full recovery after a recovery time ($\tau_{recovery}$) of 95.5 ms. A similar experiment is shown in **Fig. 4.5 (b)** performed at 20 K, this time the light intensity is varied between 50% and 100% demonstrating the clear intensity dependence of the EPR signal intensity.

Section 4.2 - Light-induced EPR properties of CrI_3

The focus will now shift to the experimental findings of the light-induced EPR properties for CrI_3. Similar to $CrCl_3$, the magnetic properties of CrI_3 are verified through magnetometry as is shown in **Fig. 4.6 (a, b)**. The ZFC $\chi(T)$ measurement demonstrates the typical FM behavior expected from CrI_3 with a T_C at 61 K, confirmed by the $\frac{d\chi}{dT}$ in the inset of **Fig. 4.6 (a)** [83]. Additionally, we capture the isothermal magnetization behavior expected for CrI_3 at 50 K shown

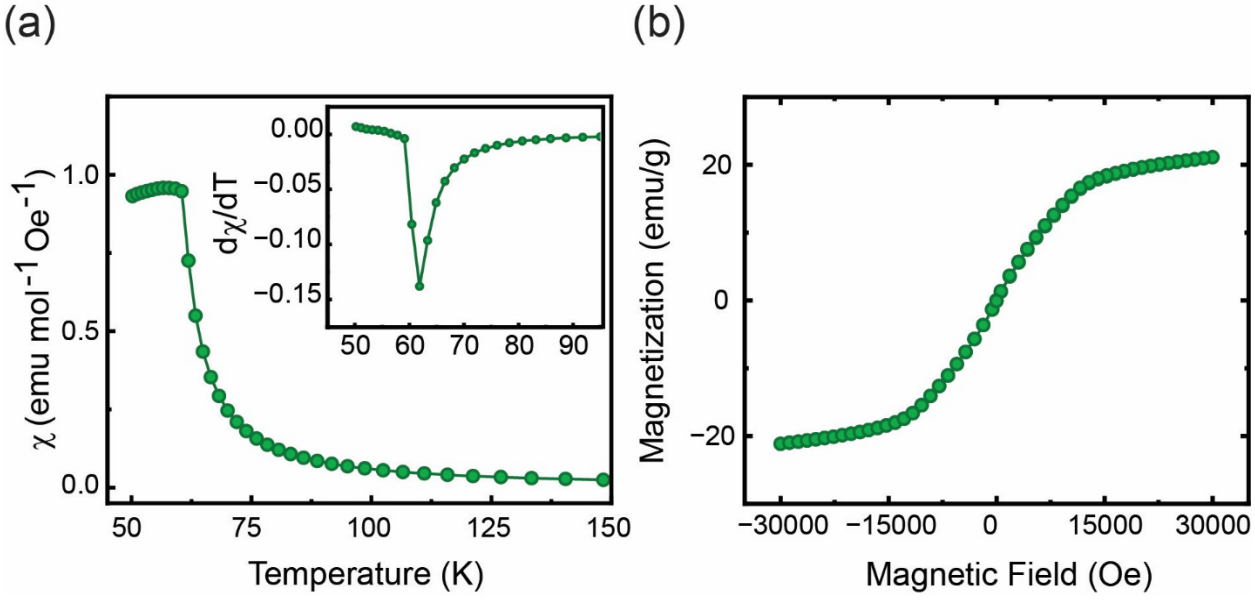

Figure 4.6: (a) shows the ZFC $\chi(T)$ curve taken with an $Ha = 0.5\,kOe$ and inset is the derivative to better estimate the T_C. Also shown is the isothermal M(H) measurement (b) taken at 50 K. Both (a) and (b) were also captured along the H//c direction.

in **Fig. 4.6 (b)**. After confirming the magnetic properties of CrI_3, the light-induced EPR properties were studied with confidence.

The EPR spectra for CrI_3 were taken across the magnetic phase transition (10 K, 30 K, 60 K, 65 K, and 100 K). However, the EPR signals collected below the ferromagnetic phase were irreproducible (see **Figure 4.7 (a, b)**). This might have been the case because of strong interactions

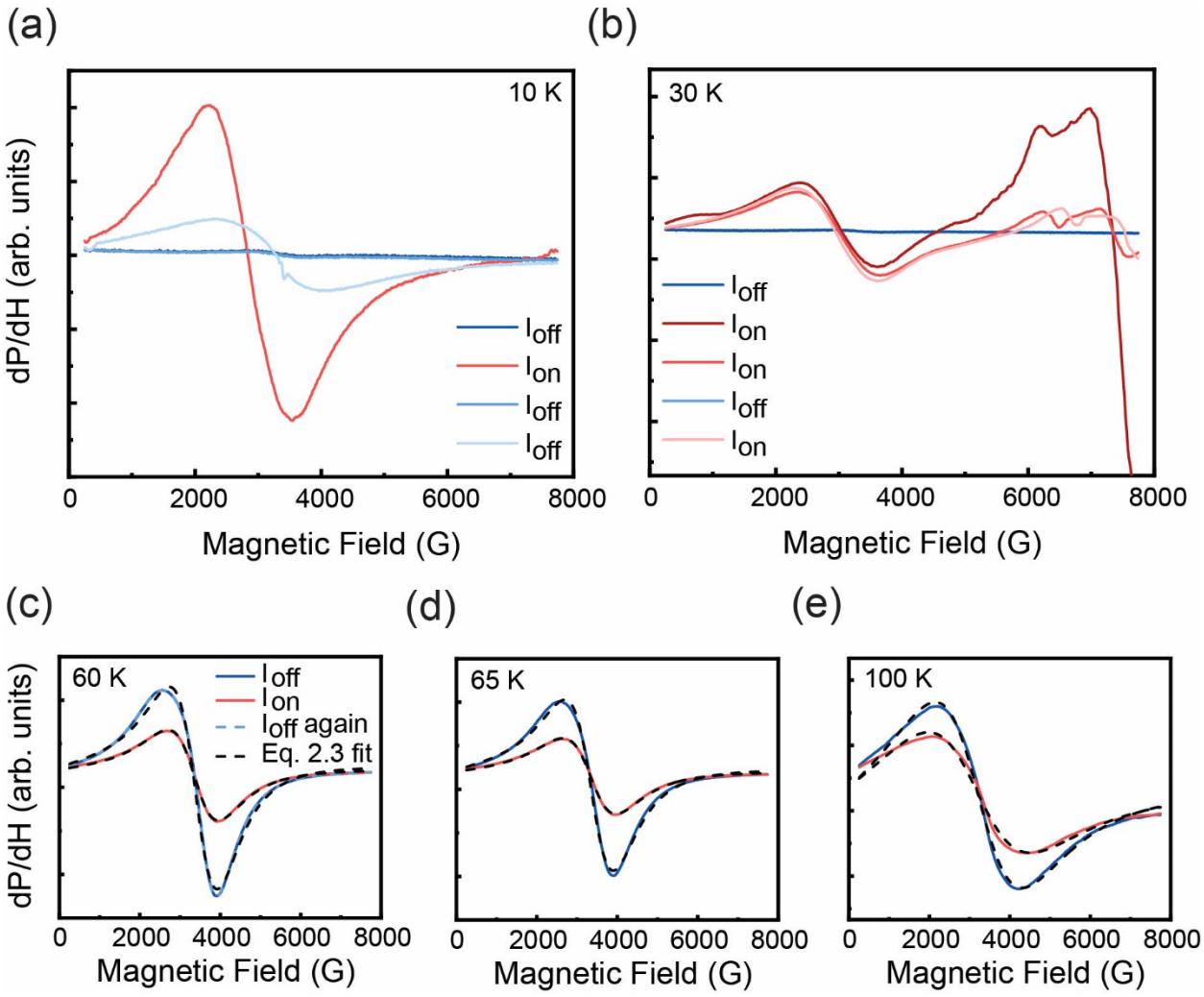

Figure 4.7: EPR signals of CrI_3 in the I_{on} (red) and I_{off} (blue) states at (a) 10, (b) 30, (c) 60, (d) 65, and (e) 100 K. Various EPR spectra are shown for the data collected at 10 and 30 K repeatedly turning the light source on and off to demonstrate the irreproducibility of the signals within the FM phase. The blue dotted line in (c) shows the EPR signal for CrI_3 when the light is set to the OFF state after the ON state (signal overlaps with the initial OFF state signal). The black dotted line in (c), (d), and (e) represents the Dysonian fit to the experimental signals.

with light and the magnetic domains, which causes instability in the FM domains of CrI_3 [110]. Even after field-cooling the sample with $H_a = 3000$ Oe to produce a single FM domain, it was difficult to obtain reproducible data. Therefore, the focus will be on the measurements performed at 60 K and above. The rest of **Figure 4.7 (c – d)** shows the data collected at and above the T_C with EPR spectra in the I_{off} and I_{on} states. At first glance, a clear decrease in the signal intensity is observed along with a slight asymmetry in the EPR signals. The signals measured for CrI_3 were also fitted with Eq. 2.3 to extract the g-value, H_{pp}, and I as shown in **Fig. 4.8 (a – c)** also demonstrating good fitting between Eq. 2.3 and the experimental data. At 60 K, a shift in the g-value is observed for CrI_3 from 1.956 to 1.990 followed by a broadening of the EPR linewidth from 1170 G to 1260 G after exposure to light. Lastly, **Fig. 4.8 (c)** shows a quenching in the EPR signal intensity by a factor of ~1.9 after light exposure at 60 K with a decrease in the asymmetry parameter from -0.689 ± 0.008 to -0.367 ± 0.003.

The time-dependent light-induced EPR intensity change was also recorded for CrI_3 as shown in **Fig. 4.9 (a - d)** measured at 60 K and 100 K. The time-dependent EPR signal intensity is shown to vary with the light intensity (25%, 50%, 100% power intensity) demonstrating that

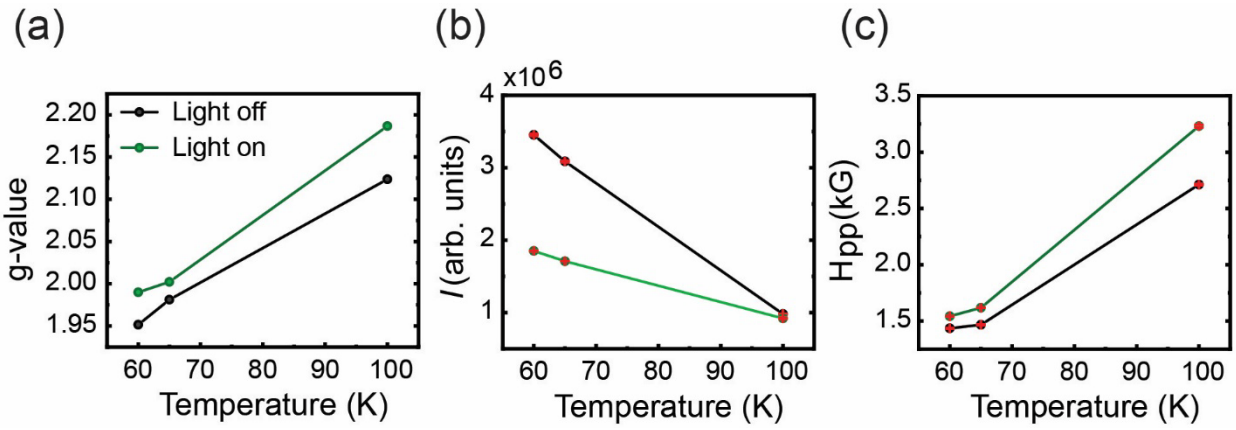

Figure 4.8: The temperature dependence of the (a) g-value, (b) H_{pp}, and (c) I obtained from Eq. 2.3 for the light off (in black) and light on (in green) states from CrI_3 with the error bars in (b) and (c) shown in red.

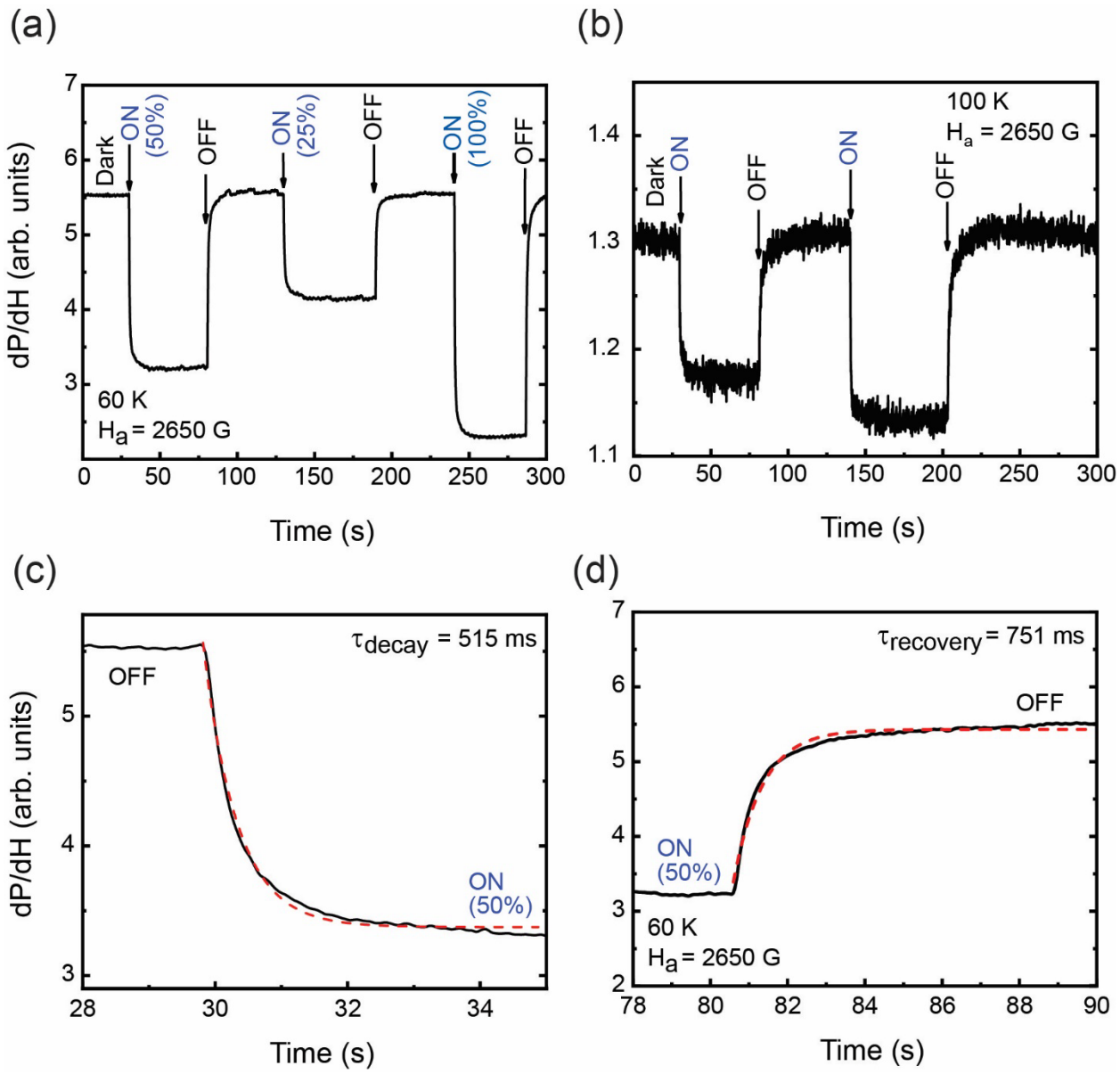

Figure 4.9: The time evolution of the EPR signal intensity measured at (a) 60 and (b) 100 K showing a sudden decrease in the signal intensity in the light ON state. The EPR signal intensity also shows a larger decrease when the light intensity increases. The EPR intensity decay (c) and recovery (d) timescales are also shown.

near its T_C the EPR signal for CrI_3 can recover back to its original state. Time constants were also extracted using a single exponential with decay and recovery times of 515 ms and 751 ms, respectively. The decay and recovery times for CrI_3 are notably longer than that of $CrCl_3$ shown previously. For both $CrCl_3$ and CrI_3, their $\tau_{recovery}$ is close to that of the excited lifetime for Cr^{3+} doped Al_2O_3 [111]. A longer recovery time for both materials may come from their bulk nature

containing larger amounts of Cr^{3+} centers. Notably, the g-value and linewidths between CrI_3 and $CrCl_3$ are quite distinct. This difference is attributed to a stronger magnetic anisotropy in CrI_3 coming from strong spin-orbit coupling from the I^- halide, exceeding that of Cr^{3+} or Cl^- by more than an order of magnitude [83,97,104,112].

Section 4.3 - Discussion

The findings we observe in $CrCl_3$ resemble that of previous reports [60,85,109] on the light-induced magnetic changes in the ferromagnetic semiconductor $CdCr_2Se_4$, which also a host to Cr^{3+} ions. The report shows that the EPR spectral properties, such as resonance field, linewidth, and signal intensity, change within the material's FM phase, while no changes were observed in the PM phase. This is quite similar to our findings on $CrCl_3$, leading to a similar explanation of the

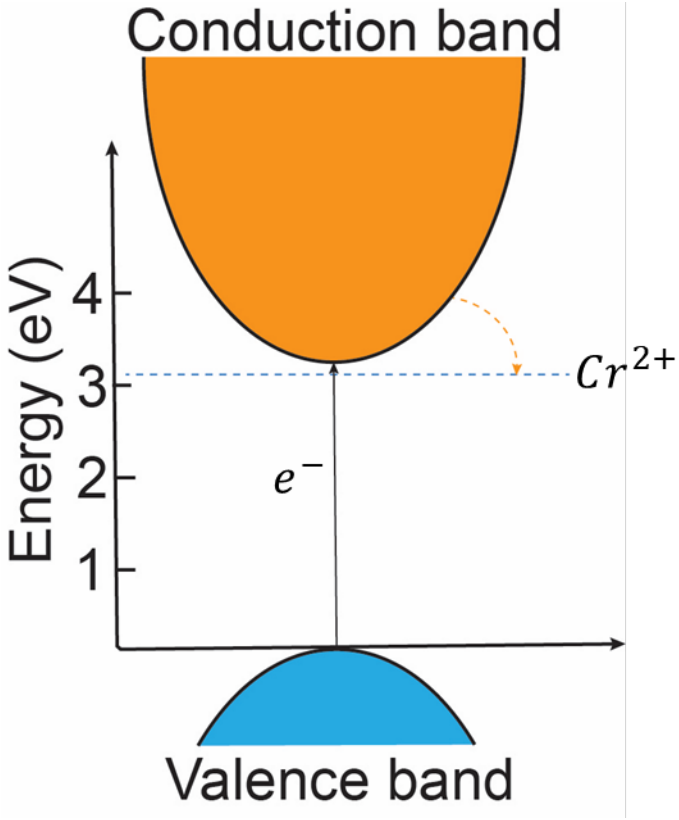

Figure 4.10: Band schematic for $CrCl_3$ depicting an electron being excited from the valence to the conduction band at 3.1 eV and then transitioning to an inter-band transition for Cr^{2+} electrons.

light-induced effects observed here. The idea is that the photoexcited electrons from the valence band are trapped within the octahedral Cr^{3+} sites, creating Cr^{2+} centers ($Cr^{3+} + e^- \rightarrow Cr^{2+}$). These photogenerated Cr^{2+} ($3d^4$ and $S = 2$) centers are assumed to be form between the valence band and conduction band, with energy levels situated 0.08 eV below the conduction band (see **Fig. 4.10**). The photo-induced decrease in the EPR signal intensity may be caused by the photoexcitation of electron transitions between the Cr^{2+} levels and the broad conduction band from which the recombination process occurs faster. To note, Cr^{2+} EPR signals could not be detected in the X-band frequency range at any of the measured temperatures, due to a shorter relaxation time and high zero field splitting [113].

Section 4.4 - Quantum Chemistry Calculations

The changes observed in the g-value and the temperature-dependent H_{pp} can be explained by accounting for two different mechanisms: (i) a slow relaxation in which the observed changes are attributed to Cr^{2+} and (ii) the appearance of random low-symmetry fields acting on the Jahn-Teller Cr^{2+} ions on the octahedral sites. To gain greater insight onto the relationship between the change in g-value with the light-induced Cr^{2+} centers for both CrI_3 and $CrCl_3$, our collaborators, from Ecole Polytechnique Federale de Lausanne in Switzerland, implemented Quantum Chemistry Calculations using a Hartree-Fock approximation, which optimizes the variations of the spin orbitals [114]. This modeled approximation contains Cr-centered octahedral units with the inclusion of an embedded array of point charges fitted to the Madelung potential of the crystal structure. Additionally, they implemented a multiconfigurational wavefunction via the complete-active-space self-consistent-field (CASSCF) computation, a method typically used to describe the electronic structure of bonded molecular systems, specifically, excited states [114]. Lastly, the

EPR g-values for the ($S = 3/2$) ground state of $CrCl_3$ and CrI_3 were determined through the methodology presented in Ref. [115]. These values were estimated to be 1.42 and 1.92 for $CrCl_3$ and CrI_3, respectively. For the light-induced Cr^{2+} excited state the estimated g-values were 1.79 and 2.08 for $CrCl_3$ and CrI_3, respectively. The calculated changes in the g-values are found to be in line with the experimental findings, assuming the reduction of Cr^{3+} to Cr^{2+} ions observed in the light-induced EPR spectral evolution. The slight discrepancy between the QCC and the experimental findings is associated with partial conversion of Cr^{3+} to the photoexcited Cr^{2+} state.

With the help of the QCC, it is understood that the CrX_3 materials under photoexcitation consist of two subsystems; (i) ferromagnetically ordered Cr^{3+} ions, with a quenched spin-orbit coupling, and (ii) photo-generated Cr^{2+} ions which are characterized by having strong spin-orbit coupling ($40 - 60\ cm^{-1}$). The two subsystems couple with each other via a generally anisotropic exchange interaction. With the two subsystems interacting with each other, it causes a slowing down of the spin dynamics due to the introduction of the spin-orbit coupling from the Jahn-Teller distorted Cr^{2+} ions. The observed photo-induced changes in the g-value and linewidth of CrI_3 are greater due to a larger spin-orbit coupling from iodine as well as ligand-induced giant magnetic anisotropy [116]. The irreproducibility of the EPR spectral properties within the FM phase of CrI_3 are thought to occur because the photo-induced Cr^{2+} centers interact strongly with the FM domains, changing the domain wall thickness and mobility, similarly observed in $FeBiO_3$ [110].

Section 4.5 - Summary

Clear changes in the EPR spectral properties of two vdW magnets, namely $CrCl_3$ and CrI_3, are observed through CW photoexcitation. Within $CrCl_3$, these changes primarily take place within the FM phase with no discernable changes in the paramagnetic phase. Meanwhile, CrI_3 interacts

strongly with light within its paramagnetic phase, however, the light-induced effects within the FM phase were hard to resolve with X-band frequency. Theoretical calculations support the conversion of Cr^{3+} to photo-induced Cr^{2+} centers due to the shift in g-value for both materials. Lastly, a greater change in the EPR spectral parameters is observed in CrI_3 than $CrCl_3$ due to CrI_3 possessing a stronger spin-orbit coupling and larger magnetic anisotropy coming from its ligand.

Chapter V - Coherent spin-phonon coupling in the layered ferrimagnet $Mn_3Si_2Te_6$

In this Chapter, the magneto-optical properties of $Mn_3Si_2Te_6$ are explored using ultrafast pump-probe spectroscopy [117]. This technique allows us to study the dynamics of novel phenomena such as ultrafast control of magnetic systems [118–120], coherent excitation of optical phonons [121–123], and optically-induced metastable phase transitions [124–126]. This technique is also an essential tool in unraveling the coupling between the electronic, lattice, and spin subsystems on their intrinsic timescales. Furthermore, this technique can be used to identify the *spin-phonon coupling* that has been alluded to in the past in $Mn_3Si_2Te_6$ [127].

Even though vdW magnets have gained popularity, there are many that remain less explored in bulk or few-layer form. One of these materials is $Mn_3Si_2Te_6$, a ferrimagnetic material with similarities to $Cr_2Si_2Te_6$. $Mn_3Si_2Te_6$ is unique within the family of vdW magnets due to its self-

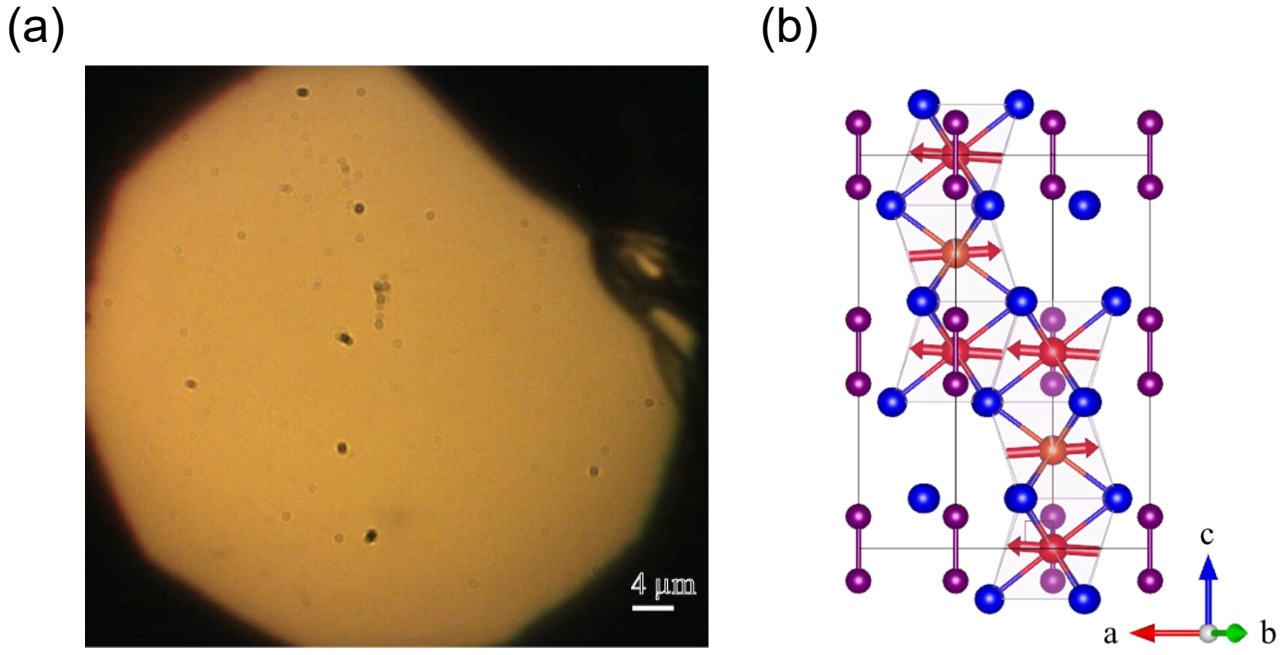

Figure 5.1: (a) Optical image showing the surface of a bulk flake of MST inside a cryostat. (b) Crystal structure of $Mn_3Si_2Te_6$ showing the spin orientation of the Mn1 and Mn2 sites. The crystal structure was constructed through the VESTA software.

intercalated layered structure with trigonal symmetry and two magnetically intertwined sublattices (see **Figure 5.1 (b)**). The two sublattices couple antiferromagnetically with each other forming three competing exchange interactions that order ferrimagnetically at 74 K [128–130]. The first sublattice contains $MnTe_6$ octahedra that share edges within the *ab*-plane (Mn1 site). The second fills one-third of the Mn atoms linking the layers together by filling the octahedral holes (Mn2 site) within the vdW gap. Most interestingly, $Mn_3Si_2Te_6$ possesses an atypical colossal magnetoresistance (CMR) effect demonstrated to only arise when a magnetic field of ≥ 4 T is applied along its *c*-axis [131,132]. This behavior has been accredited to an exotic behavior known as chiral orbital currents [133]. These orbital currents precess along the $MnTe_6$ octahedral edges and when a strong enough magnetic field is applied along its *c*-axis, the orbital currents precess along the same direction giving way to the CMR effect in $Mn_3Si_2Te_6$.

To explore the ultrafast light-driven dynamics of $Mn_3Si_2Te_6$, bulk flakes of single crystal $Mn_3Si_2Te_6$ (see **Figure 5.1 (a)**) were mechanically exfoliated and transferred into an optical cryostat inside a glovebox with an argon atmosphere to prevent the formation of TeO_2 complexes [134]. The laser energies chosen for the pump and probe were 1.55 eV (800 nm), with a pulse width of 60 fs. The photon energy is above the estimated bandgap (0.45 eV) of $Mn_3Si_2Te_6$ [129]. The beam was split into pump and probe arms (using a 50/50 beam splitter) that were focused onto the sample at near-normal incidence using a 20X apochromatic objective, with a spot size of ~ 7 μm, and linearly cross-polarized to suppress pump scattering from the obtained signal. The laser fluence for the probe was fixed at $0.125\ \mathrm{mJ \cdot cm^{-2}}$ throughout the experiment while the pump fluence was set to $2.5\ \mathrm{mJ \cdot cm^{-2}}$ to avoid sample degradation. Additional experimental details are laid out in section 2.3 of this dissertation.

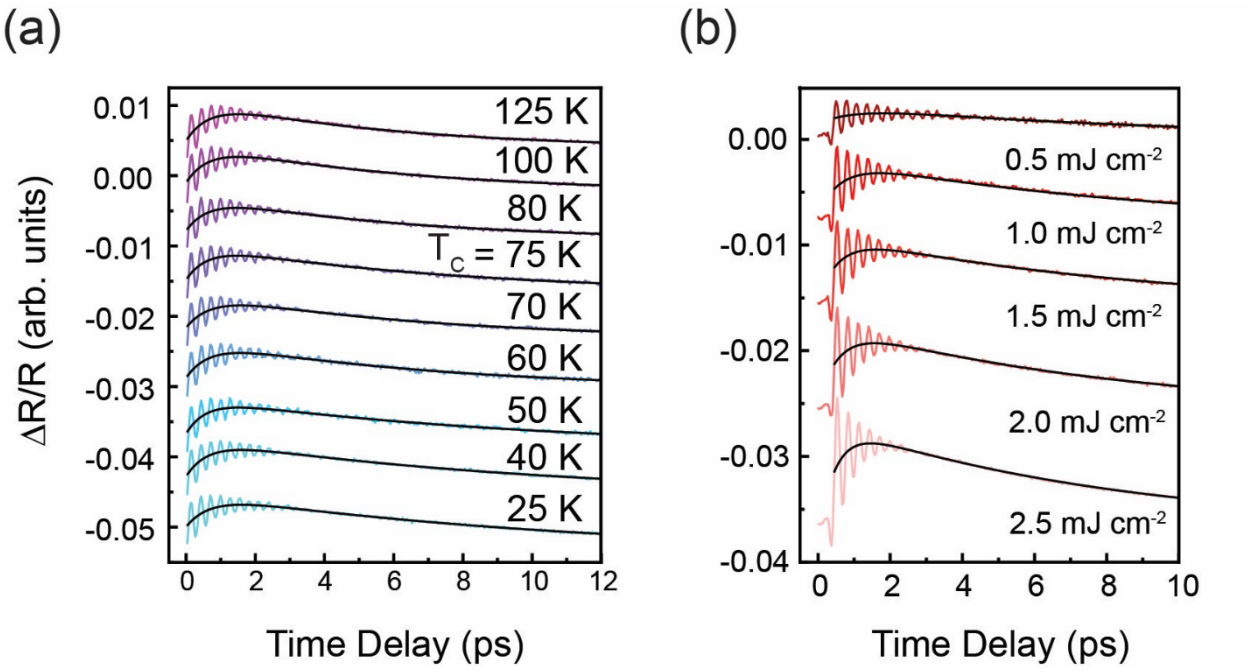

Figure 5.2: (a) shows the crystal structure of MST with its magnetic moments pointing along the *ab* plane. (b) $\Delta R/R$ from 25 - 125 K at a pump fluence of 1.5 mJ cm^{-2} and (c) the $\Delta R/R$ traces with varying pump fluence measured at 300 K, showing increases in both the oscillation amplitude and the electronic background. The black lines in both (b) and (c) are fits to the data using Eq. 5.1.1.

Section 5.1 - Incoherent Dynamics of MST

The differential reflectivity $\left(\frac{\Delta R}{R}\right)$ of $Mn_3Si_2Te_6$ as a function of temperature is shown in **Fig. 5.2 (a)**. From this figure, two components can be clearly observed, one being a broad time-dependent incoherent background superimposed with pronounced coherent oscillations. The former is due to the nonequilibrium dynamics associated with hot electrons driven by the above bandgap photoexcitation. These dynamics can be fit using a biexponential function [135–137],

$$\frac{\Delta R(t)}{R} = Ae^{-\frac{t}{\tau_1}} + Be^{-\frac{t}{\tau_2}} \qquad 5.1.1$$

where the amplitudes (A and B) and time constants (τ_1 and τ_2) are treated as free parameters. The black curves in **Fig. 5.2 (a, b)** show the best fits to the temperature- and fluence-dependent data using a trust-region reflective least squares algorithm, revealing a relatively fast rise followed by

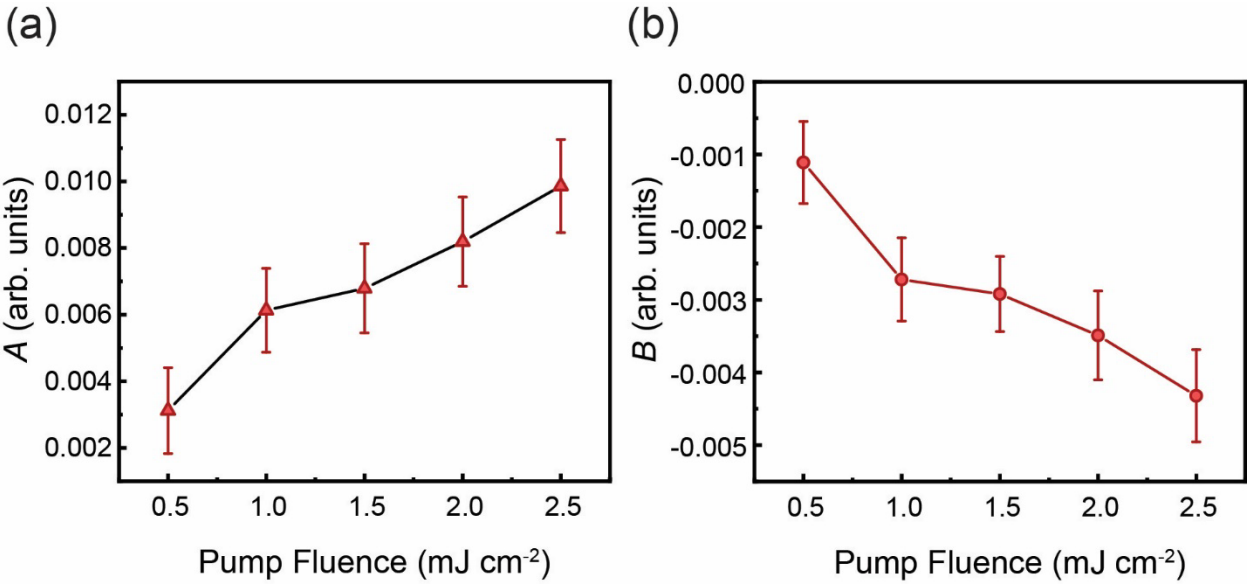

Figure 5.3: The (a) A and (b) B amplitudes obtained from the biexponential model (Eq. 6.1.1). We observe a linear increase (decrease) in the amplitude of A (B) as the pump fluence increases.

a slow relaxation for the former, consistent across the entire temperature range. Fitting the pump fluence-dependent data with the biexponential fit reaffirms the observed increase in the magnitude of A and B as the pump fluence increases (shown in **Fig. 5.3 (a, b)**) consistent with their hot electron origin.

Section 5.2 - Microscopic Four Temperature Model Description

Within the field of ultrafast demagnetization, the observed dynamics in ferromagnetic metals have been well described by a microscopic three-temperature model (M3TM). This phenomenological model was originally adapted from the three-temperature model (3TM) which describes the rate of energy exchange between the electronic, lattice, and spin reservoirs through three coupled differential equations [118]. Koopmans et al pushed this model further by incorporating a microscopic description of the spin-flip probability (a_{sf}) for an electron-phonon momentum scattering event [48]. Typically, this M3TM model is best used to describe the demagnetization dynamics within ferromagnetic metallic materials, however, it is possible to

extend this phenomenological description to semiconducting systems due to the transient quasi-metallic state driven by the ultrafast photoexcitation of carriers [82,138]. Through a collaboration with a theoretical group from the University of Edinburgh, a similar methodology was implemented in the incoherent dynamics presented in this chapter.

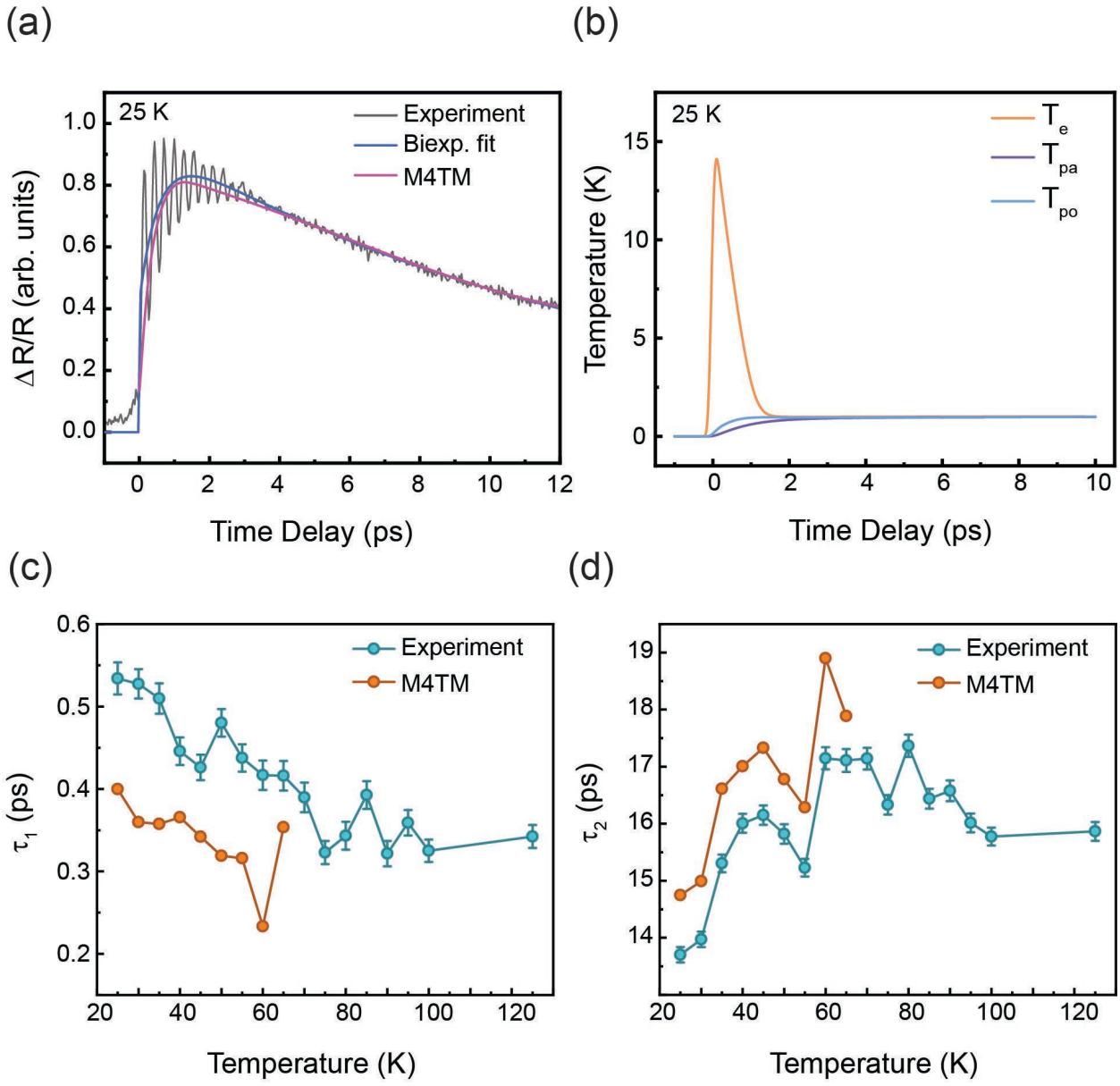

Figure 5.4: (a) The experimental $\Delta R/R$ (blue) measured at 25 K with the biexponential fit from Eq. 1 (green) and the M4TM simulation (black). (b) The electronic (T_e), acoustic (T_{pa}), and optical phonon (T_{po}) temperatures extracted from the M4TM at 25 K. (c) The temperature dependence of τ_1 (rise time) and (d) τ_2 (decay time) along with the time constants extracted from the M4TM simulation.

These theoretical calculations adopt the M3TM but splits the lattice into optical and acoustic phonon subsystems. This splitting is an approximation due to the acoustic phonons also undergoing electron-phonon scattering, but at a reduced rate. The adapted M3TM, now referred to as the microscopic four temperature model (M4TM) [138], describes the coupling between the hot electrons to the lattice through the optical and acoustic phonon subsystems, in addition to spins. This model defines the systems by the electronic, optical phonon, and acoustic phonon temperature (T_e, T_{po}, and T_{pa}, respectively) and their heat capacities (C_e, C_{po}, andC_{pa}, respectively). The dynamics between the electron and two phonon subsystems are described by the coupled equations:

$$C_e \frac{dT_e}{dt} = g_{e-po}\left(T_{po} - T_e\right) + P(t) + \dot{Q}_{e-s}, \quad 5.2.1$$

$$C_{po} \frac{dT_{po}}{dt} = g_{e-po}\left(T_{po} - T_e\right) + g_{po-pa}(T_{pa} - T_{po}), \quad 5.2.2$$

$$C_{pa} \frac{dT_{pa}}{dt} = g_{po-pa}(T_{pa} - T_{po}), \quad 5.2.3$$

where $P(t)$ is the absorbed laser pulse energy that excites the electronic system, $g_{e\text{-}po}$ is the coupling between electron and optical phonons, and $g_{po\text{-}pa}$ is the optical-acoustic phonon coupling constant. Here the electron system is energetically coupled to the (i) optical phonons with temperature T_{po} and (ii) the spin system via the energy flow, $\dot{Q}_{e-s} = \frac{Jm\dot{m}}{V_{at}}$ where J is defined by $J = 3\frac{S^2}{S(S+1)}k_B T_c$, m is the magnetization, S is the spin, and V_{at} is the atomic volume calculated by the number of atoms in a unit cell [138]. The optical phonons are also coupled to the acoustic phonons with temperature T_{pa} and heat capacity C_{pa}. Applying the M4TM to describe the incoherent dynamics allows us to extract the temperature dependences of key parameters in the system such as; g_{e-po}, the Sommerfield coefficient (γ_e), C_e, C_{po}, C_{pa}, and the a_{sf} (see **Table 5.1**).

Table 5.1: Parameters obtained from the M4TM used to simulate the experimental $\Delta R/R$. g_{e-po} is the electron-phonon coupling constant, γ_e is the Sommerfield coefficient, C_{po} is the optical phonon heat capacity, C_{pa} is the acoustic phonon heat capacity and a_{sf} is the spin-flip probability.

T (K)	$g_{e\text{-}po}$ (W m^{-3} K)	γ_e (J m^{-3} K^{-2})	C_{po} (J m^{-3} K)	a_{sf}
25	1.75×10^{18}	4.4×10^{3}	3.2×10^{7}	0.180
30	1.85×10^{18}	4.0×10^{3}	4.0×10^{7}	0.150
35	1.85×10^{18}	4.0×10^{3}	5.3×10^{7}	0.125
40	1.95×10^{18}	4.4×10^{3}	7.8×10^{7}	0.115

The latter, enabled by strong spin-orbit coupling leading to the majority and minority spin carriers being admixtures of pure spin states [139], has proven to be a major driver of ultrafast demagnetization in prototypical vdW magnets [82].

As shown in **Fig. 5.4 (a)**, the M4TM simulation of the incoherent dynamics at 25 K demonstrate good qualitative agreement with the experimental data. It is found that the M4TM provides a consistent model of the incoherent dynamics driven by the energy flow between the electrons, phonons, and spin subsystems up to 75 K. **Figure 5.4 (b)** shows the simulated T_e, T_{po}, and T_{pa} profiles for MST. The g_{e-po} is estimated to be approximately $\sim 1.85 \times 10^{18}$ W m^{-3} K, showing minimal variation with temperature, and is significantly larger than the recently reported electron-phonon coupling of a similar vdW magnet $Cr_2Ge_2Te_6$ ($\sim 15 \times 10^{18}$ W m^{-3} K) [138]. More importantly, a_{sf} steadily increases below T_C, and its relatively large value, in line with CrI_3 [82], supports the presence of strong spin-phonon coupling in $Mn_3Si_2Te_6$.

Additional insight can be gleaned from the time constants extracted from the biexponential fits using Eq. 5.1.1. τ_1 has values on the order of ~ 350 fs that increases in a linear fashion below T_C (blue dots in **Fig. 5.4 (c)**). Due to the above gap photoexcitation, the carrier dynamics on this time scale are most likely associated with electron-electron scattering, which is suppressed at lower temperatures. Other magnetic semiconductors have shown similar temperature variations in the sub-picosecond carrier dynamics [50,135,136,140]. τ_2, associated with electron-phonon scattering

processes, increases slightly from 125 K to 60 K (green dots in **Fig. 5.4 (d)**). This trend reverses below 60 K, where the electron-phonon scattering becomes faster, reaching a value of 13 ps at 25 K. This is likely due to the enhanced spin-phonon coupling below T_C and the activation of additional phonon-mediated spin-flip scattering channels, an assertion supported by the mirrored temperature dependence of a_{sf}. The time constants extracted from the M4TM are presented in **Fig. 5.4 (c, d)**. These values show a good qualitative agreement with the experimental values, differentiated only by a fixed offset. We note that the data above 70 K are not reproduced well by the M4TM (see **Figure 5.5**) given that above the critical temperature, the lack of long-range magnetic order means that the spin system is no longer a valid temperature bath. That is, the system becomes magnetically disordered which makes it difficult to describe the behavior of τ_1 and τ_2 via the connection between the different reservoirs (spin, lattice, electron) mutually interacting when one of them (e.g., spin bath) is no longer present. In a more limited two-temperature model, just including the charge and lattice degrees of freedom, we would expect to recover the high temperature data. However, this was not the case as we were unable to sound describe the behavior

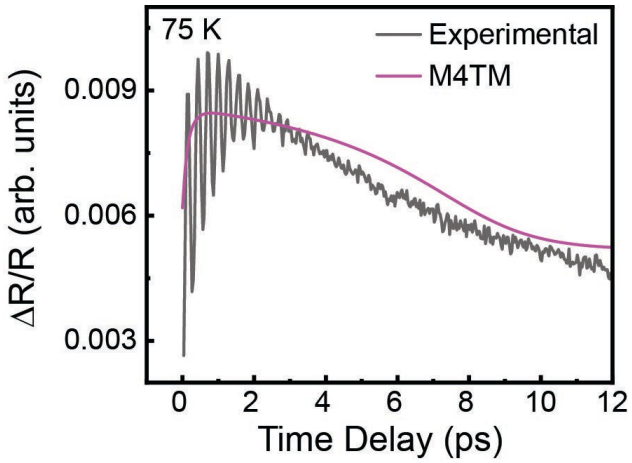

Figure 5.5: The experimental $\frac{\Delta R}{R}$ with the M4TM simulation measured at 75 K. The simulation here shows the irreproducibility of the experimental data due to a lack of long-range magnetic ordering.

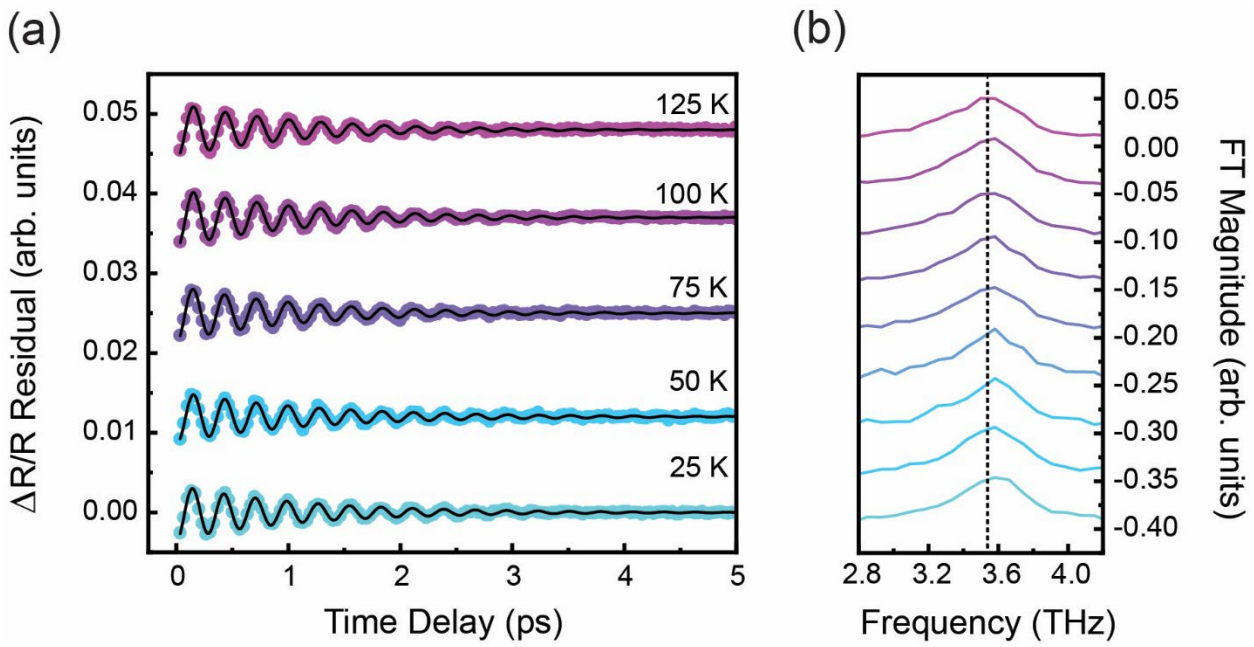

Figure 5.6: (a) The experimental $\Delta R/R_{res}$ at various temperatures above and below T_c and (b) the magnitude of their respective FTs. The black lines in (a) are fits calculated from the damped sine function (Eq. 5) and the dotted line in (b) denotes the high temperature frequency of the phonon mode (3.52 THz).

above T_C with such a simple model since the spin-driven pathways in phonon-mediated carrier relaxation is one of the main ingredients for such behavior.

Section 5.3 - Coherent Dynamics of MST

Our focus now shifts towards the coherent oscillatory dynamics presented in **Fig. 5.6 (a)** where the incoherent dynamics are subtracted (via the biexponential fitting) leaving the residual differential reflectivity $\left(\frac{\Delta R_{res}}{R}\right)$ as function of temperature. The strong coherent oscillations have a decay time of ~ 3 ps and oscillatory frequency of ~3.52 THz. The Fourier transform (FT) of the time-domain data for various temperatures is shown in **Fig. 5.6 (b)**. From recent spontaneous Raman scattering measurements [134], the extracted frequency is identified to be a phonon of E_g symmetry, driven via an impulsive stimulated Raman scattering (ISRS) process by the ultrafast pump [141,142]. There is also some potential for this to be a tellurium A_{1g} phonon [143], though

in this case, the temperature dependencies are rather unexpected as we will see later. For context, in the case of spontaneous Raman scattering, an incident photon excites an electron from its ground state into a higher energy virtual state. The electron then relaxes back to its ground state releasing energy in the form of a scattered photon. The energy difference between the incident and scattered photons then becomes the Raman shift measured in Raman spectroscopy. ISRS on the other hand, requires an impulsively driven force to initiate coherent lattice motion [144]. The main requirement for an ISRS excitation is for Raman active modes to be present within the material system. In this case, coherent phonons can be driven so long as the polarization of the pump and probe satisfy Raman selection rules and the bandwidth of the optical pulse is larger than the phonon energy (i.e., the pulse width is much smaller than the period of the lattice oscillation) [145].

Back to **Figure 5.6 (a)**, as the temperature decreases, a subtle, yet significant, stiffening of the phonon mode can be observed, evidenced by the shift of the FT peak to higher frequencies in **Fig. 5.6 (b)**. To better capture the temperature-dependent variation of the phonon frequency, we fit a damped sine function to the $\frac{\Delta R_{res}}{R}$ [141],

$$\frac{\Delta R_{\mathrm{res}}}{R} = A_{DO} e^{-\frac{t}{\tau_{DO}}} \sin\left(\omega_{DO} t + \phi_{DO}\right) \qquad 5.3.1$$

where A_{DO} is the amplitude, τ_{DO} is the time constant, ω_{DO} is the frequency, and ϕ_{DO} is the phase shift of the damped oscillator. The black lines in **Fig. 5.6 (a)** are the fits using Eq. 5.3.1. The temperature dependence of the ω_{DO} is plotted in **Fig. 5.7**. The frequency of the phonon mode is

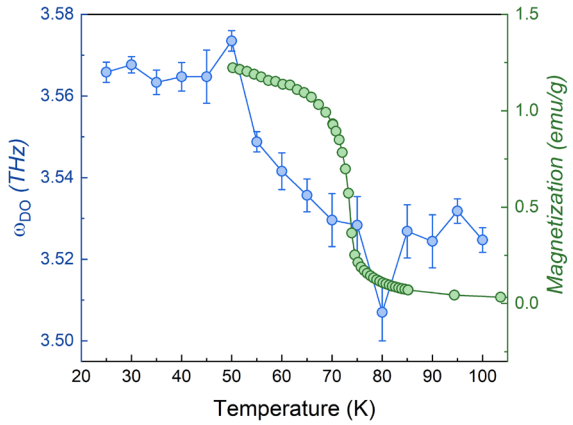

Figure 5.7: The damped oscillation frequency (black dots, left y-axis) obtained from Eq. 5.3.1, plotted as a function of temperature and the temperature dependent magnetization (blue dots, right y-axis) measured with an applied field of 0.5 T.

relatively constant (~ 3.53 THz) above the T_C but increases rapidly from 75 K down to 50 K, before stabilizing to ~ 3.57 THz at lower temperatures. This temperature dependence is distinct from what would be expected under the assumption of thermally driven lattice contraction [146]. Indeed, the frequency vs. temperature qualitatively resembles the magnetization vs. temperature, as we will discuss in the next section.

Section 5.4 - Discussion

It has been shown in the recent past that magnetic exchange interactions can be modulated by distortions of the structural lattice in vdW magnets [82], leading to spin-coupled coherent phonon dynamics. We propose that the onset of ferrimagnetic order leads to a dynamic exchange magnetostriction [147] driven by spins that then contract the lattice, hence an opposite effect to that of the above-mentioned phenomena. An overlay of the temperature-dependent magnetization (green curve in **Fig. 5.7**), obtained via VSM measurements, reveals a relatively close qualitative agreement with the experimental $\omega_{DO}(T)$ (given the laser-induced heating of the lattice). This indicates that the temperature dependence of the phonon frequency roughly follows the onset of

ferrimagnetic order in the crystal, underscoring its potential spin-driven origin. Indeed, similar spin-order dependent shifts of *thermal* phonon frequencies have been observed in other materials [148–150] through spontaneous Raman scattering. However, a spin-order dependent shift of the *coherent* phonon frequency has, to the best of our knowledge, never been observed in any vdW magnet. We note that, like CrI_3 [82], the coherent phonon mode in $Mn_3Si_2Te_6$ should also demonstrate a spin-coupled character, which can be verified using techniques such as time-resolved MOKE spectroscopy in future studies.

Section 5.5 - Summary

To conclude, ultrafast optical spectroscopy is implemented to study the electronic and coherent phonon dynamics in the ferrimagnetic crystal $Mn_3Si_2Te_6$. By using the M4TM, we modeled the electronic dynamics due to the presence of the strong spin-lattice coupling below 70 K. Most importantly, we identify a coherent phonon mode that couples strongly to the ferrimagnetic order. This phonon's frequency shifts across T_C mirroring the temperature-dependent magnetization and possible originates from an exchange mediated interaction between the coherent phonon and spins. Further studies focusing on the spin dynamics could reveal greater insight into the coupling between the phonon and spin subsystems within $Mn_3Si_2Te_6$ and could provide an exciting route to dynamically drive its intriguing magneto-resistive properties [117].

Chapter VI - Enhanced magnetization in proton irradiated $Mn_3Si_2Te_6$ van der Waals crystals

Ion irradiation has become an increasingly popular method to induce or alter the magnetic properties of functional materials [151]. Specifically, proton irradiation has been found to induce a magnetic response [152–156] in otherwise non-magnetic materials. Other materials with a link between structure and magnetic ordering have been shown to be strongly affected by proton irradiation, experiencing and alteration in their magnetic properties [151,157–160]. Therefore, we chose to explore the effects of proton irradiation on vdW magnets, due to the intrinsically strong coupling between their lattice and spin degrees of freedom [23]. From the previous chapter, through ultrafast optical excitation, we uncovered strong spin-phonon coupling in the quasi-2D vdW magnet $Mn_3Si_2Te_6$. This chapter takes advantage of this coupling and explores the effects of proton irradiation on the magnetic properties of $Mn_3Si_2Te_6$ through static magnetometry, EPR, and Raman spectroscopy.

Proton irradiation of various $Mn_3Si_2Te_6$ samples was performed through a collaboration with the Department of Nuclear Engineering at Texas A&M University. With their 1.7 MV Tandetron accelerator, irradiation with protons at an energy of 2 MeV (this energy is low enough to not cause unwanted damage to the samples) was possible, while varying the proton fluence from 1×10^{15} H^+ cm^{-2}, 5×10^{15} H^+ cm^{-2}, 1×10^{16} H^+ cm^{-2}, and 1×10^{18} H^+ cm^{-2} on different crystals of $Mn_3Si_2Te_6$. The proton beam spot size was $6\ mm \times 6\ mm$ and was rastered over an area of $1.2\ cm \times 1.2\ cm$ to ensure uniformity of irradiation. **Figure 6.1** shows the penetration depth of the hydrogen ions (H^+) to be approximately 30 μm.

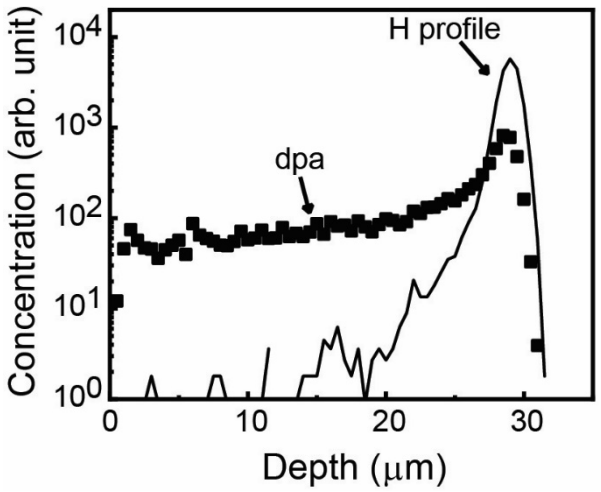

Figure 6.1: The depth profile for the proton irradiation applied to each of the samples demonstrating the displacement per atom (dpa) with an approximate penetration depth of 30 μm.

Section 6.1 - Magnetic characterization of Proton Irradiated MST

To begin, we investigated the $M(H)$ behavior of pristine $Mn_3Si_2Te_6$ and compared it to the changes induced by proton irradiation at various fluences. The isothermal magnetization (50 K) was measured within the ferrimagnetic phase with the magnetic field applied along the ab- and c-planes of the sample, shown in **Fig. 6.2 (a, b)**. The $M(H)$ measured along $H//ab$ shows a square-shaped $M - H$ loop for pristine $Mn_3Si_2Te_6$ at all the applied fluences with negligible coercive field, as expected [128,161]. Remarkably, the magnetization along the $H//ab$ at 50 K shows an enhancement by $\sim 53\%$ after the $Mn_3Si_2Te_6$ crystal is exposed to a proton fluence of 5×10^{15} H^+ cm^{-2}, relative to the pristine case. The variation in the magnetization measured along $H//c$, depicted in **Fig. 6.2 (b)**, demonstrates a similar trend after exposure to the various proton fluences with a small ferromagnetic contribution known to be present along the c-axis. The magnetization along the $H//c$ at 50 K also sees an increase by 37% at that same fluence. When comparing **Fig. 6.2 (a)** and **(b)**, it is apparent that the strong magnetic anisotropy in $Mn_3Si_2Te_6$ is retained even after proton irradiation. The magnetization measured along the ab plane is higher

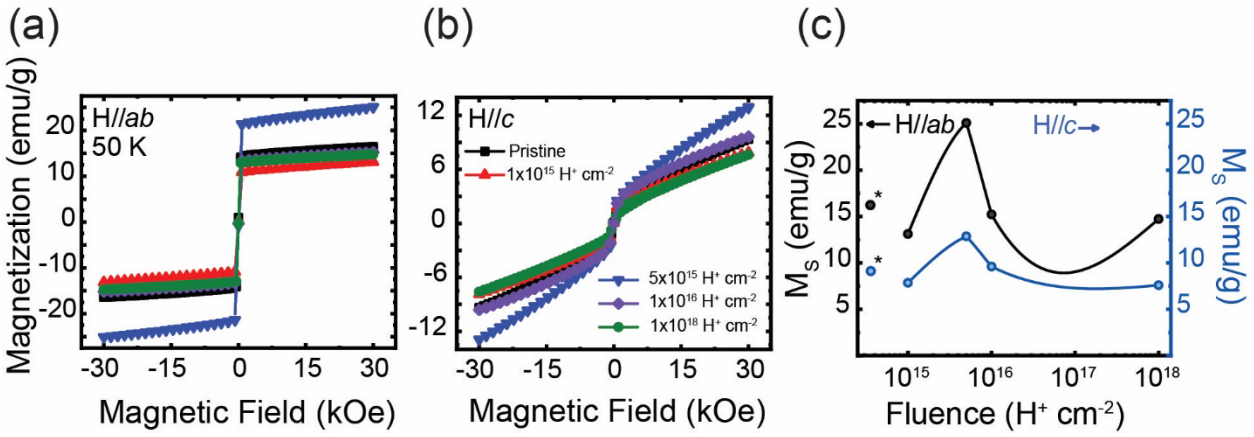

Figure 6.2: Isothermal magnetization measured in the *ab*-plane (a) and in the *c*-plane (b) within the ferrimagnetic phase. The fluence dependent magnetization is shown; the left y-axis represents the magnetization collected in the *ab*-plane at $30\ kOe$, and the right y-axis shows the magnetization collected in the *c*-plane at $30\ kOe$ (c).

than the c-axis magnetization due to the spins in $Mn_3Si_2Te_6$ primarily aligning along the *ab* plane [128,161].

The variation in the magnetization as a function of proton fluence is captured in **Figure 6.2 (c)**, for both c- and ab-plane magnetization. The measurements were taken at 50 K and 30 kOe for all the samples. It is clear from this figure that the proton fluence of $5 \times 10^{15}\ H^+\ cm^{-2}$ increased the magnetization by $\sim 53\%$ relative to its pristine value, while the magnetization decreased for the $1 \times 10^{15}\ H^+\ cm^{-2}$, $1 \times 10^{16}\ H^+\ cm^{-2}$, and $1 \times 10^{18}\ H^+\ cm^{-2}$ proton fluences.

Next, the $\chi(T)$ characteristics as a function proton irradiation were studied along both crystallographic directions (**Figure 6.3 (a, b)**). The $\chi(T)$ presented here varies differently as a function of proton fluence, in contrast to the magnetization measured through the $M(H)$ loops. However, the magnetic parameters extractable through the CW law and the temperature derivative of $\chi(T)$ $\left(\frac{d\chi}{dT}\right)$ are of greater interest. First, to study the variation in the T_C as a function of proton fluence we plot the $\frac{d\chi}{dT}$ presented in **Figure 6.3 (c)**. From this information, we can determine that

no significant change in the T_C occurs after proton irradiation. However, a notable shift in the T_C is observed after a proton fluence of 1×10^{18} H^+ cm^{-2} with a slight decrease of 1.4 K (see **Table 6.1**). For pristine $Mn_3Si_2Te_6$, the T_C is found to be $74\,K$, in good agreement with prior reports [128,161]. Second, the $\chi^{-1}(T)$ plots are fitted with the CW law (Eq. 2.1.2) within the temperature range of $175 - 400\,K$ to extract C, Θ_{CW}, μ_{eff}, and J (shown in **Table 6.1**). The

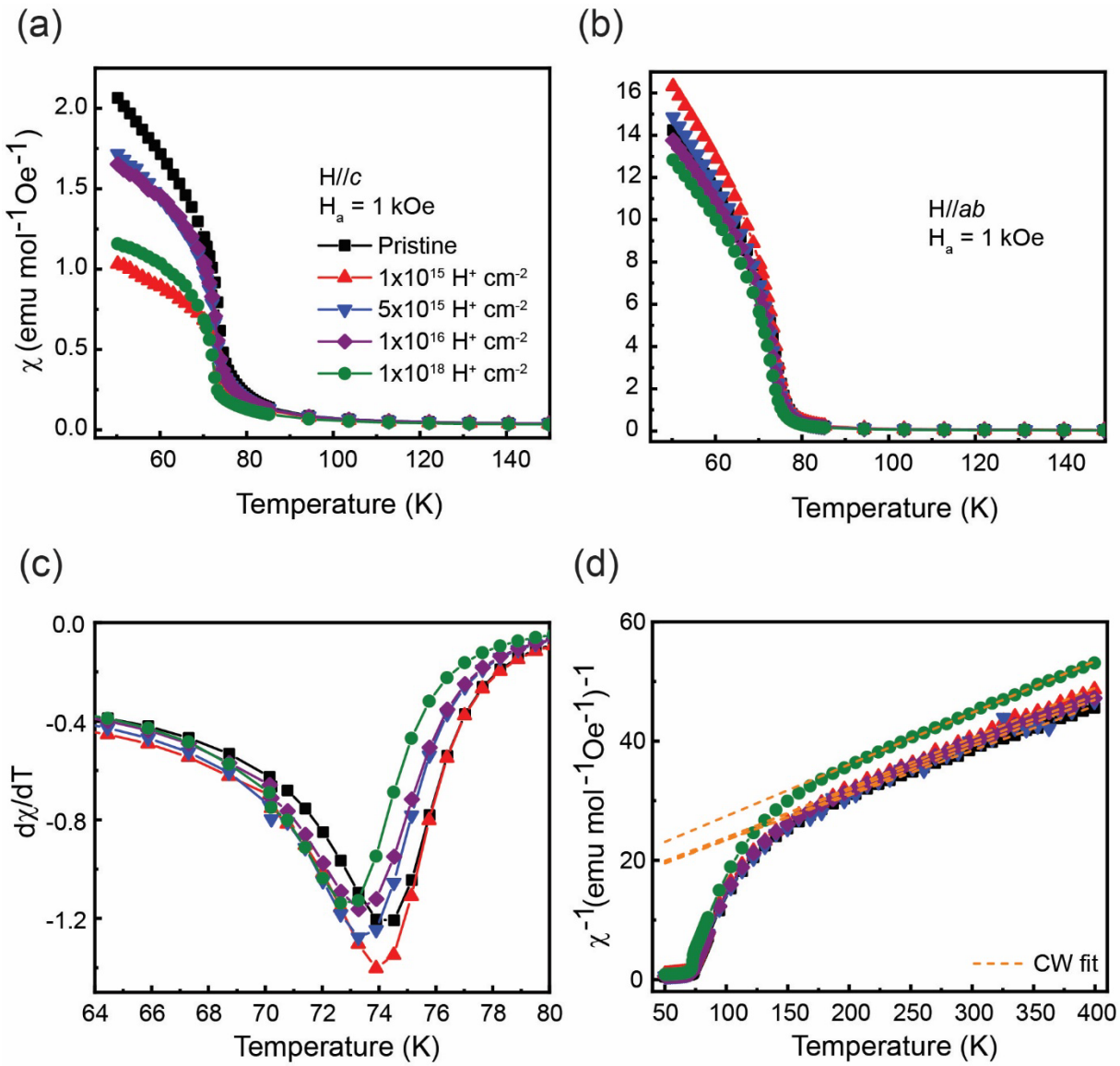

Figure 6.3: The temperature dependent susceptibility [χ(T)] Field-Cooled (FC) curves are shown in (a) and (b), measured with an applied field of 1 kOe along the *ab*- and *c*-planes. The derivative of χ(T) is shown in (c) for pristine and all the fluence applied to MST. The inverse χ(T) is also shown (d) with the CW fit (orange dotted lines) performed between $175 - 400\,K$.

resulting Θ_{CW} was found to be negative, pointing towards antiferromagnetic correlations [41,161] and is almost three times greater than T_C for pristine and all the proton fluences. Furthermore the deviations from T_C point towards short-range spin correlations that exist in $Mn_3Si_2Te_6$ [128]. The μ_{eff} is consistent with the presence of the high-spin state Mn^{2+} ($S = 5/2$) in an octahedral field, which is close to the expected value of $\mu_{cal} = 5.92\ \mu_B$ (also supported by EPR measurements in the following section) [128].

Section 6.2 - EPR spectra of Proton Irradiated MST

Greater insight can be attained on the origin of the enhancement in the magnetization induced by a proton fluence of 5×10^{15} H^+ cm^{-2} by investigating the temperature dependent EPR spectra across T_C. **Figure 6.4 (a)** shows the EPR spectra for pristine and all the irradiated samples measured within the ferrimagnetic phase (50 K), which includes the experimental data (dotted curves) and the computer-generated fits (solid-colored curves) using the Lorentzian and Dysonian

Table 6.1: Transition temperature (T_C) and parameters extracted from the CW fit to the $\chi^{-1}(T)$ such as Curie constant (C), CW temperature (Θ_{CW}), the effective moment (μ_{eff}), and nearest-neighbor exchange interaction (J) for pristine and all irradiated MST samples.

Parameters	T_C (K)	C (emu K mol^{-1})	Θ_{CW} (K)	μ_{eff} (μ_B)	J (meV)
Pristine	73.9	13.34	-212.4	5.16	-1
1x10^{15} H$^+$ cm^{-2}	73.2	11.92	-186.1	4.88	-0.916
5x10^{15} H$^+$ cm^{-2}	72.6	12.74	-198.1	5.04	-0.975
1x10^{16} H$^+$ cm^{-2}	72.6	12.6	-200.6	5.01	-0.987
1x10^{18} H$^+$ cm^{-2}	72	11.54	-216.3	4.8	-1.1

line shapes. From the fits, two overlapped signals were identified. **Figure 6.4 (b)** shows the two signals fitted with their respective line shapes for pristine $Mn_3Si_2Te_6$ at 50 K. A similar process

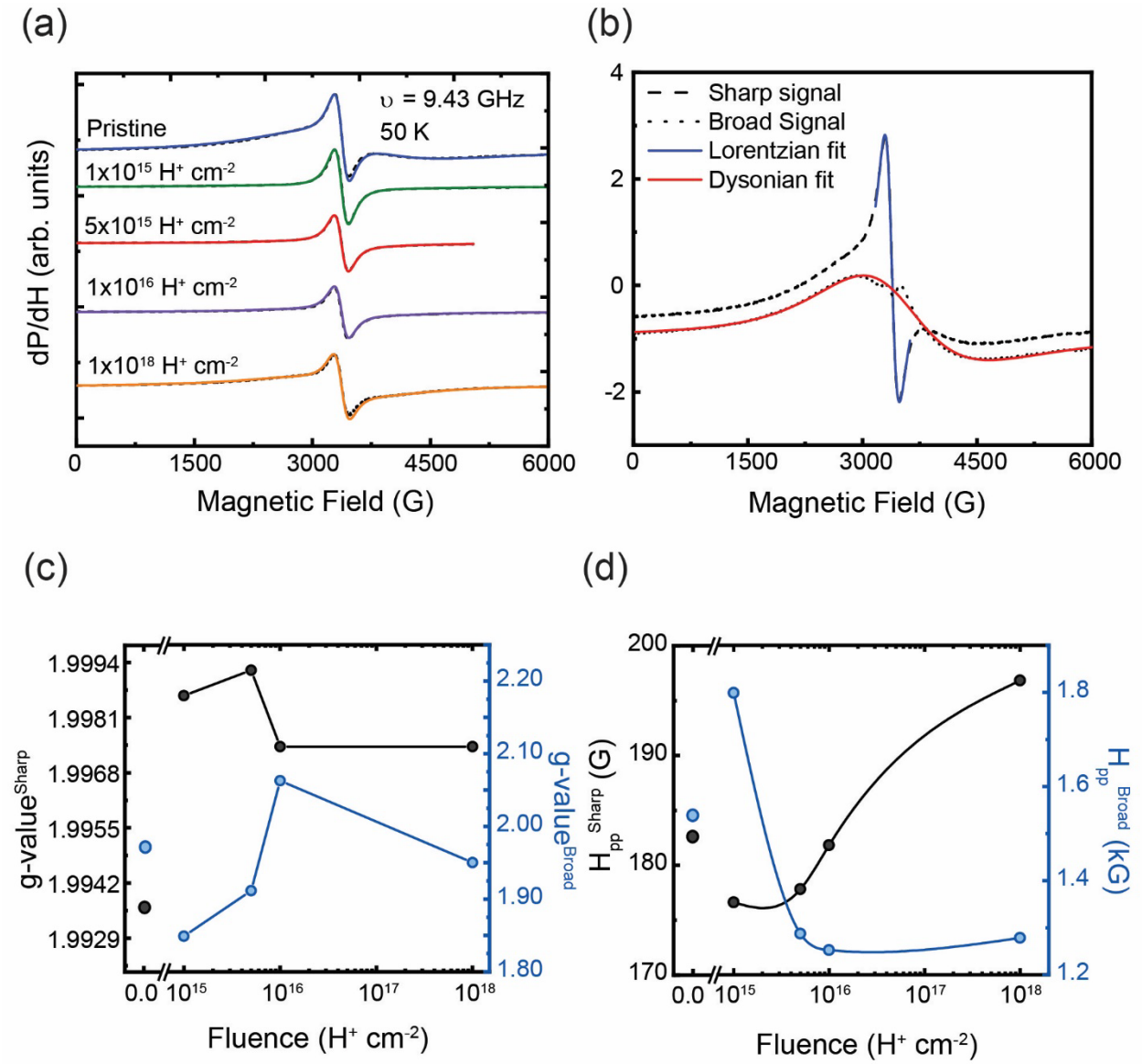

Figure 6.4: X-band EPR spectra measured within the ferrimagnetic phase (50 *K*) of pristine and the irradiated MST samples (a). The colored continuous curves are the measured spectra while the dotted lines are computer-generated simulations for each EPR spectra using two Dysonian line-shapes. (b) Sharp signal and the deconvoluted broad signal with Dysonian fits. The g-value (b) and the linewidths (c) as a function of proton fluence are also shown for the sharp and broad signals.

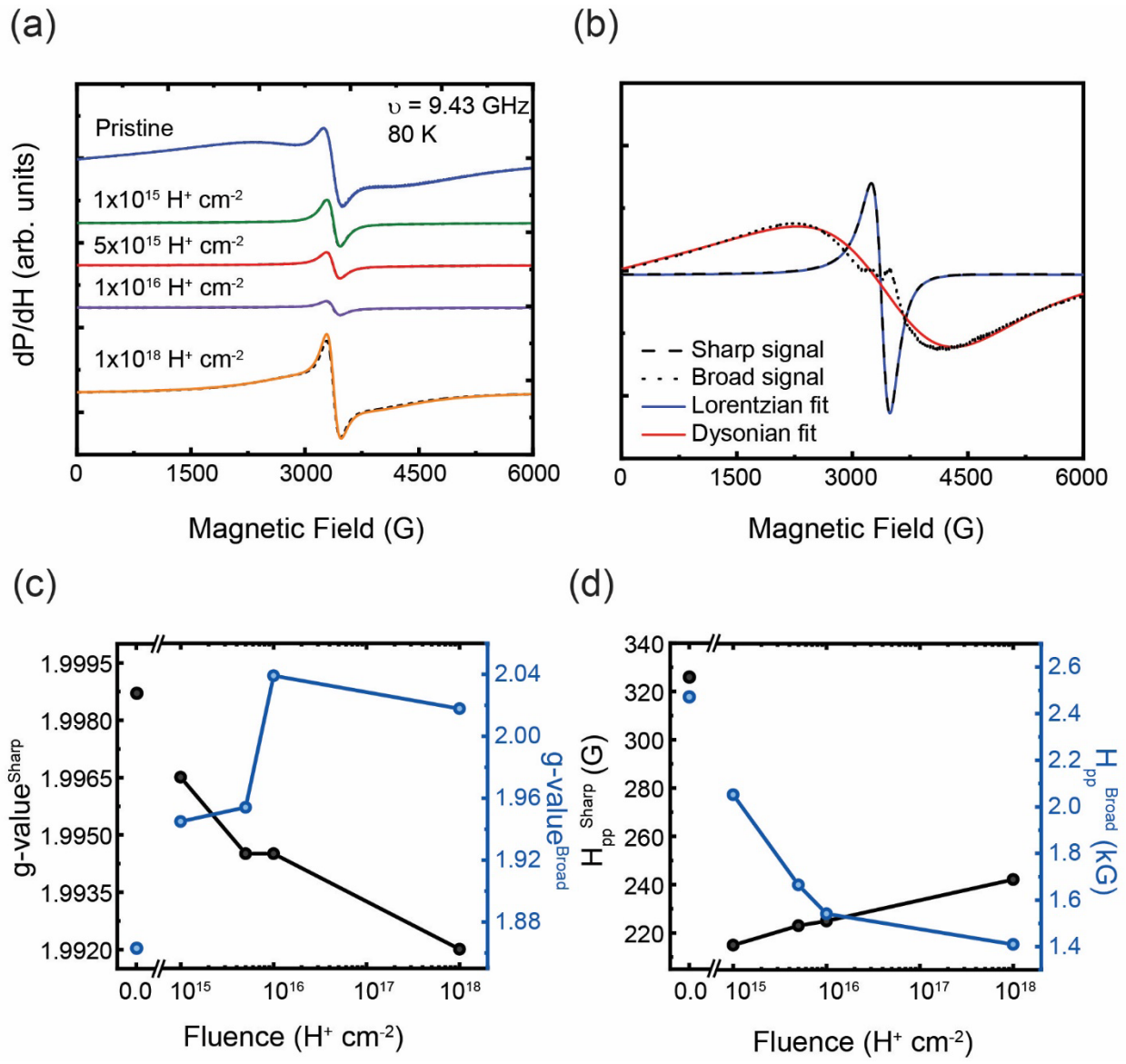

Figure 6.5: X-band EPR spectra measured slight above the ferrimagnetic phase (80 K) of pristine and the irradiated MST samples (a). Like Figure 6.4 (a), the colored continuous curves are the measured spectra while the dotted lines are computer-generated fits to the each EPR spectra using a Lorentzian and Dysonian line-shapes. (b) The sharp signal observed at 80 K with the deconvoluted broad signal fitted with a Dysonian line-shape. The g-value (b) and the linewidths (c) as a function of proton fluence are also shown for the sharp and broad signals.

was done for all the irradiated samples. The EPR spectral parameters, such as Sharp signal linewidth (H_{pp}^{Sharp}), Broad signal linewidth (H_{pp}^{Broad}), Sharp signal g-value (g-value$^{\text{Sharp}}$), and Broad signal g-value (g-value$^{\text{Broad}}$) were extracted from the fits as a function of fluence (shown in

Fig. 6.4 (c, d)). Upon closer examination, a clear variation in the EPR spectral parameters is seen at a fluence of around 5×10^{15} H^+ cm^{-2}. The reduction in the linewidth for both signals is attributed to the strong exchange narrowing effect [162] at that fluence, while the variation in the g-value tops out due to locally enhanced magnetic corrections [163]. A similar analysis was performed for the EPR spectra for pristine and all the irradiated samples slightly above the ferrimagnetic phase (80 K) as shown **Figure 6.5 (a – d)**. Above T_C, we still observe only two signals with no additional signals related to magnetic defects after proton irradiation.

Now, we will focus on identifying the two EPR signals observed above and below T_C. Prior reports [128,161] demonstrate the presence of two Mn sites within $Mn_3Si_2Te_6$, namely, Mn1 (in the ab-plane) and Mn2 (in the c-plane). Additionally, the multiplicity of the Mn1 site is twice that of Mn2 with a significant separation between the two sites. With the Mn1 site being two times greater in number than the Mn2 site, the magnetic moment of Mn1 is thus expected to be twice as high as Mn2. As stated in the introductory part of Chapter V, the Mn1 site is composed of $MnTe_6$ octahedra while the Mn2 sites links the layers together filling up one-third of the octahedral holes within the vdW gap [128]. In addition, due to the strong exchange interaction (Mn1-Mn1 $\approx$ 4.06 Å) between the spins on the Mn1 site, the EPR signal is expected to be sharper. Hence, it is reasonable to assign the sharper signal ($H_{pp}^{Sharp} \approx 180 - 200$ G) to the observed Mn1 site while the broader signal ($H_{pp}^{Broad} \approx 1.2 - 1.8$ kG) can be assigned to the Mn2 site. Because of their distinct surroundings, the two Mn sites should have different EPR spectral properties. The sharper, more intense signal is associated with a g-value of 1.998. While the broader, less intense signal is associated with a g-value of 1.85. In the addition to the lack of defects, hydrogen ion implantation is absent from the EPR spectra (due to the lack of hyperfine structures) [164], which indicates that the changes brought on by proton irradiation are not caused by the implantation of H^+ ions.

Section 6.3 - Raman spectra of Proton Irradiated MST

Proton irradiation is known to cause structural changes in an irradiated sample. Typically, in proton irradiation experiments, an atom is displaced from the lattice initiating a collision cascade in the system (this is also known as primary knock-on atom [PKA]) [158] thus modifying the magnetic properties of materials with a strong spin-lattice coupling. To gain a better understanding of the observed changes in the magnetization after proton irradiation, we employed Raman spectroscopy to study the lattice vibrations in $Mn_3Si_2Te_6$. The room temperature Raman spectra is shown for pristine and the irradiated $Mn_3Si_2Te_6$ samples in **Fig. 6.6 (a)**. Two peaks are observed for each sample and the extracted Raman peak positions are plotted in **Fig. 6.6 (b)**. We note that the Raman spectra for $Mn_3Si_2Te_6$ had not been previously reported in the literature. However, the Raman spectra for its analog compound $Cr_2Si_2Te_6$ have been reported and will be used as a guide

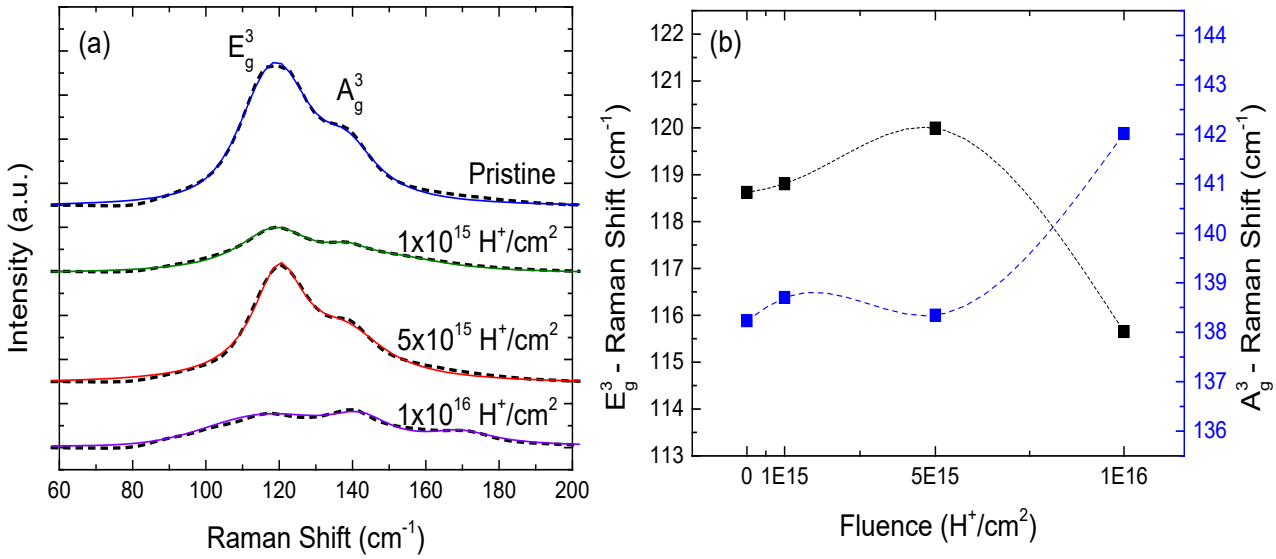

Figure 6.6: Raman spectra collected for pristine and the irradiated MST samples (a) as a function of fluence collected at room temperature. The dotted curves are the measured spectra, and the continuous curves are fits using the Voigt lineshape. The extracted peaks of the observed vibration modes are identified as E_g^3 and A_g^3 phonon Raman modes shown in (b) as a function of proton fluence.

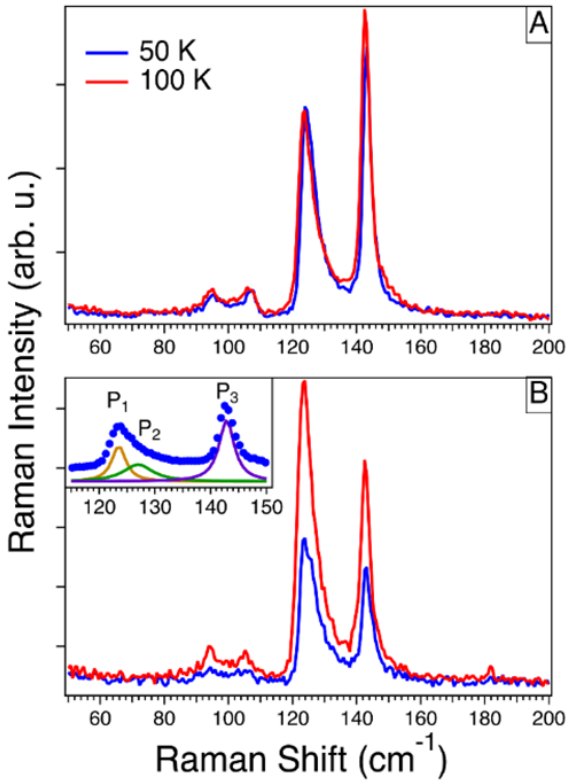

Figure 6.7: Low temperature (50 and 100 K) Raman spectra collected for pristine (A) and a proton fluence of 1x10^{18} H^+ cm^{-2} (B) collected in a cross-polarization scheme. The inset to (B) is an example of fitting the 50 K signal with three Lorentzian line-shapes.

to the observed vibrational modes in $Mn_3Si_2Te_6$ [165,166]. The reported Raman peaks in $Cr_2Si_2Te_6$ arise from in-plane and out-of-plane Te vibrational modes, which are sensitive to magnetic interactions. For pristine $Mn_3Si_2Te_6$, the Raman spectra shows two modes with a peak at 118.4 cm^{-1} and a shoulder at 136.9 cm^{-1}, with close agreement to similar reported modes in $Cr_2Si_2Te_6$ [165,166] related to E_g^3 and A_g^3 modes, respectively. The main differences between the spectra of $Mn_3Si_2Te_6$ and $Cr_2Si_2Te_6$ come from the change in mass and lattice parameters causing phonon positions to differ slightly. From **Figure 6.6 (b)**, the variation in the E_g^3 peak as a function of proton fluence follows a similar trend to the one observed for the magnetization saturation (M_S) shown in **Figure 6.2 (c)**. Hence, it is quite likely that the E_g^3 and A_g^3 modes involve atomic motions of the Te atoms, similar to the modes observed for $Cr_2Si_2Te_6$ which are susceptible to spin

Table 6.2: Extracted parameters, frequency and full-width half-max (FWHM), from the Raman spectra presented in Figure 6.7 (A, B) using Lorentzian lineshapes.

Phonon		Pristine 50 K	Irradiated 50 K	Pristine 100 K	Irradiated 100 K
Frequency (cm^{-1})	P_1	124.02	123.47	123.52	123.38
	P_2	126.62	126.31	126.99	127.02
	P_3	143.27	143.2	142.85	142.77
FWHM (cm^{-1})		2.33	1.95	3.02	3.51
		5.61	5.85	6.44	6.79
		3.09	3.94	3.29	3.88

interactions due to the super-exchange interaction between Cr-Te-Cr atoms [165]. Initial temperature dependent Raman measurements (shown in **Figure 6.7 (A, B)**) reveal changes in the spectral parameters (see **Table 6.2**), indicative of a modification in the spin-lattice coupling after proton irradiation. It is also quite likely that other factors such as changes in the local band structure and surface crystal structure could also be at play.

Section 6.4 - Discussion

The effects on the magnetization of $Mn_3Si_2Te_6$ upon proton irradiation are hypothesized to come from alterations in the magnetic exchange interactions. This material system is known to contain competing antiferromagnetic interactions that lead to frustration [128,129,167]. For example, Mn1-Mn1 interactions have been reported to have a rivalry between direct- and super-exchange interactions that can push the system between an FM and AFM state, determined by the participation of the *p* or *d* orbitals [128]. A recent report on the ultrafast optical excitation of the ligand-to-metal charge transfer resonance of $Cr_2Si_2Te_6$ revealed an enhancement in the nearest-neighbor super-exchange interaction [168]. This enhancement led to a weakening of the AFM direct exchange and strengthened the FM exchange [67]. It is quite possible that the competing

interactions within $Mn_3Si_2Te_6$ could have been affected by the variation in the proton fluence resulting in the observed magnetization change.

A later study on the magnetic properties of pristine and proton irradiated $Mn_3Si_2Te_6$ (at the same fluence presented in this dissertation) provided greater evidence of an enhancement in the FM super-exchange interaction rather than a weakening of the AFM exchange interaction [169]. Through heat capacity and magnetic critical analysis of proton irradiated $Mn_3Si_2Te_6$, two additional sets of data confirmed this scenario in a study performed by Olmos et al [169]. Firstly, extracting the spin correlation length from pristine $Mn_3Si_2Te_6$ and proton irradiated $Mn_3Si_2Te_6$ at the various fluences demonstrated that the proton fluence of 5×10^{15} H^+ cm^{-2} had a greater correlation between the spins when compared to pristine $Mn_3Si_2Te_6$. Secondly, the heat capacity measurements revealed a significant increase in the extracted magnetic entropy of the 5×10^{15} H^+ cm^{-2} proton irradiated $Mn_3Si_2Te_6$ sample to 2.45 J kg^{-1} K^{-1} from 1.60 J kg^{-1} K^{-1} in the pristine case. This report further affirms the conclusion stated in this chapter that the proton fluence of 5×10^{15} H^+ cm^{-2} enhances the FM super-exchange interaction.

Section 6.5 – Summary

The magnetization of $Mn_3Si_2Te_6$ is significantly enhanced by 53% and 37% in the ferrimagnetic phase after exposure to a proton fluence of 5×10^{15} H^+ cm^{-2}, in the ab- and c-planes, respectively. Through EPR spectroscopy we find an absence of defects or implanted H^+, indicating that the enhancement in the magnetization through proton irradiation takes a different route. Raman measurements reveal some of the vibrational modes in this material system for the first time. From these Raman measurements, we demonstrate that the shift in the E_g^3 mode as a function of proton fluence follows the same trend observed for the M_S, indicating a modification

in the strong spin-lattice coupling within $Mn_3Si_2Te_6$. This experimental evidence supports the scenario in which the magnetic super-exchange interactions are modified at this fluence, verified further by heat capacity and critical analysis of the proton irradiated samples. This chapter demonstrates the possibility of using proton irradiation as an effective method to modify the magnetic properties of a vdW crystals by targeting the exchange interactions in these systems.

Chapter VII - Conclusions and Future Directions

The implementation of photoexcitation and proton irradiation onto bulk vdW magnets in this dissertation leads to a greater understanding of what mechanisms are affected after these external stimuli modify their magnetic properties. Firstly, static optical excitation of specific electronic transitions within bulk CrI_3 reveals an enhancement in the saturation magnetization driven by an alteration of the exchange interactions through the creation of a Cr^{2+} photoexcited state. This mechanism was corroborated by studying the photo-induced changes on the local magnetic exchange interactions of CrI_3 and $CrCl_3$ through static EPR spectroscopy. We demonstrate that by photoexciting bulk CrI_3 and $CrCl_3$, a shift in their EPR signals occurred, indicating an optically induced transition from Cr^{3+} to a photoexcited Cr^{2+} state further verified by theoretical calculations. Secondly, ultrafast optical excitation of bulk $Mn_3Si_2Te_6$ revealed an impulsively stimulated coherent phonon that strongly couples to the magnetic ordering. The spin-order-driven frequency shift of the coherent phonon seems to indicate a strong spin-lattice coupling, manifesting as a contraction of the lattice induced by the spin ordering. Thirdly, we showed that subjecting materials such as $Mn_3Si_2Te_6$ (with a strong spin-lattice coupling) to proton irradiation is an effective tool to control its magnetic properties.

After unveiling the effects of these external stimuli on the magnetic properties of bulk vdW materials, this dissertation provides an empirical road map on what mechanism to target when reducing these materials to their true 2D counterparts. More importantly, our work leads to the understanding that these external stimuli schemes can be used as a “knob” to tune exchange interactions in vdW magnets. These findings will become crucial when designing spin-based nanodevices with the 2D counterparts of these vdW magnets, using these forms of stimuli to afford an additional layer of control of device functionality.

There dissertation opens various paths for future exploration. It is important to note that these excitation schemes enhanced the magnetization through control over the exchange interactions. However, the question of how to increase the transition temperature of these vdW magnets remains open. Previously, it has been shown that isostatic pressure is able to target the interactions that affect the transition temperature in $Cr_2Ge_2Te_6$ and $CrBr_3$ [170,171]. Hence, it will be interesting to explore whether other forms of contactless external stimuli, such as nonlinear optical excitation, can become effective tools to target the interactions that directly affect the ordering temperature of vdW magnets. Another interesting direction will be to use ultrafast optical pulses to target specific optical transitions on quasi-2D CrX_3 magnets to understand and characterize the fundamental speed limit of the observed enhancements through the measurement of their magneto-optical dynamics. It will also be quite interesting to target the terahertz (THz) phonons of vdW magnets with intense THz pulses. This method allows us to couple light directly to certain vibrational modes, and dynamically change the magnetic ground state of materials [124]. In a similar fashion, applying this technique to $Mn_3Si_2Te_6$ may allow us to push this material system between an uncompensated AFM phase to a stronger FM phase. Additionally, it would be interesting to identify if an effect related to the colossal magnetoresistance of $Mn_3Si_2Te_6$ [131,132] can be triggered by nonlinear THz spectroscopy. This dissertation thus provides a greater understanding of these external stimuli to tune the exchange interactions in various bulk vdW magnets and provides another step forward in applying these materials for future spin-based nanotechnologies.

References

[1] W. D. C. Jr and D. G. Rethwisch, *Materials Science and Engineering: An Introduction* (Wiley Global Education, 2018).

[2] N. Fang, C. Wu, Y. Zhang, Z. Li, and Z. Zhou, *Perspectives: Light Control of Magnetism and Device Development*, ACS Nano **18**, 8600 (2024).

[3] A. V. Kimel, A. Kirilyuk, and T. Rasing, *Femtosecond Opto-Magnetism: Ultrafast Laser Manipulation of Magnetic Materials*, Laser Photonics Rev. **1**, 3 (2007).

[4] S. Yang, T. Zhang, and C. Jiang, *Van Der Waals Magnets: Material Family, Detection and Modulation of Magnetism, and Perspective in Spintronics*, Adv. Sci. **8**, 2002488 (2021).

[5] A. Hirohata, K. Yamada, Y. Nakatani, I.-L. Prejbeanu, B. Diény, P. Pirro, and B. Hillebrands, *Review on Spintronics: Principles and Device Applications*, J. Magn. Magn. Mater. **509**, 166711 (2020).

[6] Q. H. Wang et al., *The Magnetic Genome of Two-Dimensional van Der Waals Materials*, ACS Nano **16**, 6960 (2022).

[7] V. P. Ningrum et al., *Recent Advances in Two-Dimensional Magnets: Physics and Devices towards Spintronic Applications*, Research **2020**, (2020).

[8] P. Liu, Y. Zhang, K. Li, Y. Li, and Y. Pu, *Recent Advances in 2D van Der Waals Magnets: Detection, Modulation, and Applications*, iScience **26**, 107584 (2023).

[9] H. Yan et al., *A Piezoelectric, Strain-Controlled Antiferromagnetic Memory Insensitive to Magnetic Fields*, Nat. Nanotechnol. **14**, 131 (2019).

[10] C. A. F. Vaz, J. A. C. Bland, and G. Lauhoff, *Magnetism in Ultrathin Film Structures*, Rep. Prog. Phys. **71**, 056501 (2008).

[11] K. S. Novoselov, A. K. Geim, S. V. Morozov, D. Jiang, Y. Zhang, S. V. Dubonos, I. V. Grigorieva, and A. A. Firsov, *Electric Field Effect in Atomically Thin Carbon Films*, Science **306**, 5696 (2004).

[12] H.-L. Liu, C.-C. Shen, S.-H. Su, C.-L. Hsu, M.-Y. Li, and L.-J. Li, *Optical Properties of Monolayer Transition Metal Dichalcogenides Probed by Spectroscopic Ellipsometry*, Appl. Phys. Lett. **105**, 201905 (2014).

[13] K. I. Bolotin, K. J. Sikes, Z. Jiang, M. Klima, G. Fudenberg, J. Hone, P. Kim, and H. L. Stormer, *Ultrahigh Electron Mobility in Suspended Graphene*, Solid State Commun. **146**, 351 (2008).

[14] S. Ahmed et al., *Inducing High Coercivity in MoS2 Nanosheets by Transition Element Doping*, Chem. Mater. **29**, 21 (2017).

[15] M. Habib, Z. Muhammad, R. Khan, C. Wu, Z. ur Rehman, Y. Zhou, H. Liu, and L. Song, *Ferromagnetism in CVT Grown Tungsten Diselenide Single Crystals with Nickel Doping*, Nanotechnology **29**, 11 (2018).

[16] B. Huang et al., *Layer-Dependent Ferromagnetism in a van Der Waals Crystal down to the Monolayer Limit*, Nature **546**, 270 (2017).

[17] C. Gong et al., *Discovery of Intrinsic Ferromagnetism in Two-Dimensional van Der Waals Crystals*, Nature **546**, 7657 (2017).

[18] C. Xu, J. Feng, H. Xiang, and L. Bellaiche, *Interplay between Kitaev Interaction and Single Ion Anisotropy in Ferromagnetic CrI3 and CrGeTe3 Monolayers*, Npj Comput. Mater. **4**, 1 (2018).

[19] L. Webster, L. Liang, and J.-A. Yan, *Distinct Spin–Lattice and Spin–Phonon Interactions in Monolayer Magnetic CrI 3*, Phys. Chem. Chem. Phys. **20**, 36 (2018).
[20] A. Milosavljević, A. Šolajić, J. Pešić, Y. Liu, C. Petrovic, N. Lazarević, and Z. V. Popović, *Evidence of Spin-Phonon Coupling in ${\mathrm{CrSiTe}}_{3}$*, Phys. Rev. B **98**, 10 (2018).
[21] Y. Liu and C. Petrovic, *Critical Behavior and Magnetocaloric Effect in ${\mathrm{Mn}}_{3}{\mathrm{Si}}_{2}{\mathrm{Te}}_{6}$*, Phys. Rev. B **98**, 6 (2018).
[22] Z. Fei et al., *Two-Dimensional Itinerant Ferromagnetism in Atomically Thin Fe 3 GeTe 2*, Nat. Mater. **17**, 9 (2018).
[23] K. S. Burch, D. Mandrus, and J.-G. Park, *Magnetism in Two-Dimensional van Der Waals Materials*, Nature **563**, 7729 (2018).
[24] Z. Wang et al., *Electric-Field Control of Magnetism in a Few-Layered van Der Waals Ferromagnetic Semiconductor*, Nat. Nanotechnol. **13**, 7 (2018).
[25] Y. Sun, R. C. Xiao, G. T. Lin, R. R. Zhang, L. S. Ling, Z. W. Ma, X. Luo, W. J. Lu, Y. P. Sun, and Z. G. Sheng, *Effects of Hydrostatic Pressure on Spin-Lattice Coupling in Two-Dimensional Ferromagnetic Cr2Ge2Te6*, Appl. Phys. Lett. **112**, 7 (2018).
[26] S. Jiang, L. Li, Z. Wang, K. F. Mak, and J. Shan, *Controlling Magnetism in 2D CrI 3 by Electrostatic Doping*, Nat. Nanotechnol. **13**, 549 (2018).
[27] Y. Deng et al., *Gate-Tunable Room-Temperature Ferromagnetism in Two-Dimensional Fe 3 GeTe 2*, Nature **563**, 7729 (2018).
[28] C. Wang, X. Zhou, Y. Pan, J. Qiao, X. Kong, C.-C. Kaun, and W. Ji, *Layer and Doping Tunable Ferromagnetic Order in Two-Dimensional $\mathrm{Cr}{\mathrm{S}}_{2}$ Layers*, Phys. Rev. B **97**, 24 (2018).
[29] S. Mondal, M. Kannan, M. Das, L. Govindaraj, R. Singha, B. Satpati, S. Arumugam, and P. Mandal, *Effect of Hydrostatic Pressure on Ferromagnetism in Two-Dimensional ${\mathrm{CrI}}_{3}$*, Phys. Rev. B **99**, 180407 (2019).
[30] T. A. Tartaglia et al., *Accessing New Magnetic Regimes by Tuning the Ligand Spin-Orbit Coupling in van Der Waals Magnets*, Sci. Adv. **6**, eabb9379 (2020).
[31] K. L. Seyler et al., *Ligand-Field Helical Luminescence in a 2D Ferromagnetic Insulator*, Nat. Phys. **14**, 3 (2018).
[32] J. F. Dillon and C. E. Olson, *Magnetization, Resonance, and Optical Properties of the Ferromagnet CrI3*, J. Appl. Phys. **36**, 3 (1965).
[33] J. F. Dillon, H. Kamimura, and J. P. Remeika, *Magneto-Optical Properties of Ferromagnetic Chromium Trihalides*, J. Phys. Chem. Solids **27**, 9 (1966).
[34] B. Wang, S. Yang, J. Chen, C. Mann, A. Bushmaker, and S. B. Cronin, *Radiation-Induced Direct Bandgap Transition in Few-Layer MoS2*, Appl. Phys. Lett. **111**, 13 (2017).
[35] A. K. Geremew et al., *Proton-Irradiation-Immune Electronics Implemented with Two-Dimensional Charge-Density-Wave Devices*, Nanoscale **11**, 17 (2019).
[36] R. C. Walker, T. Shi, B. Jariwala, I. Jovanovic, and J. A. Robinson, *Stability of the Tungsten Diselenide and Silicon Carbide Heterostructure against High Energy Proton Exposure*, Appl. Phys. Lett. **111**, 14 (2017).
[37] P. Esquinazi, D. Spemann, R. Höhne, A. Setzer, K.-H. Han, and T. Butz, *Induced Magnetic Ordering by Proton Irradiation in Graphite*, Phys. Rev. Lett. **91**, 22 (2003).
[38] P. Esquinazi, R. Höhne, K.-H. Han, A. Setzer, D. Spemann, and T. Butz, *Magnetic Carbon: Explicit Evidence of Ferromagnetism Induced by Proton Irradiation*, Carbon **42**, 7 (2004).

[39] S. Mathew et al., *Magnetism in MoS2 Induced by Proton Irradiation*, Appl. Phys. Lett. **101**, 10 (2012).
[40] E. M. Mozur and R. Seshadri, *Methods and Protocols: Practical Magnetic Measurement*, Chem. Mater. **35**, 3450 (2023).
[41] S. Mugiraneza and A. M. Hallas, *Tutorial: A Beginner's Guide to Interpreting Magnetic Susceptibility Data with the Curie-Weiss Law*, Commun. Phys. **5**, 1 (2022).
[42] Quantum Design, *Fiber Optic Sample Holder (VSM)*, (n.d.).
[43] Quantum Design, *TLS120Xe and MLS Xenon Light Source*, (2021).
[44] M. M. Roessler and E. Salvadori, *Principles and Applications of EPR Spectroscopy in the Chemical Sciences*, Chem. Soc. Rev. **47**, 2534 (2018).
[45] J. A. Weil and J. R. Bolton, *Electron Paramagnetic Resonance: Elementary Theory and Practical Applications* (John Wiley & Sons, 2007).
[46] A. S. Disa et al., *Photo-Induced High-Temperature Ferromagnetism in YTiO3*, Nature **617**, 7959 (2023).
[47] M. Fiebig, K. Miyano, Y. Tomioka, and Y. Tokura, *Visualization of the Local Insulator-Metal Transition in Pr0.7Ca0.3MnO3*, Science **280**, 1925 (1998).
[48] B. Koopmans, G. Malinowski, F. Dalla Longa, D. Steiauf, M. Fähnle, T. Roth, M. Cinchetti, and M. Aeschlimann, *Explaining the Paradoxical Diversity of Ultrafast Laser-Induced Demagnetization*, Nat. Mater. **9**, 259 (2010).
[49] M. Pankratova, I. P. Miranda, D. Thonig, M. Pereiro, E. Sjöqvist, A. Delin, O. Eriksson, and A. Bergman, *Heat-Conserving Three-Temperature Model for Ultrafast Demagnetization in Nickel*, Phys. Rev. B **106**, 174407 (2022).
[50] T. Lichtenberg, C. F. Schippers, S. C. P. van Kooten, S. G. F. Evers, B. Barcones, M. H. D. Guimarães, and B. Koopmans, *Anisotropic Laser-Pulse-Induced Magnetization Dynamics in van Der Waals Magnet Fe3GeTe2*, 2D Mater. **10**, 015008 (2022).
[51] T. Sun et al., *Ultra-Long Spin Relaxation in Two-Dimensional Ferromagnet Cr$\less$sub$\greater$2$\less$/sub$\greater$Ge$\less$sub$\greater$2$\less$/sub$\greater$Te$\less$sub$\greater$6$\less$/Sub$\greater$ Flake*, 2D Mater. **8**, 045040 (2021).
[52] R. P. P. Taylor Antoinette J., editor , *Optical Techniques for Solid-State Materials Characterization* (CRC Press, Boca Raton, 2012).
[53] R. Trebino, P. Bowlan, P. Gabolde, X. Gu, S. Akturk, and M. Kimmel, *Simple Devices for Measuring Complex Ultrashort Pulses*, Laser Photonics Rev. **3**, 314 (2009).
[54] D. W. Snoke, *Solid State Physics: Essential Concepts* (Addison Wesley, 2008).
[55] G. R. Fowles, *Introduction to Modern Optics* (Courier Corporation, 1989).
[56] X.-X. Zhang, L. Li, D. Weber, J. Goldberger, K. F. Mak, and J. Shan, *Gate-Tunable Spin Waves in Antiferromagnetic Atomic Bilayers*, Nat. Mater. **19**, 8 (2020).
[57] S. Jiang, L. Li, Z. Wang, K. F. Mak, and J. Shan, *Controlling Magnetism in 2D CrI 3 by Electrostatic Doping*, Nat. Nanotechnol. **13**, 7 (2018).
[58] M. Abramchuk, S. Jaszewski, K. R. Metz, G. B. Osterhoudt, Y. Wang, K. S. Burch, and F. Tafti, *Controlling Magnetic and Optical Properties of the van Der Waals Crystal CrCl3−xBrx via Mixed Halide Chemistry*, Adv. Mater. **30**, 25 (2018).
[59] T. A. Tartaglia et al., *Accessing New Magnetic Regimes by Tuning the Ligand Spin-Orbit Coupling in van Der Waals Magnets*, Sci. Adv. **6**, 30 (2020).
[60] W. Lems, P. J. Rijnierse, P. F. Bongers, and U. Enz, *Photomagnetic Effect in a Chalcogenide Spinel*, Phys. Rev. Lett. **21**, 1643 (1968).

[61] E. Beaurepaire, J.-C. Merle, A. Daunois, and J.-Y. Bigot, *Ultrafast Spin Dynamics in Ferromagnetic Nickel*, Phys. Rev. Lett. **76**, 4250 (1996).
[62] R. V. Mikhaylovskiy et al., *Ultrafast Optical Modification of Exchange Interactions in Iron Oxides*, Nat. Commun. **6**, 8190 (2015).
[63] C. Banerjee, N. Teichert, K. E. Siewierska, Z. Gercsi, G. Y. P. Atcheson, P. Stamenov, K. Rode, J. M. D. Coey, and J. Besbas, *Single Pulse All-Optical Toggle Switching of Magnetization without Gadolinium in the Ferrimagnet Mn2RuxGa*, Nat. Commun. **11**, 4444 (2020).
[64] J.-Y. Shan, M. Ye, H. Chu, S. Lee, J.-G. Park, L. Balents, and D. Hsieh, *Giant Modulation of Optical Nonlinearity by Floquet Engineering*, Nature **600**, 7888 (2021).
[65] B. Liu et al., *Light-Tunable Ferromagnetism in Atomically Thin ${\mathrm{Fe}}_{3}{\mathrm{GeTe}}_{2}$ Driven by Femtosecond Laser Pulse*, Phys. Rev. Lett. **125**, 267205 (2020).
[66] T. Amano et al., *Light-Induced Magnetization Driven by Interorbital Charge Motion in the Spin-Orbit Assisted Mott Insulator $\ensuremath{\alpha}\text{\ensuremath{-}}{\mathrm{RuCl}}_{3}$*, Phys. Rev. Res. **4**, L032032 (2022).
[67] A. Ron, S. Chaudhary, G. Zhang, H. Ning, E. Zoghlin, S. D. Wilson, R. D. Averitt, G. Refael, and D. Hsieh, *Ultrafast Enhancement of Ferromagnetic Spin Exchange Induced by Ligand-to-Metal Charge Transfer*, Phys. Rev. Lett. **125**, 197203 (2020).
[68] D. Afanasiev et al., *Controlling the Anisotropy of a van Der Waals Antiferromagnet with Light*, Sci. Adv. **7**, eabf3096 (2021).
[69] S. R. Singamaneni, L. M. Martinez, J. Niklas, O. G. Poluektov, R. Yadav, M. Pizzochero, O. V. Yazyev, and M. A. McGuire, *Light Induced Electron Spin Resonance Properties of van Der Waals CrX3 (X = Cl, I) Crystals*, Appl. Phys. Lett. **117**, 8 (2020).
[70] J. F. Dillon, H. Kamimura, and J. P. Remeika, *Magneto-Optical Properties of Ferromagnetic Chromium Trihalides*, J. Phys. Chem. Solids **27**, 1531 (1966).
[71] K. L. Seyler et al., *Ligand-Field Helical Luminescence in a 2D Ferromagnetic Insulator*, Nat. Phys. **14**, 277 (2018).
[72] M. Wu, Z. Li, T. Cao, and S. G. Louie, *Physical Origin of Giant Excitonic and Magneto-Optical Responses in Two-Dimensional Ferromagnetic Insulators*, Nat. Commun. **10**, 1 (2019).
[73] A. Arora et al., *Interlayer Excitons in a Bulk van Der Waals Semiconductor*, Nat. Commun. **8**, 1 (2017).
[74] M.-W. Lin et al., *Ultrathin Nanosheets of CrSiTe3: A Semiconducting Two-Dimensional Ferromagnetic Material*, J. Mater. Chem. C **4**, 2 (2015).
[75] P. Zhang, T.-F. Chung, Q. Li, S. Wang, Q. Wang, W. L. B. Huey, S. Yang, J. E. Goldberger, J. Yao, and X. Zhang, *All-Optical Switching of Magnetization in Atomically Thin CrI3*, Nat. Mater. **21**, 12 (2022).
[76] K. Shinagawa, H. Sato, H. J. Ross, L. F. McAven, and P. H. Butler, *Charge-Transfer Transitions in Chromium Trihalides*, J. Phys. Condens. Matter **8**, 8457 (1996).
[77] J. F. Dillon and C. E. Olson, *Magnetization, Resonance, and Optical Properties of the Ferromagnet CrI3*, J. Appl. Phys. **36**, 1259 (1965).
[78] V. K. Gudelli and G.-Y. Guo, *Magnetism and Magneto-Optical Effects in Bulk and Few-Layer CrI3: A Theoretical GGA $\mathplus$Ustudy*, New J. Phys. **21**, 053012 (2019).

[79] F. Juliá, *Ligand-to-Metal Charge Transfer (LMCT) Photochemistry at 3d-Metal Complexes: An Emerging Tool for Sustainable Organic Synthesis*, ChemCatChem **14**, e202200916 (2022).
[80] O. Laporte and W. F. Meggers, *Some Rules of Spectral Structure**, JOSA **11**, 459 (1925).
[81] D. C. Harris and M. D. Bertolucci, *Symmetry and Spectroscopy: An Introduction to Vibrational and Electronic Spectroscopy* (Courier Corporation, 1989).
[82] P. Padmanabhan et al., *Coherent Helicity-Dependent Spin-Phonon Oscillations in the Ferromagnetic van Der Waals Crystal CrI3*, Nat. Commun. **13**, 1 (2022).
[83] M. A. McGuire, H. Dixit, V. R. Cooper, and B. C. Sales, *Coupling of Crystal Structure and Magnetism in the Layered, Ferromagnetic Insulator CrI3*, Chem. Mater. **27**, 612 (2015).
[84] C. Xu, J. Feng, H. Xiang, and L. Bellaiche, *Interplay between Kitaev Interaction and Single Ion Anisotropy in Ferromagnetic CrI3 and CrGeTe3 Monolayers*, Npj Comput. Mater. **4**, 1 (2018).
[85] E. Mosiniewicz-Szablewska and H. Szymczak, *Photoinduced Changes in the Ferromagnetic Resonance of CdCr2Se4 Single Crystals*, J. Magn. Magn. Mater. **104–107**, 986 (1992).
[86] K. Yoshizawa, F. Mohri, G. Nuspl, and T. Yamabe, *Analysis of Photoinduced Magnetization in a (Co, Fe) Prussian Blue Model*, J. Phys. Chem. B **102**, 5432 (1998).
[87] J. Wang, I. Cotoros, K. M. Dani, X. Liu, J. K. Furdyna, and D. S. Chemla, *Ultrafast Enhancement of Ferromagnetism via Photoexcited Holes in GaMnAs*, Phys. Rev. Lett. **98**, 217401 (2007).
[88] J. Kim, K.-W. Kim, B. Kim, C.-J. Kang, D. Shin, S.-H. Lee, B.-C. Min, and N. Park, *Exploitable Magnetic Anisotropy of the Two-Dimensional Magnet CrI3*, Nano Lett. **20**, 929 (2020).
[89] I. V. Kashin, V. V. Mazurenko, M. I. Katsnelson, and A. N. Rudenko, *Orbitally-Resolved Ferromagnetism of Monolayer CrI3*, 2D Mater. **7**, 025036 (2020).
[90] R. V. Mikhaylovskiy, T. J. Huisman, V. A. Gavrichkov, S. I. Polukeev, S. G. Ovchinnikov, D. Afanasiev, R. V. Pisarev, Th. Rasing, and A. V. Kimel, *Resonant Pumping of $d\mathrm{\ensuremath{-}}d$ Crystal Field Electronic Transitions as a Mechanism of Ultrafast Optical Control of the Exchange Interactions in Iron Oxides*, Phys. Rev. Lett. **125**, 157201 (2020).
[91] L. Chen, J.-H. Chung, B. Gao, T. Chen, M. B. Stone, A. I. Kolesnikov, Q. Huang, and P. Dai, *Topological Spin Excitations in Honeycomb Ferromagnet ${\mathrm{CrI}}_{3}$*, Phys. Rev. X **8**, 041028 (2018).
[92] R. V. Mikhaylovskiy et al., *Ultrafast Optical Modification of Exchange Interactions in Iron Oxides*, Nat. Commun. **6**, 8190 (2015).
[93] S. R. Singamaneni, L. M. Martinez, J. Niklas, O. G. Poluektov, R. Yadav, M. Pizzochero, O. V. Yazyev, and M. A. McGuire, *Light Induced Electron Spin Resonance Properties of van Der Waals CrX3 (X = Cl, I) Crystals*, Appl. Phys. Lett. **117**, 082406 (2020).
[94] J. Cenker et al., *Direct Observation of Two-Dimensional Magnons in Atomically Thin CrI 3*, Nat. Phys. **17**, 1 (2021).
[95] L. Chen et al., *Magnetic Anisotropy in Ferromagnetic ${\mathrm{CrI}}_{3}$*, Phys. Rev. B **101**, 134418 (2020).

[96] J. Kim, K.-W. Kim, B. Kim, C.-J. Kang, D. Shin, S.-H. Lee, B.-C. Min, and N. Park, *Exploitable Magnetic Anisotropy of the Two-Dimensional Magnet CrI3*, Nano Lett. **20**, 929 (2020).
[97] M. A. McGuire, G. Clark, S. KC, W. M. Chance, G. E. Jellison, V. R. Cooper, X. Xu, and B. C. Sales, *Magnetic Behavior and Spin-Lattice Coupling in Cleavable van Der Waals Layered ${\mathrm{CrCl}}_{3}$ Crystals*, Phys. Rev. Mater. **1**, 014001 (2017).
[98] D. R. Klein et al., *Enhancement of Interlayer Exchange in an Ultrathin Two-Dimensional Magnet*, Nat. Phys. **15**, 1255 (2019).
[99] F. Yao, V. Multian, Z. Wang, N. Ubrig, J. Teyssier, F. Wu, E. Giannini, M. Gibertini, I. Gutiérrez-Lezama, and A. F. Morpurgo, *Multiple Antiferromagnetic Phases and Magnetic Anisotropy in Exfoliated CrBr3 Multilayers*, Nat. Commun. **14**, 4969 (2023).
[100] B. Niu et al., *Coexistence of Magnetic Orders in Two-Dimensional Magnet CrI3*, Nano Lett. **20**, 553 (2020).
[101] A. McCreary et al., *Distinct Magneto-Raman Signatures of Spin-Flip Phase Transitions in CrI3*, Nat. Commun. **11**, 3879 (2020).
[102] X. Cai et al., *Atomically Thin CrCl3: An in-Plane Layered Antiferromagnetic Insulator*, ArXiv190400261 Cond-Mat (2019).
[103] Z. Wang, M. Gibertini, D. Dumcenco, T. Taniguchi, K. Watanabe, E. Giannini, and A. F. Morpurgo, *Determining the Phase Diagram of Atomically Thin Layered Antiferromagnet CrCl3*, Nat. Nanotechnol. **14**, 1116 (2019).
[104] X. Cai et al., *Atomically Thin CrCl3: An In-Plane Layered Antiferromagnetic Insulator*, Nano Lett. **19**, 3993 (2019).
[105] V. Singh, G. Sivaramaiah, J. L. Rao, and S. H. Kim, *EPR and Optical Investigations of LaMgAl11O19:Cr3+ Phosphor*, Mater. Res. Bull. **60**, 397 (2014).
[106] J. P. Joshi and S. V. Bhat, *On the Analysis of Broad Dysonian Electron Paramagnetic Resonance Spectra*, J. Magn. Reson. **168**, 284 (2004).
[107] C. P. J. Poole and H. A. Farach, *Handbook of Electron Spin Resonance* (Springer Science & Business Media, 1999).
[108] S. Chehab, J. Amiell, P. Biensan, and S. Flandrois, *Two-Dimensional ESR Behaviour of CrCl3*, Phys. B Condens. Matter **173**, 211 (1991).
[109] E. Mosiniewicz-Szablewska and H. Szymczak, *Photomagnetic Effect in the ${\mathrm{CdCr}}_{2}${\mathrm{Se}}_{4}$ Ferromagnetic Semiconductor*, Phys. Rev. B **47**, 8700 (1993).
[110] Yu. M. Fedorov, A. A. Leksikov, and A. E. Aksenov, *Light-Induced Dynamic Instability of the Domain Structure in FeBo3:Ni*, ZhETF Pisma Redaktsiiu **37**, 134 (1983).
[111] F. Varsanyi, D. L. Wood, and A. L. Schawlow, *Self-Absorption and Trapping of Sharp-Line Resonance Radiation in Ruby*, Phys. Rev. Lett. **3**, 544 (1959).
[112] J. Liu, Q. Sun, Y. Kawazoe, and P. Jena, *Exfoliating Biocompatible Ferromagnetic Cr-Trihalide Monolayers*, Phys. Chem. Chem. Phys. **18**, 8777 (2016).
[113] J. T. Vallin and G. D. Watkins, *EPR of ${\mathrm{Cr}}^{2+}$ in II-VI Lattices*, Phys. Rev. B **9**, 2051 (1974).
[114] T. Helgaker, P. Jorgensen, and J. Olsen, *Molecular Electronic-Structure Theory* (John Wiley & Sons, 2014).
[115] L. F. Chibotaru and L. Ungur, *Ab Initio Calculation of Anisotropic Magnetic Properties of Complexes. I. Unique Definition of Pseudospin Hamiltonians and Their Derivation*, J. Chem. Phys. **137**, 064112 (2012).

[116] D.-H. Kim, K. Kim, K.-T. Ko, J. Seo, J. S. Kim, T.-H. Jang, Y. Kim, J.-Y. Kim, S.-W. Cheong, and J.-H. Park, *Giant Magnetic Anisotropy Induced by Ligand LS Coupling in Layered Cr Compounds*, Phys. Rev. Lett. **122**, 207201 (2019).
[117] L. M. Martinez et al., *Coherent Spin-Phonon Coupling in the Layered Ferrimagnet Mn3Si2Te6*, arXiv:2308.14931.
[118] E. Beaurepaire, J.-C. Merle, A. Daunois, and J.-Y. Bigot, *Ultrafast Spin Dynamics in Ferromagnetic Nickel*, Phys. Rev. Lett. **76**, 22 (1996).
[119] F. Hansteen, A. Kimel, A. Kirilyuk, and T. Rasing, *Nonthermal Ultrafast Optical Control of the Magnetization in Garnet Films*, Phys. Rev. B **73**, 014421 (2006).
[120] G. Wu, S. Chen, Y. Ren, Q. Y. Jin, and Z. Zhang, *Laser-Induced Magnetization Dynamics in Interlayer-Coupled [Ni/Co]4/Ru/[Co/Ni]3 Perpendicular Magnetic Films for Information Storage*, ACS Appl. Nano Mater. **2**, 8 (2019).
[121] D. Afanasiev, J. R. Hortensius, B. A. Ivanov, A. Sasani, E. Bousquet, Y. M. Blanter, R. V. Mikhaylovskiy, A. V. Kimel, and A. D. Caviglia, *Ultrafast Control of Magnetic Interactions via Light-Driven Phonons*, Nat. Mater. **20**, 5 (2021).
[122] M. Först, C. Manzoni, S. Kaiser, Y. Tomioka, Y. Tokura, R. Merlin, and A. Cavalleri, *Nonlinear Phononics as an Ultrafast Route to Lattice Control*, Nat. Phys. **7**, 11 (2011).
[123] M.-C. Lee et al., *Strong Spin-Phonon Coupling Unveiled by Coherent Phonon Oscillations in ${\mathrm{Ca}}_{2}{\mathrm{RuO}}_{4}$*, Phys. Rev. B **99**, 14 (2019).
[124] A. S. Disa et al., *Photo-Induced High-Temperature Ferromagnetism in YTiO3*, Nature **617**, 7959 (2023).
[125] M. Matsubara, Y. Okimoto, T. Ogasawara, Y. Tomioka, H. Okamoto, and Y. Tokura, *Ultrafast Photoinduced Insulator-Ferromagnet Transition in the Perovskite Manganite ${\mathrm{Gd}}_{0.55}{\mathrm{Sr}}_{0.45}{\mathrm{MnO}}_{3}$*, Phys. Rev. Lett. **99**, 20 (2007).
[126] M. Fiebig, K. Miyano, Y. Tomioka, and Y. Tokura, *Visualization of the Local Insulator-Metal Transition in Pr0.7Ca0.3MnO3*, Science **280**, 5371 (1998).
[127] Y. Liu and C. Petrovic, *Critical Behavior and Magnetocaloric Effect in ${\mathrm{Mn}}_{3}{\mathrm{Si}}_{2}{\mathrm{Te}}_{6}$*, Phys. Rev. B **98**, 6 (2018).
[128] A. F. May, Y. Liu, S. Calder, D. S. Parker, T. Pandey, E. Cakmak, H. Cao, J. Yan, and M. A. McGuire, *Magnetic Order and Interactions in Ferrimagnetic ${\mathrm{Mn}}_{3}{\mathrm{Si}}_{2}{\mathrm{Te}}_{6}$*, Phys. Rev. B **95**, 174440 (2017).
[129] Y. Zhang, L.-F. Lin, A. Moreo, and E. Dagotto, *Electronic Structure, Magnetic Properties, Spin Orientation, and Doping Effect in Mn$_3$Si$_2$Te$_6$*, arXiv:2211.13321.
[130] F. Ye, M. Matsuda, Z. Morgan, T. Sherline, Y. Ni, H. Zhao, and G. Cao, *Magnetic Structure and Spin Fluctuations in the Colossal Magnetoresistance Ferrimagnet ${\mathrm{Mn}}_{3}{\mathrm{Si}}_{2}{\mathrm{Te}}_{6}$*, Phys. Rev. B **106**, L180402 (2022).
[131] Y. Ni, H. Zhao, Y. Zhang, B. Hu, I. Kimchi, and G. Cao, *Colossal Magnetoresistance via Avoiding Fully Polarized Magnetization in the Ferrimagnetic Insulator ${\mathrm{Mn}}_{3}{\mathrm{Si}}_{2}{\mathrm{Te}}_{6}$*, Phys. Rev. B **103**, 16 (2021).
[132] J. Seo et al., *Colossal Angular Magnetoresistance in Ferrimagnetic Nodal-Line Semiconductors*, Nature **599**, 7886 (2021).

[133] Y. Zhang, Y. Ni, H. Zhao, S. Hakani, F. Ye, L. DeLong, I. Kimchi, and G. Cao, *Control of Chiral Orbital Currents in a Colossal Magnetoresistance Material*, Nature **611**, 7936 (2022).
[134] S. Djurdjić Mijin, A. Šolajić, J. Pešić, Y. Liu, C. Petrovic, M. Bockstedte, A. Bonanni, Z. V. Popović, and N. Lazarević, *Spin-Phonon Interaction and Short-Range Order in ${\mathrm{Mn}}_{3}{\mathrm{Si}}_{2}{\mathrm{Te}}_{6}$*, Phys. Rev. B **107**, 054309 (2023).
[135] J. Guo, W. Liang, and S.-N. Luo, *Anomalous Hot Carrier Decay in Ferromagnetic Cr2Ge2Te6 via Spin–Phonon Coupling*, J. Phys. Chem. Lett. **11**, 9351 (2020).
[136] D. J. Lovinger et al., *Magnetoelastic Coupling to Coherent Acoustic Phonon Modes in the Ferrimagnetic Insulator $\mathrm{Gd}\mathrm{Ti}{\mathrm{O}}_{3}$*, Phys. Rev. B **102**, 085138 (2020).
[137] A. Q. Wu, X. Xu, and R. Venkatasubramanian, *Ultrafast Dynamics of Photoexcited Coherent Phonon in Bi2Te3 Thin Films*, Appl. Phys. Lett. **92**, 011108 (2008).
[138] E. Sutcliffe, X. Sun, I. Verzhbitskiy, T. Griepe, U. Atxitia, G. Eda, E. J. G. Santos, and J. O. Johansson, *Transient Magneto-Optical Spectrum of Photoexcited Electrons in the van Der Waals Ferromagnet ${\mathrm{Cr}}_{2}{\mathrm{Ge}}_{2}{\mathrm{Te}}_{6}$*, Phys. Rev. B **107**, 174432 (2023).
[139] K. Carva, M. Battiato, and P. M. Oppeneer, *Ab Initio Investigation of the Elliott-Yafet Electron-Phonon Mechanism in Laser-Induced Ultrafast Demagnetization*, Phys. Rev. Lett. **107**, 207201 (2011).
[140] D. Bossini, S. Dal Conte, M. Terschanski, G. Springholz, A. Bonanni, K. Deltenre, F. Anders, G. S. Uhrig, G. Cerullo, and M. Cinchetti, *Femtosecond Phononic Coupling to Both Spins and Charges in a Room-Temperature Antiferromagnetic Semiconductor*, Phys. Rev. B **104**, 224424 (2021).
[141] K. Ishioka and O. V. Misochko, *Coherent Lattice Oscillations in Solids and Their Optical Control*, in *Progress in Ultrafast Intense Laser Science: Volume V*, edited by K. Yamanouchi, A. Giulietti, and K. Ledingham (Springer, Berlin, Heidelberg, 2010), pp. 23–46.
[142] T. Dekorsy, G. C. Cho, and H. Kurz, *Coherent Phonons in Condensed Media*, in *Light Scattering in Solids VIII: Fullerenes, Semiconductor Surfaces, Coherent Phonons*, edited by M. Cardona and G. Güntherodt (Springer, Berlin, Heidelberg, 2000), pp. 169–209.
[143] S. Hunsche, K. Wienecke, T. Dekorsy, and H. Kurz, *Impulsive Softening of Coherent Phonons in Tellurium*, Phys. Rev. Lett. **75**, 1815 (1995).
[144] K. Ishioka and O. V. Misochko, *Coherent Lattice Oscillations in Solids and Their Optical Control*, in *Progress in Ultrafast Intense Laser Science: Volume V*, edited by K. Yamanouchi, A. Giulietti, and K. Ledingham (Springer, Berlin, Heidelberg, 2010), pp. 23–46.
[145] R. Merlin, *Generating Coherent THz Phonons with Light Pulses*, Solid State Commun. **102**, 207 (1997).
[146] A. Baum et al., *Phonon Anomalies in FeS*, Phys. Rev. B **97**, 054306 (2018).
[147] S. Jiang, H. Xie, J. Shan, and K. F. Mak, *Exchange Magnetostriction in Two-Dimensional Antiferromagnets*, Nat. Mater. **19**, 12 (2020).
[148] Y. Tian, M. J. Gray, H. Ji, R. J. Cava, and K. S. Burch, *Magneto-Elastic Coupling in a Potential Ferromagnetic 2D Atomic Crystal*, 2D Mater. **3**, 025035 (2016).

[149] K. Kim, S. Y. Lim, J.-U. Lee, S. Lee, T. Y. Kim, K. Park, G. S. Jeon, C.-H. Park, J.-G. Park, and H. Cheong, *Suppression of Magnetic Ordering in XXZ-Type Antiferromagnetic Monolayer NiPS3*, Nat. Commun. **10**, 1 (2019).
[150] T. Yin et al., *Chiral Phonons and Giant Magneto-Optical Effect in CrBr3 2D Magnet*, Adv. Mater. **33**, 2101618 (2021).
[151] D. Czernia, P. Konieczny, E. Juszyńska-Gałązka, M. Perzanowski, J. Lekki, A. B. G. Guillén, and W. Łasocha, *Influence of Proton Irradiation on the Magnetic Properties of Two-Dimensional Ni(II) Molecular Magnet*, Sci. Rep. **13**, 14032 (2023).
[152] S. Mathew et al., *Magnetism in MoS2 Induced by Proton Irradiation*, Appl. Phys. Lett. **101**, 102103 (2012).
[153] P. Esquinazi, D. Spemann, R. Höhne, A. Setzer, K.-H. Han, and T. Butz, *Induced Magnetic Ordering by Proton Irradiation in Graphite*, Phys. Rev. Lett. **91**, 227201 (2003).
[154] S. Mathew, B. Satpati, B. Joseph, B. N. Dev, R. Nirmala, S. K. Malik, and R. Kesavamoorthy, *Magnetism in ${\mathrm{C}}_{60}$ Films Induced by Proton Irradiation*, Phys. Rev. B **75**, 075426 (2007).
[155] S. W. Han et al., *Controlling Ferromagnetic Easy Axis in a Layered ${\mathrm{MoS}}_{2}$ Single Crystal*, Phys. Rev. Lett. **110**, 247201 (2013).
[156] T. L. Makarova, A. L. Shelankov, I. T. Serenkov, V. I. Sakharov, and D. W. Boukhvalov, *Anisotropic Magnetism of Graphite Irradiated with Medium-Energy Hydrogen and Helium Ions*, Phys. Rev. B **83**, 085417 (2011).
[157] U. Abdurakhmanov, A. B. Granovskii, A. A. Radkovskaya, M. Kh. Usmanov, Sh. M. Sharipov, and V. P. Yugai, *The Influence of Neutron and Proton Irradiation on the Magnetization of Biotite*, Phys. Solid State **44**, 312 (2002).
[158] A. J. Samin, *A Review of Radiation-Induced Demagnetization of Permanent Magnets*, J. Nucl. Mater. **503**, 42 (2018).
[159] R. Olmos, A. Cosio, C. L. Saiz, L. M. Martinez, L. Shao, Q. Wang, and S. R. Singamaneni, *Magnetic Properties of Proton Irradiated Fe2.7GeTe2 Bulk Crystals*, MRS Adv. 1 (undefined/ed).
[160] H. Iturriaga, J. Chen, J. Yang, L. M. Martinez, L. Shao, Y. Liu, C. Petrovic, M. Kirk, and S. R. Singamaneni, *Proton-Fluence Dependent Magnetic Properties of Exfoliable Quasi-2D van Der Waals Cr2Si2Te6 Magnet*, J. Phys. Condens. Matter **36**, 22 (2024).
[161] Y. Liu and C. Petrovic, *Critical Behavior and Magnetocaloric Effect in ${\mathrm{Mn}}_{3}{\mathrm{Si}}_{2}{\mathrm{Te}}_{6}$*, Phys. Rev. B **98**, 064423 (2018).
[162] P. M. Richards and M. B. Salamon, *Exchange Narrowing of Electron Spin Resonance in a Two-Dimensional System*, Phys. Rev. B **9**, 32 (1974).
[163] N. S. Sangeetha, S. D. Cady, and D. C. Johnston, *EPR Measurements of Eu{+2} Spins in Metallic EuCo{2-y}As2 Single Crystals*, arXiv:1809.02653.
[164] K. W. Lee and C. E. Lee, *Electron Spin Resonance of Proton-Irradiated Graphite*, Phys. Rev. Lett. **97**, 137206 (2006).
[165] A. Milosavljević, A. Šolajić, J. Pešić, Y. Liu, C. Petrovic, N. Lazarević, and Z. V. Popović, *Evidence of Spin-Phonon Coupling in ${\mathrm{CrSiTe}}_{3}$*, Phys. Rev. B **98**, 104306 (2018).
[166] M.-W. Lin et al., *Ultrathin Nanosheets of CrSiTe3: A Semiconducting Two-Dimensional Ferromagnetic Material*, J. Mater. Chem. C **4**, 315 (2015).

[167] G. Sala, J. Y. Y. Lin, A. M. Samarakoon, D. S. Parker, A. F. May, and M. B. Stone, *Ferrimagnetic Spin Waves in Honeycomb and Triangular Layers of ${\mathrm{Mn}}_{3}{\mathrm{Si}}_{2}{\mathrm{Te}}_{6}$*, Phys. Rev. B **105**, 214405 (2022).
[168] A. Ron, S. Chaudhary, G. Zhang, H. Ning, E. Zoghlin, S. D. Wilson, R. D. Averitt, G. Refael, and D. Hsieh, *Ultrafast Enhancement of Ferromagnetic Spin Exchange Induced by Ligand-to-Metal Charge Transfer*, Phys. Rev. Lett. **125**, 19 (2020).
[169] R. Olmos, J. A. Delgado, H. Iturriaga, L. M. Martinez, C. L. Saiz, L. Shao, Y. Liu, C. Petrovic, and S. R. Singamaneni, *Critical Phenomena of the Layered Ferrimagnet Mn3Si2Te6 Following Proton Irradiation*, J. Appl. Phys. **130**, 013902 (2021).
[170] R. Olmos, P.-H. Chang, P. Mishra, R. R. Zope, T. Baruah, Y. Liu, C. Petrovic, and S. R. Singamaneni, *Pressure-Dependent Magnetic Properties of Quasi-2D Cr2Si2Te6 and Mn3Si2Te6*, J. Phys. Chem. C **127**, 21 (2023).
[171] R. Olmos, S. Alam, P.-H. Chang, K. Gandha, I. C. Nlebedim, A. Cole, F. Tafti, R. R. Zope, and S. R. Singamaneni, *Pressure Dependent Magnetic Properties on Bulk CrBr3 Single Crystals*, J. Alloys Compd. **911**, 165034 (2022).

Vita

My name is Luis Miguel Martinez Milian, and I come from a small island in the Caribbean called Puerto Rico. In my home, I completed an associate's degree in Technology for Electronics followed by a bachelor's degree in Physics Applied to Electronics. During my time as an undergraduate student, I was fortunate to participate in the Partnership for Research and Education (PREM) program allowing me to gain research experience early on with mentorship from Dr. Nicholas Pinto and Dr. Idalia Ramos. After completing my undergraduate degree, I traveled to El Paso, Texas to pursue a master's degree in Physics at the University of Texas at El Paso (UTEP). Once there, I began working under the tutelage of Dr. Singamaneni. Having gained enough confidence in my ability as a researcher, I decided to pursue a Ph.D. in Material Science and Engineering at UTEP while remaining in Dr. Srinivasa's lab with great support from the Bridge to the Doctorate Louise Stokes Alliance for Minority Participation (BD-LSAMP).

From the beginning of my undergraduate degree to where I stand now (Spring 2024), I have amassed 17 publications with 6 first authors publications (3 of which are directly tied to this dissertation). As a student in Dr. Singamaneni's lab, I became quite proficient in the Electron Paramagnetic Resonance spectroscopic technique along with magnetic materials characterization. My research experience grew when I was chosen as a Science Graduate Student Research (SCGSR) fellow, allowing me to conduct research in Los Alamos National Lab under the guiding hands of Dr. Prasankumar and Dr. Padmanabhan. During my time as an SCGSR fellow, I learned a new-to-me field in the form of Ultrafast Pump-Probe Spectroscopy gaining a strong grasp on nonlinear optical phenomena.